



CIMR DEVALGO



CIMR Level-2 Algorithm Development
(CIMR-DEVALGO)

Contract number:
4000137493/22/NL/AD

Algorithm Theoretical Basis Document v2 for the Sea Surface Salinity Level-2 product

ATBD SSS v2 D-5

Issue: 2.0

Date: 27/08/2024



Norwegian
Meteorological
Institute

The Norwegian Meteorological Institute
(MET Norway)
Henrik Mohns Plass 1
N-0313 Oslo
Norway
Phone: + 47 22 96 30 00
Fax: + 47 22 96 30 50

	E-Mail: thomas.lavergne@met.no http://met.no
--	---

Contract CIMR LEVEL-2 ALGORITHM DEVELOPMENT (CIMR DEVALGO)	Deliverable ATBD SSS v2, 2.0
CLIENT European Space Agency	CLIENT REFERENCE 4000137493/22/NL/AD
Revision date: 27/08/2024	Approval by ESA (date + signature)

Table of Contents

1.	Abstract	6
2.	Applicable and reference documents	6
3.	Acronyms	7
4.	Definitions used in this ATBD	9
5.	Introduction, purpose and scope	11
6.	Background and justification of selected algorithm	12
6.1	Introduction	12
6.2	Historical Heritage	14
6.3	Justification of selected algorithm	16
6.3.1	Model for the dielectric constant of the seawater at L-band.....	16
6.3.2	Model for correcting the sea surface roughness emission	19
6.3.3	Model for other geophysical contributions	20
7.	Level-2 product definition	22
8.	Baseline Algorithm Definition.....	23
8.1	Overview	23
8.2	Level-2 end to end algorithm functional flow diagram	26
8.2.1	Input data	26
8.2.1	SSS retrieval algorithm	27
8.3	Models for the Dielectric Constant of seawater at 1.4 GHz	28
8.3.1	Mathematical description.....	28
8.3.2	Functional flow diagram	29
8.3.3	Assumption and limitations	29
8.4	Perfectly flat or ‘specular’ sea surface emission.....	30
8.4.1	Mathematical Description.....	30
8.4.2	Functional flow diagram	33
8.5	Rough Sea surface emission	33
8.5.1	Physics of the problem	33
8.5.2	Wind-induced isotropic emissivity	35
8.5.3	Wind-induced anisotropic emissivity	37
8.5.4	Functional flow diagram	39
8.6	Atmospheric contributions	40
8.6.1	Physics of the problem	40
8.6.2	Effects on the Stokes vector.....	47
8.6.3	Atmospheric Emission	48
8.6.4	Combining Attenuation and Emission	49
8.6.5	Relating Attenuation to Emission	49

8.6.6 Integration of the Radiative Transfer Equation	50
8.6.7 Functional flow diagram.....	55
8.7 Accounting for rotation of the polarization plane in the Stokes vector	55
8.7.1 From surface polarization basis to Ludwig-3 antenna basis.....	56
8.7.2 Faraday Rotation.....	59
8.7.3 Total rotation from surface basis to antenna basis.....	62
8.8 Sum of contributions at the Top of the atmosphere and antenna pattern integration	63
8.9 CIMR Level1b re-sampling approach.....	64
8.10 Sea Surface Salinity inversion algorithm.....	65
9. A Level-2 SSS retrieval prototype algorithm for CIMR	68
9.1) Sea Water Dielectric Constant model at L--band.....	68
9.2) Brightness Temperature of a perfectly flat Sea Surface	74
9.3) Sea Surface Roughness-Induced Brightness temperature	80
9.3.1) Isotropic components of the wind-induced radio-brightness contrast TB	80
9.3.2) Anisotropic components of the wind-induced Radio-Brightness Contrast TB	84
9.4) Atmospheric Contributions.....	87
9.4.1) complex index of atmospheric refraction owing to dry air (molecular oxygen)...	87
9.4.2) Complex index of atmospheric refraction owing to water vapor	90
9.4.3) Complex index of atmospheric refraction due to cloud liquid water	92
9.4.4 Complex index of atmospheric refraction for cloud ice water	94
9.4.5 Complex index of atmospheric refraction owing to rain	95
9.4.6 Example of Atmospheric contributions to TOA Brightness Temperatures.....	97
9.4.6.1 standard 1976 atmosphere profiles	97
9.4.6.2 Evaluation at each vertical level and integration	99
10. Algorithm performance assessment using SCEPS	112
9.1 Geophysical data used to describe the ocean scene	113
9.2 Simulated TOA Tbs over the scene	114
9.3 Simulated instrument Tbs over the scene	116
10.4 SSS retrieval simulations	119
10.4 SSS retrieval simulations: comparison with MRD	121
10.4.1 Error Estimates for individual CIMR L2 SSS	121
10.4.2 Error Estimates for Level 3 CIMR SSS	124
11. Roadmap for Future CIMR SSS ATBD Developments	127
11.1 New Sea water dielectric constant model at L-band.....	127
11.2 Incidence angle & SST dependencies of the roughness correction	127
11.3 Roughness emission azimuthal harmonics in High winds.....	128
11.4 Simplified Atmospheric Corrections	128

11.5 Needed and missing correction: retrieval in coastal areas and closer to the sea ice edge	130
11.6 SSS uncertainty estimation	130
12. References.....	132

1. Abstract

This document provides the theoretical basis for the CIMR salinity retrieval algorithm. The inputs to the algorithm are the CIMR L-band Top Of the Atmosphere (TOA) measurements along with a number of auxiliary products and pre-computed tables of forward model emission and geophysical data. The output is sea-surface salinity and intermediate variables required for the salinity calculation. This is the pre-launch version of the ATBD. Changes made postlaunch will be included as addenda and updated periodically. In particular, the sea water dielectric constant model at L-band and the roughness correction is based on pre-launch information from SMOS, Aquarius, and SMAP missions and changes are likely as soon as data from the radiometer become available.

2. Applicable and reference documents

List of applicable and reference documents

ID	applicable documents
RD-1	C.J. Donlon. Copernicus Imaging Microwave Radiometer (CIMR) Mission Requirements Document. Version 4.0, 2020. [Online; accessed 1 September 2022]. URL: https://esamultimedia.esa.int/docs/EarthObservation/CIMR-MRD-v4.0-20201006_Issued.pdf .
RD-2	J. Tenerelli, The SCEPS Instrument Simulator: Algorithm Theoretical Basis Document, January 15, 2024. https://drive.google.com/file/d/1FzzN3DKDELooB-2uMVXbV42eHhD7i8Cc/view
RD-3	N.Reul and J.Tenerelli, Error Sources for Ocean Surface Salinity Measurements from CIMR TN4, Metrological Analysis of CIMR Radiometry (MACRAD), Apr 2024.
RD.4	SMOS L2 OS Algorithm Theoretical Baseline Document SO-TN-ARG-GS-0007 13 29 April 2016

3. Acronyms

Here follows a formatted list of acronyms

Acronym	Meaning
acdm	Absorption coefficient for color detrital matter
AMSR	Advanced Microwave Scanning Radiometer
BL	Barrier-Layer
BLT	Barrier-Layer Thickness
CAP	Combined Active-Passive
CATDS	Centre Aval de Traitement des Données SMOS
CCI-SSS	ESA Climate Change Initiative-Sea Surface Salinity project
CDTI	Spanish Centre for the Development of Industrial Technology
CIMR	Conical Imaging Microwave Radiometer
CMB	Cosmic Microwave Background
CNES	French Centre National d'Etudes Spatiales
Ch-la	Chlorophyll-a
CONAE	Comisión Nacional
CTD	Conductivity-Temperature-Depth
DIC	Dissolved Inorganic Carbon
EAF-FOV	Extended Alias-Free Field Of View
EASE-grid	Equal-Area Scalable Earth Grid
ECMWF	European Center for Medium-range Weather Forecast
ECV	Essential Climate Variable
ENSO	El Niño Southern Oscillations
EO	Earth Observation
E-P	Evaporation (E) minus Precipitation (P)
EPE	Eddy Potential Energy
ESA	European Space Agency
ESTAR	Electrically Scanning Thinned Array Radiometer
ESTEC	European Space Research and Technology Centre, the Netherlands
EUC	Equatorial UnderCurrent
FOV	Field Of View
GCOS	Global Climate Observing System
GOOS	Global Ocean Observing System
GMF	Geophysical Model Functions
GOSUD	
GODAE	Global Ocean Data Assimilation Experiment
GPM	Global Precipitation Mission
HH	Horizontally-polarized emitted Horizontally-polarized received
HYCOM	HYbrid COordinate Model
IOD	Indian Ocean Dipole
ITCZ	Inter-tropical Convergence Zone

Acronym	Meaning
ITU	International Telecommunication Union
JPL	Jet Propulsion Laboratory
KS	dielectric constant model for sea water from Klein and Swift (1977)
LSC	Land Sea Contamination
MIRAS	Microwave Imaging Radiometer with Aperture Synthesis
MJO	Madden-Julian Oscillation
MW	dielectric constant model for sea water from Meissner and Wentz (2004)
NASA	National Aeronautics and Space Administration
NBC	North Brazilian Current
NCEP	National Center for Environmental Prediction
NEDT	Noise Equivalent Differential Temperature
NOAA	National Oceanic and Atmospheric Administration
NODC	NOAA National Oceanic Data Center
OS	Ocean Salinity
OTT	Ocean Target Transformation
PALS	Passive-Active L-band System
PI-MEP	SMOS Pilot Mission Exploitation Platform
RMS	Root Mean Square
RMSD	Root Mean Square Difference
RFI	Radio Frequency Interferences
RR	Rain Rate
RSS	Remote Sensing System
RSTN	United States Air Force Radio Solar Telescope Network
SAMOS	Shipboard Automated Meteorological and Oceanographic System
SEPSI	Southeastern Pacific SSS Index
SIO	Scripps Institution of Oceanography
SLFMR	Scanning Low Frequency Microwave Radiometer
SMAP	Soil Moisture Active-Passive mission
SMOS	Soil Moisture and Ocean Salinity
SOI	Southern Oscillation Index
SSM/I	Special Sensor Microwave Imager
SSH	Sea Surface Height
SSS	Sea Surface Salinity
SSSA	SSS Anomalies
SST	Sea Surface Temperature
STD	STandard Deviation
SWH	Significant Wave Height
TA	Total Alkalinity
TB	brightness temperature
TC	Tropical Cyclones
TEC	Total Electron Content
TIW	Tropical Instability Wave

Acronym	Meaning
TOA	Top Of the Atmosphere
TOI	Top of the Ionosphere
TSG	ThermoSalinoGraphs
VTEC	Vertical ionospheric Total Electron Content
VV	Vertically-polarized emitted Vertically-polarized received
WOCE	World Ocean Circulation Experiment
WOD	World Ocean Database

4. Definitions used in this ATBD

Here follows a glossary, or list of definitions

Notation	Definition
T_{atm}^{up}	Unpolarized upwelling brightness temperature of atmospheric 1-way emission [K]
τ_d	1-way atmospheric transmittance associated with molecular oxygen absorption [nd]
τ_v	1-way atmospheric transmittance associated with water vapor absorption [nd]
$T_{surf,p}^{tot}$	p-pol brightness temperature of the total sea surface emission (specular+rough+foam) [K]
$R_{surf,p}^{tot}$	reflectivity of the total sea surface (specular+rough+foam) in p-pol
T_{atm}^{dw}	Unpolarized downwelling brightness temperature of atmospheric 1-way emission [K]
T_{erU}	Third Stokes brightness temperature of rough surface emission (surface pol. Basis) [K]
T_{erV}	Fourth Stokes brightness temperature of rough surface emission (surface pol. Basis) [K]
T_{scp}	p-pol brightness temperature of scattered celestial sky radiation (surface pol. Basis) [K]
T_{ssp}	p-pol brightness temperature of scattered solar radiation (sun glint) (surface pol. Basis) [K]
T_s	Sea Surface Temperature [K]
$e_{surf,p}^{tot}$	p (h or v)-pol total sea surface emission (specular+rough+foam) [K]
F_f	Fractionnal area of sea surface covered by foam [nd]
T_{esp}	p-pol brightness temperature of specular emission (surface pol. Basis) [K]
T_{erp}	p-pol brightness temperature of rough surface emission (surface pol. Basis) [K]
$T_{foam,p}$	p-pol brightness temperature of the total foam-covered surface emission (surface pol. Basis) [K]
T_{esh}	H-pol brightness temperature of specular emission (surface pol. Basis) [K]
T_{erh}	H-pol brightness temperature of rough surface emission (surface pol. Basis) [K]
T_{sch}	H-pol brightness temperature of scattered celestial sky radiation (surface pol. Basis) [K]
T_{ssh}	H-pol brightness temperature of scattered solar radiation (sun glint) (surface pol. Basis) [K]
T_{esv}	V-pol brightness temperature of specular emission (surface pol. Basis) [K]
T_{erv}	V-pol brightness temperature of rough surface emission (surface pol. Basis) [K]
T_{scv}	V-pol brightness temperature of scattered celestial sky radiation (surface pol. Basis) [K]
T_{ssv}	V-pol brightness temperature of scattered solar radiation (sun glint) (surface pol. Basis) [K]
T_{ea}	Unpolarized brightness temperature of atmospheric 1-way emission [K]
R_h	Fresnel power reflection coefficient at the surface in H-pol
R_v	Fresnel power reflection coefficient at the surface in V-pol
e_{sh}	Perfectly flat sea surface emissivity in H-pol
e_{sv}	Perfectly flat sea surface emissivity in V-pol

Notation	Definition
e_{rh}	Rough surface emissivity in H-pol
e_{rv}	Rough surface emissivity in V-pol
T_{erU}	Third Stokes brightness temperature of rough surface emission (surface pol. Basis) [K]
T_{erv}	Fourth Stokes brightness temperature of rough surface emission (surface pol. Basis) [K]
F_f	Fractionnal area of sea surface covered by foam [nd]
T_s	Sea Surface Temperature [K]
U_{10}	10-m height Sea surface wind speed modulus [m/s]

5. Introduction, purpose and scope

The purpose of this Algorithm Theoretical Baseline Document (ATBD) is to establish the procedure that will be used in the CIMR mission to generate the Sea Surface Salinity (SSS) data from brightness temperatures (Tb) recorded by the CIMR L-band radiometer. The historical satellite SSS “Background” and justification of selected algorithm are first provided. As described in the “Level-2 product definition” section, the output product (CIMR SSS Level 2 SSS product) will consist of files containing half-orbit data (from pole to pole) on a geographical grid (e.g. EASE2-like for Polar Regions, Equal Area Cylindrical projection) defined by the level 1c grid, itself defined by the CIMR Level 1b to Level 1C re-sampling approach.

As it is not possible to transform the brightness temperatures Tb into SSS through a univocal mathematical expression. L-band emission of the sea surface is computed using a series of mathematical models that have as independent variables the different geophysical parameters (including SSS) that determine this emission. Some of these parameters are obtained from sources external to CIMR (sky maps; atmospheric profiles) or from CIMR data directly (Sea Surface Temperature, surface wind speed,...), and for SSS a guessed value can be considered. The computed Tb, for all observation configurations that correspond to the specific satellite passage, are compared to the measured ones, and then the independent variables are modified in an iterative process until reaching the maximum similarity between both Tb values. The SSS that corresponds to this situation is the value retrieved from CIMR.

In the “Baseline Algorithm Definition” section, a detailed description of all the parts of the algorithm, the different modules or sub-models that are used to compute the different contributions to sea surface Tb as well as the procedures to compare it with the measured Tb and the iterative convergence method.

In the Algorithm Input and Output Data Definition, we define all needed input and output data.

The Intergovernmental Oceanographic Commission adopted the new International Thermodynamic Equation of Seawater - 2010 that describes salinity through the Absolute Salinity definition in g/kg instead of Practical Salinity (PS Scale - 78) to take into account the spatial variability of seawater composition and to use IS units. However, measuring systems, both in situ and remotely sensed, will continue being based on conductivity, so all instruments and data bases will deliver practical salinity as before. For historical reasons, all the SSS data processing algorithms presented here use practical salinity regardless of labels in different modules (no units/psu/pss/pss-78). CIMR is a data provider and users may apply the new TEOS-2010 formulae to convert conductivity-based practical salinity to the more correct Absolute Salinity values when appropriate.

In §9, a Level-2 SSS retrieval prototype algorithm for CIMR is proposed in the form of python codes for the different parts of the algorithm. In §10, the algorithm performance is assessed through end-to-end retrieval simulations and assessment of uncertainties due to several error sources is performed to test how MRD requirements shall be met. A roadmap for future algorithm developments is then given in §1A. References are provided in a last section.

6. Background and justification of selected algorithm

6.1 Introduction

Ocean salinity is a key physical-chemical variable that critically contributes to the density-driven global ocean circulation and the Earth's climate [[Siedler et al., 2001](#)]. The Sea Surface Salinity (SSS) is affected by (and thus reflects) the air-sea freshwater fluxes (Wust [[1936](#)]; Schmitt [[2008](#)]; Durack *et al.* [[2012](#)]; Skliris *et al.* [[2014](#)]; Zika *et al.* [[2015](#)]), ice formation/melting, river runoff, horizontal advection and vertical exchanges through mixing and entrainment. It also provides fundamental information for ocean bio-geochemistry through its links with the carbonate system (Land *et al.* [[2015](#)]; Fine *et al.* [[2017](#)])). Stable fresh surface salinity layers (such as river plumes, rain-induced lenses) on top of saltier and denser deep waters can inhibit the upper-ocean mixing generated by intense atmospheric events (e.g., wind bursts, tropical cyclones) due to so-called barrier layer effect (e.g., Lukas and Lindstrom [[1991](#)]; Balaguru *et al.* [[2012](#)])). This suggests that mixed layer salinity can actively impact air-sea interactions from local to synoptic scales. Given its importance for many key ocean and climate processes, the SSS has been recognized as an Essential Climate Variable (ECV) by the Global Climate Observing System (GCOS) program. [[Bingham et al., 2002](#)] examined the global distribution of historical (1874-1998) in situ SSS observations measured at 5 m or less in depth from the World Ocean Database 1998 (WOD98) and showed how poorly SSS was sampled by the end of the 1990s, despite a peak period of ocean sampling (including near surface salinity) during the World Ocean Circulation Experiment (WOCE, 1990-1998). The Global Ocean Data Assimilation Experiment (GODAE) group, therefore, estimated that it would be necessary to develop global SSS measurements from both in situ sensor networks and dedicated satellite missions to reach an accuracy of about 0.1-0.2 pss at monthly and $100 \times 100 \text{ km}^2$, or 10-day and $200 \times 200 \text{ km}^2$ scales. Tremendous efforts to reach this goal using in situ sensor networks have been carried out by the ocean science community since the early 2000s. At global scale, the large increase in salinity data sampling is dominantly associated with the invention and deployment of the Argo profiler network. Since reaching its full planned capacity in 2007, the network includes ~3000 Argo floats in the global Ocean providing at least one salinity cast every 10 days in a $3^\circ \times 3^\circ$ cell (see Notarstefano [[2022](#)].. In addition to Argo floats which profile to the top 2 km of the global ocean column, near surface salinity is monitored by thermosalinographs (TSG) on board numerous ships of opportunity and research vessels. These TSGs are installed and maintained on board ships via international programs such as the Global Ocean Surface Underway Data (GOSUD; Alory *et al.* [[2015](#)]) and the Shipboard Automated Meteorological and Oceanographic System (SAMOS; Smith *et al.* [[2009](#)]), as well as a growing number of deployments of surface drifters equipped with salinity sensors.

Despite its oceanographic importance, SSS is an ocean ECV that only started to be estimated from Space about fourteen years ago with the launch of the Soil Moisture and Ocean Salinity (SMOS) mission by the European Space Agency (ESA) in

November 2009. The SMOS mission was then followed by the NASA/CONAE Aquarius/SAC-D mission, also focused on the sea surface salinity. Both missions had an overlapping period between June 2011 and mid-2015. Next came the NASA Soil Moisture Active-Passive (SMAP) mission launched in early 2015, which also monitors SSS. SMOS and SMAP operation periods overlapped with Aquarius only during about four months (February to June 2015). The primary sensors onboard these three missions are L-band microwave radiometers operating at ~ 1.4 GHz (wavelength=21cm). When accurate corrections for external contributions to the measured radiometer signal are applied (e.g., radiation from the Sun and celestial radio sources, reflection/emission due to sea surface roughness, and temperature), the SSS can be estimated from L-band brightness temperature T_B (Font *et al.* [2004]; Lagerloef *et al.* [1995]). The feasibility of the measurement of SSS at L-band was demonstrated in the 1970s in a number of field campaigns from aircraft (Droppleman *et al.* [1970]), from a bridge which spans the Cape Cod canal (Swift [1974]), and even with a satellite radiometer from the short-lived (2-week) Skylab S-194 mission (Lerner and Hollinger [1977]). It took more than 40 years after the aforementioned pioneer experiments to develop and implement instruments to measure SSS regularly from space with sufficient accuracy and spatial resolution to address the GODAE recommendation. Two major technological factors limit L-band SSS measurements from space. First, at low microwave frequencies (decimeter wavelengths), classical radiometer sensors require large antenna size of ~ 3 to 8 m in diameter to meet a useful spatial resolution on the ground (100-150 km at most, 30-50 km wished for). Such large antenna technologies were not available before the late 1990s.

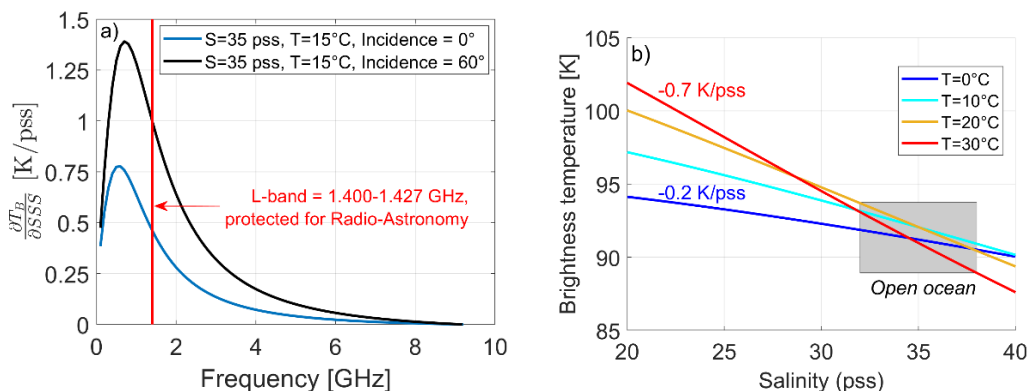


Figure 1: a) Sensitivity of the ocean surface microwave brightness temperature to Salinity (First Stokes parameter) as a function of electromagnetic frequency and incidence angle (blue curve=0°, black curve=60°) and for a water body with salinity of 35 pss and temperature of 15°C. b) First Stokes parameter divided by 2 of the Brightness temperature changes at 1.4 GHz and nadir of the perfectly flat sea surface as a function of salinity (x-axis) and sea surface temperature (colors). The gray domain indicates the range of SSS values mostly encountered in the open ocean.

Second, while being optimal in low microwave frequencies (see Figure 1), the sensitivity of the sea surface brightness temperature to salinity at 1.4 GHz and vertical (VV) polarization varies only between $\partial T_B / \partial SSS \sim -0.5$ to -1 K/pss for incidence angles from 0° to 60° at characteristic ocean conditions (SSS= 35 pss and Sea Surface Temperature SST=15°C). This sensitivity to SSS remains relatively small compared to (i) noise characteristics of available radiometers (~ 0.3 to 2 K) and (ii) the small range of natural variability of SSS in the open ocean (32 to 38 pss). Finally, as illustrated in Figure 1.b, $\partial T_B / \partial SSS$ also decreases with decreasing SST from ~ -0.7 K/pss at 30°C to ~ -0.2 K/pss at 0°C, making SSS estimation in the high latitude cold waters even more

challenging than in the tropical seas. Given the sensitivity of T_B to salinity at 1.4 GHz, very low noise radiometers and/or a large number of T_B observations for a given ocean scene within short integration times (~a few seconds) are required for accurate SSS estimations. Therefore, salinity satellite mission objectives are generally expected to be reached for SSS products obtained after spatio-temporal averaging of in-swath instantaneous data.

6.2 Historical Heritage

In the late 1960s, Siroonian [1968] and Paris [1969] recognized that ocean surface microwave emission in the 1 to 3 GHz range had measurable sensitivity to changes in ocean SSS. The first airborne salinity measurements were demonstrated in 1970 by Droppleman *et al.* [1970]. Combining aircraft mounted 1.4 GHz microwave and 11 μm infrared radiometers, they were able to observe strong SSS gradients near the mouth of the Mississippi River, and thus demonstrate the feasibility of 1.4-GHz passive radiometers to detect sea water salinity gradients. Multi-frequency (L-, X- and K-bands) microwave radiometer observations conducted by Hollinger [1971] from a research tower located off the island of Bermuda revealed the potential effect of sea surface roughness on L-band T_B for wind speed conditions varying from calm to 15 m/s. Thomann [1976] used a system similar to Droppleman *et al.* [1970] to map ocean surface salinity in the Gulf of Mexico. As reviewed in Goodberlet *et al.* [1997], these early instruments could achieve an acceptable measurement accuracy only by averaging over time periods from 12 to 16 seconds. The averaging time was later reduced below 1 second using a NASA Langley built precise radiometer system (Blume *et al.* [1978]; Blume and Kendall [1982]) operating at 1.4 GHz (L-band) and 2.65 GHz (S-band). Its improved noise characteristics (and lower integration times) allowed improvement in spatial resolution and measurements in the Chesapeake Bay SSS that resolved ~0.5 km spatial scales. The dual-frequency radiometer system was also successfully operated from an aircraft (Kendall and Blanton [1981]) to measure quasi-synoptic salinity changes induced by the Savannah River plume along the coast of Georgia. A key model component for the salinity retrieval algorithm from microwave radiometer data is the model for the sea water dielectric constant, ϵ_{sw} . The semi-empirical Debye model was first proposed by Stogryn [1971] and re-analyzed by Klein and Swift [1977] to include new S-band and L-band data from the NASA 2-band radiometer. Shutko *et al.* [1982] further examined and refined the dependencies of ϵ_{sw} on electromagnetic frequency, water temperature, and salinity. In addition, near nadir L-band measurements from the Bering Sea aircraft experiments as reported by Webster *et al.* [1976] allowed for better characterization of wind speed dependence of the surface emissivity.

First attempts to measure SSS from space took place in 1968 aboard the Soviet Cosmos 243 and in 1973 aboard the Skylab S-194 satellite missions (Lerner and Hollinger [1977]). They utilized nadir looking L-band horizontal (HH) microwave radiometers with 3dB beam width of 15° corresponding to ~110 km ground footprint. Unfortunately, only a very limited amount of L-band radiometer data was collected and there were no in situ measurements available to validate SSS retrievals estimated from the satellite data. Nevertheless, the retrieved SSS was found correlating with climatological in situ salinity. Overall, these experiments showed that open sea SSS (i.e., away from the land and coasts) could be measured with an accuracy of ~2 psu, a promising early result. Based on these first aircraft and satellite experiments, Swift and McIntosh [1983] suggested a revised satellite concept to achieve an ideal precision

of about 0.25 pss with a footprint spatial resolution of ~100 km. However, at that time, space agencies were primarily devoting efforts to develop missions to measure surface temperature (Advanced Very High Resolution Radiometers (AVHRRs) and Along-Track Scanning Radiometers (ATSRs)), surface dynamic topography (Geosat (GEOdetic SATellite)), wind stress (SEASAT A Scatterometer (SASS)), ocean color (Coastal Zone Color Scanner (CZCS)), and sea ice (scanning multichannel microwave radiometer (SMMR)). Mainly because of the technological challenges associated with the launch of sensors with large antenna size and the need for high radiometric sensitivity, salinity remote sensing was considered too costly and not given a high priority in the early 1980s. Interest in salinity remote sensing was renewed in the late 1980s with the development of an airborne demonstration instrument called the Electrically Scanning Thinned Array Radiometer (ESTAR), which was operated at 1.4 GHz and used the concept of aperture synthesis (Le Vine *et al.* [1990]) allowing an increase in cross-track spatial resolution. Small salinity variations typical of the open ocean were retrieved from the data acquired by the ESTAR interferometer during flights across a coastal current in Delaware and the Gulf Stream (Le Vine *et al.* [1998]). Such a system demonstrated that it was feasible to achieve high spatial and radiometric resolution at a reasonable cost for a potential 1.4 GHz satellite radiometer design. By the mid-1990s, the Scanning Low Frequency Microwave Radiometer (SLFMR) was built (Goodberlet and Swift [1993]) based on the similar concept as the ESTAR but with an improved radiometric resolution and adapted for light aircraft. Salinity in coastal and estuarine waters on the U.S. Atlantic coasts, as well as in the Australian Great Barrier reef waters have been mapped successfully using the SLFMR data acquired during several airborne campaigns (Robinson [1985]; Le Vine *et al.* [1998]; Miller *et al.* [1998]; Burrage *et al.* [2003]; Miller and Goodberlet [2004]; Perez *et al.* [2006]).

A detailed review of remote sensing of SSS in coastal waters is provided in Klemas [2011]. A Passive-Active L-band System (PALS) (Wilson *et al.* [2003]) providing coincident scatterometer and radiometer airborne L-band data was developed to better characterize the sea surface roughness impact on L-band TB. This instrument was deployed on ocean flights across the Gulf Stream in an attempt to illustrate the use of active scatterometer data to correct the impact of surface roughness on passive radiometer data (Yueh *et al.* [2001]). The PALS design and data provided the basis for the NASA Aquarius and SMAP instrument designs. In 1995, during the “Soil Moisture and Ocean Salinity” Workshop organized at the ESA ESTEC (European Space Research and Technology Centre, Noordwijk, the Netherlands), possible techniques to remotely measure SSS from space were discussed. The two most suitable approaches were identified to be L-band microwave radiometry using either real or synthetic, aperture antenna design. The use of a real aperture antenna with moderate size (diameter < 3 m) eases sensor integration into a launch vehicle and better fulfills satellite weight constraints but results in lower spatial resolution on the ground. This option was realized for the Aquarius mission with a moderately large antenna (reflector diameter ~2.5 m) used in the push broom mode. Another concept was realized for the SMAP mission, which has a relatively large deployable mesh antenna reflector of 6 meters in diameter. Both Aquarius and SMAP instruments were designed with combined active and passive measurements. The second approach involves the use of interferometric radiometers with a synthetic aperture antenna allowing T_B measurements at higher spatial resolution than with a real-aperture antenna of the same size. The ESTAR interferometric 1-D imaging concept evolved into a 2-D imager in the mid-1990s (Goutoule *et al.* [1996]). Its airborne prototype was made and

operated (Bayle *et al.* [2002]) and then further evolved into the Microwave Imaging Radiometer with Aperture Synthesis (MIRAS), the instrument carried by the SMOS mission.

6.3 Justification of selected algorithm

The new satellite SSS era started with the Soil Moisture and Ocean Salinity (SMOS) mission, launched in 2009 under the auspices of the European Spatial Agency (ESA), the French Centre National d'Etudes Spatiales (CNES), and the Spanish Centre for the Development of Industrial Technology (CDTI). Followed by the National Aeronautics and Space Administration (NASA) Aquarius instrument from mid-2011 to mid-2015, it is today complemented by the NASA Soil Moisture Active-Passive (SMAP) mission. Initially dedicated to Soil Moisture measurements only, SMAP applications have been extended to include the SSS, which is available since early 2015. All instruments on-board these different missions follow the previously described early 1970s historical heritage that demonstrated how passive microwave radiometer observations in the L-band (frequency~1.4 GHz, wavelength~21 cm) could be used to retrieve SSS. The SSS measurement principle was successfully developed and demonstrated in the 1970s from various platforms (land-based bridge, aircrafts, towers, short-lived satellites, etc). The long delay until the final development and launch of the first satellite salinity sensor was mainly dictated by technological challenges associated with space delivery and deployment of large antennas. Indeed, to achieve a proper pixel resolution, a very large size (~3-8 m) radiometer antenna is needed for 1.4 GHz operations even from low polar orbits. There are major technological differences but also similarities between the three first satellite salinity missions. SMOS and SMAP spatial resolution (~40 km) is a factor 2-3 higher than Aquarius spatial resolution (~100 km - 150 km). Moreover, with their large swaths, observations cover almost the full globe in 3 days, while 7 days were needed in the case of Aquarius. Yet, Aquarius radiometric noise was significantly lower than SMOS, or SMAP, radiometric noise. For SMOS, image reconstruction errors are sources of specific and variable noise in the T_B images (e.g., sun and land image aliasing in ocean scenes, noise floor errors ...) and impact the quality of retrieved SSS from this sensor. But SMOS multi-angular viewing capability also provides a way to mitigate the noise in individual samples, thanks to a large number of T_B acquisition for a given ocean target pixel. The Aquarius antenna emissivity was negligibly small, while the SMAP mesh reflector has an emissivity of about 0.2%, which needs to be accounted for in salinity retrieval. Moreover, the simultaneous acquisition of scatterometer and radiometer observations by Aquarius significantly helped to improve the correction for sea surface roughness effect. For SMOS and SMAP, retrieval algorithms must rely on external surface wind vector data, not always of sufficiently high quality to well characterize the actual impact of roughness on L-band passive sensors. For CIMR the case is different as higher frequency channels can provide quasi-simultaneous SST and wind data.

6.3.1 Model for the dielectric constant of the seawater at L-band

The relative permittivity (also called dielectric constant) of the seawater, $\epsilon_{sw}(f, S, T)$ is a complex function dependent on f , the electromagnetic frequency, as well as, temperature T , and, salinity S . It is a key component of the radiative transfer forward model used for sea surface salinity retrieval from L-band radiometer data, as the accuracy of SSS retrievals strongly depends on how well the dielectric constant is

known as a function of these two geophysical parameters (Lang *et al.* [2016]). Models for $\epsilon_{sw}(f, S, T)$ at frequency $f=1.4$ GHz are still uncertain, particularly at low ($\leq 8^{\circ}\text{C}$) and high ($\geq 28^{\circ}\text{C}$) SST. $\epsilon_{sw}(f, S, T)$ can be estimated at any frequency f within the microwave band from the Debye [1929] expression involving ϵ_{∞} , the electrical permittivity at very high frequencies, ϵ_s the static dielectric constant, τ the relaxation time, σ the ionic conductivity, and ϵ_0 the permittivity of free space, where ϵ_s , τ and σ are functions of temperature T and salinity S . At the time the first salinity mission was developed, these functions had been evaluated historically by Stogryn [1971], Stogryn *et al.* [1995], Klein and Swift [1977], and Ellison *et al.* [1998]. Klein and Swift [1977] (denoted KS hereafter) modified the Stogryn [1971] model by using a different expression for the static dielectric constant $\epsilon_s(S, T)$, based on Ho and Hall [1973] and Ho *et al.* [1974] measurements at 2.6 and 1.4 GHz, respectively. The KS and Stogryn $\epsilon_{sw}(f, S, T)$ models are valid for frequencies f ranging from L- to X-bands (Meissner and Wentz [2004]; Meissner and Wentz [2012]; Meissner *et al.* [2014]). Following SMOS pre-launch comparisons and analyses (Camps *et al.* [2004]; Wilson *et al.* [2004], Blanch and Aguasca [2004]), the KS model was selected in the Level 2 Ocean Salinity (OS) processor for the SMOS mission in the first phases post-launch (Team and others [2016]).

An alternative model function developed by Meissner and Wentz [2004] (denoted MW hereafter) fits the dielectric constant data to a double Debye relaxation polynomial that performs best at higher frequencies. The seawater dielectric data were obtained by inverting T_B measurements from the Special Sensor Microwave Imager (SSM/I) at frequencies higher than 19 GHz; measurements from Ho *et al.* [1974] were used to derive the model at the lower frequencies. The MW model function was recently updated by providing small adjustments to the Debye parameters based on including results for the C-band and X-band channels of WindSat and AMSR (Meissner and Wentz [2012]; Meissner *et al.* [2014]). The MW model is used in the Aquarius and SMAP SSS retrieval algorithms (Meissner *et al.* [2018]). Dinnat *et al.* [2014] analyzed the difference in SSS retrieved by SMOS and Aquarius radiometers and found that both instruments observe similar large scale patterns, but also reported significant regional discrepancies (mostly between $+/- 1$ pss). SMOS SSS was found generally fresher than Aquarius SSS (within 0.2–0.5 pss depending on latitude and SST), except at the very high southern latitudes near the ice edge and in a few local (mostly coastal) areas. It was found that the differences exhibit large-scale patterns similar to SST variations. To investigate its source, Dinnat *et al.* [2014] reprocessed the Aquarius SSS, including the calibration, using the KS ϵ_{sw} model that is used in SMOS processing. This reprocessing decreases the difference between Aquarius and SMOS SSS by a few tenths of a pss for SST between 6°C and 18°C while warmer waters show little change in the difference. Water colder than 3°C shows mixed results, probably due to a complex mix of error sources, such as the presence of sea ice and rough seas. The comparison of the reprocessed Aquarius SSS with in situ data from Argo shows an improvement of a few tenths of a pss for temperatures between 6°C and 18°C . In warmer waters, both the nominal and reprocessed Aquarius data, as well as SMOS data, have a fresh SSS bias. For very cold waters (less than 3°C), the reprocessed Aquarius data using the KS model show significant degradation of the SSS in comparison with the Argo, in turn suggesting that the KS model might be in error in the lowest sea surface temperature regime. Direct laboratory measurements of the ϵ_{sw} at 1.413 GHz and SSS=30, 33, 35, and 38 (Lang *et al.* [2016]) were used to develop a new model (Zhou *et al.* [2017]) by fitting the

measurements with a third-order polynomial. This new L-band ϵ_{sw} model has been compared with KS and MW. The authors claimed that this new model function gives more accurate SSS at high (25°C to 30°C) and low (0.5°C to 7°C) SSTs than other existing model functions. Laboratory measurements at low SSS lead to a small increase in the accuracy of the model function. Although the model showed improvements in salinity retrieval, it had an inconsistent behavior between partitioned salinities. To overcome these problems, two new parametrizations were recently developed based on one hand on SMOS satellite multi-angular brightness temperature measurements by Boutin *et al.* [2021] (BV), and on the other hand on new George Washington laboratory measurements by Zhou *et al.* [2021] (hereafter denoted GW2020). These two approaches are fully independent. The brightness temperatures T_B simulated through the BV and GW2020 parametrizations agree particularly well for most SSS and SST conditions commonly observed over the open ocean, and better than with earlier parametrizations previously used in the SMOS, SMAP and Aquarius SSS retrievals. Nevertheless, uncertainty remains below 10°C where a $\sim 0.1\text{K}$ relative difference between the two models is observed.

Recently, Le Vine *et al.* [2022] compared available models in the context of how well they represent the dielectric constant of sea water at 1.4 GHz. Among the criteria applied were the recent measurements at the George Washington University of the dielectric constant at 1.4 GHz. As reviewed, in the two models, BV and MW, parameters were tuned to optimize the science retrieval algorithm by choosing the model parameters to minimize the differences between radiative transfer simulations of the brightness temperature and the T_B actually observed by the satellite. These two models are close to the measurements but diverge in some significant respects. This is particularly evident in the temperature dependence of the real part. The BV model was tuned to optimize the retrieval of salinity from SMOS observations of brightness temperature at 1.4 GHz. The tuning was done on the temperature dependence of the static term, which is strongly coupled to the real part. The MW model is a double Debye resonance model intended to cover a large range of higher frequencies and the tuning was done to fit the satellite observations from Windsat and SSM/I in this higher range and particularly near 37 GHz.

Three of the models have been used in remote sensing of salinity: KS and BV have been used in SMOS retrievals and MW was used for Aquarius and is now used for retrieving salinity from soil moisture active passive (SMAP). In addition, a combination of the MW and KS model has been used in the combined active passive (CAP) algorithm for retrievals from Aquarius and SMAP. While these models have been used quite successfully to retrieve salinity, this success does not guarantee that they are a good representation of the dielectric constant of sea water. For salinity typical of the open ocean, $32 < S < 38$ psu, the differences in the dependence of the models on S are on the order 0.1 K, which is acceptable. As found by Le Vine *et al.* [2022], except for cold temperatures, KS appears to be a better fit to the dielectric constant at 1.4 GHz. Because BV and MW are satellite sensor-dependent and tuned to best fit their specific datasets, and because KS seems biased in low SSTs, as a first step, we plan here to rely on the GW2020 empirical model based the most recent George Washington laboratory measurements as described in Zhou *et al.* [2021]. At the time this ATBD was developed, the recently revised parameterization, hereafter denoted BVZ (Boutin, Vergely, and Zhou, 2023) was not yet available. As stated in the roadmap, noting that this new parametrization significantly improved the SSS retrieval from SMOS in the 5°C - 15°C SST

range, we advise to update the GW2020 L-band sea water dielectric constant model with this new BVZ model in future algorithm developments for CIMR.

6.3.2 Model for correcting the sea surface roughness emission

The current status in the development of forward models to estimate and correct for the sea surface roughness contribution to L-band T_B measured at antenna level can be summarized as follows. To first order, Geophysical Model Functions (GMF) developed are dependent on the auxiliary surface wind speed product used to generate them. There is however a general good agreement between L-band GMFs used in the latest versions of Aquarius, SMAP, and SMOS products (V5 for Aquarius, RSS V6 for SMAP, JPL V4 for SMAP and ESA V772 for SMOS) (Yin *et al.* [2016]; Meissner *et al.* [2018]). The JPL CAP algorithm developed for Aquarius data (Yueh *et al.* [2014], Fore *et al.* [2016]) relies on a purely-empirical GMF for the roughness correction. In all other operational algorithms, a semi-empirical two-scale scattering model approach is used for that correction, such as in [Yin *et al.*, 2016] for SMOS, and in [Meissner *et al.*, 2018] for SMAP and Aquarius. Development and analysis of the two-scale model for ocean waves and resulting microwave ocean emissivities were presented in (Yueh [1997]) and (Yueh *et al.* [1994], Yueh *et al.* [1999]; Johnson [2006]; Ma *et al.* [2021]; Lee and Gasiewski [2022]), within which were published two-scale model algorithms that have been successfully used to date for the prediction of ocean wave influences on surface emission. Ocean foam (i.e., white capping) is an air-sea mixture caused by ocean wave breaking and is an additional surface process that strongly increases ocean surface emissivity (Monahan and O'Muircheartaigh [1986]; Stogryn [1972]; Reul and Chapron [2003]; Camps *et al.* [2005]) at microwave frequencies due to its near-blackbody behavior. As wind speed increases, ocean foam coverage also increases, resulting in a large discrepancy between two-scale emissivity calculations made with and without consideration of foam coverage. The quasi-blackbody models used for both foam emissivity and coverage are in themselves of limited accuracy due to the paucity of in situ observations for both foam coverage and emissivity that have been able to be made in conjunction with brightness temperatures from passive microwave instruments. In spite of numerous efforts to derive a suitable empirical relationship between foam coverage and ocean surface wind speed (Monahan and O'Muircheartaigh [1986]; Erickson *et al.* [1986]; Asher *et al.* [2002]; Bondur and Sharkov [1982]; Anguelova and Webster [2006]; Callaghan *et al.* [2008]), there is to date no universally accepted relationship between them due to the variable conditions under which foam is produced, as well as its spatial inhomogeneity. This shortcoming is especially true for breaking waves caused by shoaling. Smith *et al.* [2008] found that the differences in surface-referenced microwave brightness temperatures between WindSat observations and a two-scale model developed by Johnson [2006] were significant, especially in the zeroth-azimuthal-harmonic components of ocean brightness at a wind speed of 8–20 m/s. The discrepancy was largely due to foam coverage and emissivity models. They concluded that an empirical tuning process using observed satellite data is needed to model ocean surface emissivity with enough precision for general retrieval and data assimilation applications.

The limitations on the various purely physical published models on the ocean surface emissivity include a limited range of validity in frequency and incidence angle. Combined physical and empirical models have been used to correct for these shortcomings but do not necessarily permit extension of the models to arbitrary frequencies and incidence angles, as required for the design and development of new observation systems.

In this algorithm for CIMR, a full Stokes vector model for ocean surface emissivity based on empirical GMFs derived from SMOS, Aquarius and SMAP are used to model ocean surface emissivity with enough precision for general retrieval and data assimilation applications. Note that remaining uncertainties for the roughness-induced radio-brightness contrast are still the subject of on-going research efforts.

6.3.3 Model for other geophysical contributions

In the SSS retrieval algorithm, accurate corrections associated with ionospheric, atmospheric, solar, and sky radiation contributions to the antenna measured brightness are needed.

The ionospheric correction commonly involve the use of the ratio of the third Stokes (U) parameter to the difference between the vertical and horizontal polarization channels (Yueh [2000], Le Vine and Abraham [2002], Vergely *et al.* [2014]). This helps to infer the rotation angle (geometry plus Faraday) across the ionosphere. Again, accurate calibration of the third Stokes parameter is still challenging. The ionospheric rotation estimates also rely on the first guess data, including the Total Electronic Content (TEC) and geomagnetic field data (Vergely *et al.* [2014]) for which uncertainties still remain.

For L-band, sources of atmospheric attenuation are due to absorption by oxygen, water vapor, and liquid water. The contribution from the atmosphere is found to be a few Kelvins on average, rather stable in space and time, with the dominant source of signal associated with oxygen. As presently implemented, atmospheric corrections used in salinity retrieval algorithms all rely on time interpolated and integrated vertical profiles of atmospheric pressure, temperature, relative humidity, and cloud water mixing ratio obtained from numerical weather forecast models (ECMWF or NCEP). The overall error in salinity retrievals due to the atmosphere is estimated to be less than 0.2 psu (e.g., Meissner *et al.* [2018]).

Correcting for the Sun, and, Sky direct and reflected radiation further demands accurate characterization of the antenna patterns, and sun T_{sun} , and sky T_{sky} at the time of acquisition. Models for the bi-static scattering coefficients of the sea surface at L-band are then also needed. Sun flux measurements made by the United States Air Force Radio Solar Telescope Network are used but remain uncertain to within 10%, which is significant for salinity retrieval algorithms as the Sun is an extremely bright source at 1.4 GHz ($\sim 10^6$ K). Bi-static sea surface scattering coefficient models are generally estimated using the Physical Optics (Reul *et al.* [2007]), or the Geometric Optics approaches (Khazâal *et al.* [2016], Meissner *et al.* [2018]). A practical rule for L-band measurements is to consider a reduced, by about 50 %, surface slope variance as a function of wind speed, as compared to optical data. Applied corrections remove the reflected galactic radiation correctly to about 90% as estimated in the Aquarius and SMAP cases (e.g., Meissner *et al.* [2018]). Remaining uncertainties from the rough ocean surface scattering models in the L-band, the T_{sky} map of the celestial sky, and the antenna gain pattern appear as sources of remaining ascending-descending biases in all the satellite data. Empirical corrections to best mitigate these remaining signals are currently under investigation. They are based on either alternative antenna gain-weighted sky maps obtained from the satellite data or rely on the multiple view capabilities of the instrument (e.g., use of the fore and aft-look for SMAP, and for CIMR). Antenna gain-weighted sky maps can be derived from the accumulated radiometer direct observation of the sky as recorded during the regular cold-sky calibration maneuvers.

Being significantly warmer than the ocean water at L-band, land (and sea ice) surfaces can significantly impact the ocean T_B measured, and this over a 400 to 1000 km-wide band off the coasts (or sea ice border) of the major land (ice) masses. A correction for land entering the antenna side-lobes when the sensor observation gets close to the land has been derived from simulated T_B (Meissner *et al.* [2018]). Such empirical corrections appear to be efficient globally to reduce the land-contamination biases in satellite SSS. Yet, uncertainties remain in the antenna gain patterns and the reference geophysical fields (e.g. coastal SSS, land T_B), which are used to model the expected ocean-land transition signal. Alternatively, corrections can also be successfully applied after the SSS has been retrieved from the uncorrected T_B . These corrections, based on filtering largely biased estimates, are empirical adjustments, or based on advanced filtering of the salinity products (e.g., Boutin *et al.* [2018], Olmedo *et al.* [2017], Olmedo *et al.* [2018]). Accordingly, while the absolute salinity retrievals can degrade quickly as the footprint approaches land, the SSS Anomalies (SSSA) derived from satellites generally show coherent and informative signatures in many coastal zones (Boutin *et al.* [2018]; Grodsky *et al.* [2018]; Grodsky *et al.* [2019]).

7. Level-2 product definition

The Level-2b SSS product is obtained through application of the SSS retrieval algorithm, given the Level-1b TBs after proper resampling (Level-1C). The product is provided in the L-band grid of the CIMR instrument ($x_{dimgrid}, y_{dimgrid}$). There is also one SSS retrieval per CIMR look direction (aft and fore views). The product is provided in netCDF format and contains the variables listed in Table 1.

Table 1: CIMR Level-2 product definition

name	description	Units	dimensions
time	seconds observation since YYYY-MM-DD 00:00:00 UTC.	of seconds	[look, $x_{dimgrid}, y_{dimgrid}$]
lon	longitude. range: [0°,360°]	degrees East	[look, $x_{dimgrid}, y_{dimgrid}$]
lat	latitude. range: [90°S,90°N]	degrees North	[look, $x_{dimgrid}, y_{dimgrid}$]
sea_surface_salinity	sea salinity	surface pss	[look, $x_{dimgrid}, y_{dimgrid}$]
sea_surface_salinity_uncertainty	sea salinity uncertainty	surface pss	[look, $x_{dimgrid}, y_{dimgrid}$]
sea_surface_salinity_quality_level	Flag indicating n/a the quality level of the SSS retrieval	n/a	[look, $x_{dimgrid}, y_{dimgrid}$]
sea_surface_temperature	sea tempearture	surface Kelvin	[look, $x_{dimgrid}, y_{dimgrid}$]
wind_speed	sea speed	surface wind m/s	[look, $x_{dimgrid}, y_{dimgrid}$]
wind_direction	sea direction	surface wind meteorological convention. 0°: wind coming out of N, +90° : wind coming out of E, etc. range: [0°,+360°]	[look, $x_{dimgrid}, y_{dimgrid}$]

8. Baseline Algorithm Definition

8.1 Overview

The present algorithm aims at retrieving the surface salinity by finding the best-fit solution to minimize the difference between the CIMR L-band Top of the Atmosphere brightness temperature Stokes vector data and a forward radiative transfer model.

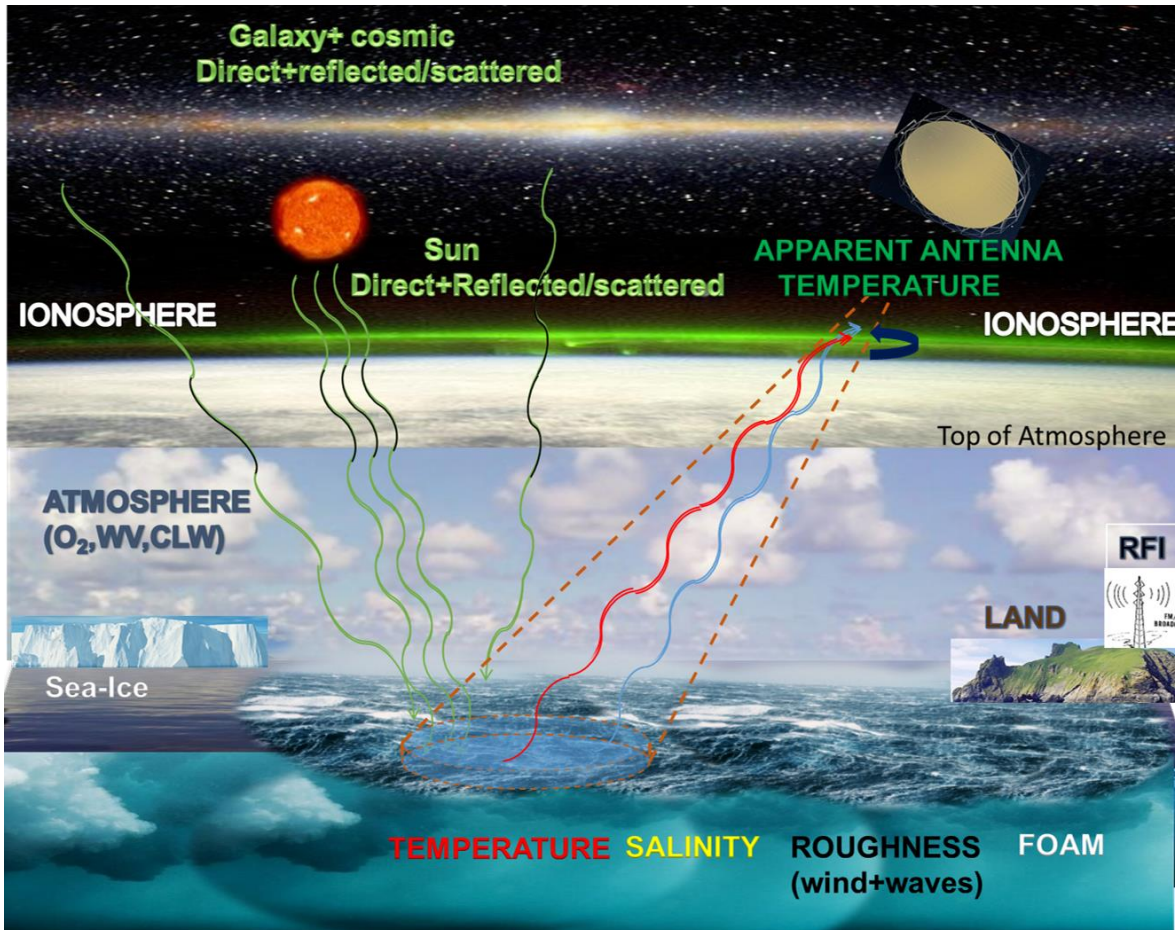


Figure 2: Major signals received by a Space borne L-band microwave radiometer

As illustrated in Figure 2, several geophysical parameters contribute significantly to T_B measured by a satellite microwave L-band radiometer at antenna level (e.g., see Yueh *et al.* [2001]; Font *et al.* [2004], Reul *et al.* [2020]): these include sea surface salinity and temperature, sea surface roughness and foam, atmospheric water vapor, cloud liquid water, oxygen, ionospheric Total Electronic Content, sea surface scattered sky and sun radiations. To properly retrieve surface properties such as the ocean surface salinity from the radiometer data, these contributions need to be accurately known and used in corrections of measured, or forward model simulations, of antenna T_B . They include:

- the direct and sea surface reflected/scattered solar and sky emission (Wentz [1978]; Le Vine *et al.* [2005]; Reul *et al.* [2007]; Reul *et al.* [2008]; Tenerelli *et al.* [2008]; Dinnat and Le Vine [2008]),

- the Faraday rotation in the ionosphere (Yueh [2000]; Le Vine and Abraham [2002]; Meissner and Wentz [2006]; Vergely *et al.* [2014]),
- the impact of the atmosphere (Liebe *et al.* [1992]; Skou and Hoffman-Bang [2005]; Wentz and Meissner [2016]),
- the effect of sea surface roughness on emissivity (Meissner *et al.* [2014]; Yueh *et al.* [1999]; Meissner and Wentz [2012]; Meissner *et al.* [2018]; Yin *et al.* [2016]; Yueh *et al.* [2010]; Yueh *et al.* [2014]). and,
- the effect of the portion of the energy received due to land or sea ice in the CIMR antenna pattern when the main lobe is over water, but, close to land-sea, or, sea ice-sea transition (e.g., see Reul *et al.* [2020], Meissner and Manaster [2021])

The upwelling brightness temperatures above the atmosphere but below the ionosphere (before Faraday rotation) is referred hereafter to as the “Top of Atmosphere” brightness temperature and denoted T_{tp}^{TOA} (with superscript “TOA”) for upwelling signal in polarization p . Considering all components of the scene brightness temperature, the complete model solution for T_{tp}^{TOA} , in the surface polarization basis, is:

$$\begin{pmatrix} T_{th}^{TOA} \\ T_{tv}^{TOA} \\ U^{TOA} \\ V^{TOA} \end{pmatrix} = \begin{pmatrix} T_{atm}^{up} + (\tau_d \tau_v \tau_w \tau_I \tau_R) [T_{surf,h}^{tot} + R_{surf,h}^{tot} \cdot T_{atm}^{dw} + T_{sch} + T_{ssh}] \\ T_{atm}^{up} + (\tau_d \tau_v \tau_w \tau_I \tau_R) [T_{surf,v}^{tot} + R_{surf,v}^{tot} \cdot T_{atm}^{dw} + T_{scv} + T_{ssv}] \\ (\tau_d \tau_v \tau_w \tau_I \tau_R) T_{erU} \\ (\tau_d \tau_v \tau_w \tau_I \tau_R) T_{erV} \end{pmatrix} \quad (\text{Eq.1})$$

where the only contribution to the third and fourth Stokes parameters at Top of the Atmosphere and in the surface polarization basis comes from the rough surface emission components, and in which:

Notation	Definition
T_{atm}^{up}	Unpolarized upwelling brightness temperature of atmospheric 1-way emission [K]
τ_d	1-way atmospheric transmittance associated with molecular oxygen absorption [nd]
τ_v	1-way atmospheric transmittance associated with water vapor absorption [nd]
τ_w	1-way atmospheric transmittance associated with cloud water absorption [nd]
τ_I	1-way atmospheric transmittance associated with ice water absorption [nd]
τ_R	1-way atmospheric transmittance associated with rain absorption [nd]
$T_{surf,p}^{tot}$	p-pol brightness temperature of the total sea surface emission (specular+rough+foam) [K]
$R_{surf,p}^{tot}$	reflectivity of the total sea surface (specular+rough+foam) in p-pol
T_{down}^{up}	Unpolarized downwelling brightness temperature of atmospheric 1-way emission [K]
T_{erU}	Third Stokes brightness temperature of rough surface emission (surface pol. Basis) [K]

T_{erv}	Fourth Stokes brightness temperature of rough surface emission (surfacepol. Basis) [K]
T_{scp}	p-pol brightness temperature of scattered celestial sky radiation (surface pol. Basis) [K]
T_{ssp}	p-pol brightness temperature of scattered solar radiation (sunglint) (surface pol.Basis) [K]

The brightness temperature of the total sea surface emission, $T_{surf,p}^{tot}$, can be further decomposed as follows:

$$T_{surf,p}^{tot} = T_s \cdot e_{surf,p}^{tot} = T_s \cdot [(1 - F_f) \cdot (e_{sp} + e_{rp}) + F_f \cdot e_{foam,p}] = T_s \cdot (e_{sp} + \Delta e_{rp}) \quad (\text{Eq.2})$$

where:

Notation	Definition
T_s	Sea Surface Temperature [K]
$e_{surf,p}^{tot}$	p (h or v)-pol total sea surface emission (specular+rough+foam)
F_f	Fractional area of sea surface covered by foam
e_{sp}	p-pol specular emission (surface pol. Basis)
Δe_{rp}	p-pol rough surface emission (surface pol. Basis)
$e_{foam,p}$	p-pol foam-covered surface emission (surface pol. Basis)

and where we split the total sea surface brightness temperature $T_{surf,p}^{tot}$ into two components:

- the brightness temperature from the perfectly flat sea surface ($T_{sp} = T_s \cdot e_{sp}$),
- the brightness temperature contrast induced by the rough and foamy sea surface ($T_{rp} = T_s \cdot \Delta e_{rp}$)

Note that the total surface reflectivity is related to the total surface emissivity by $R_{surf,p}^{tot} = 1 - T_{surf,p}^{tot}$. Considering all components of the scene brightness temperature, the complete model solution for the upwelling brightness temperatures above the atmosphere but below the ionosphere (before Faraday rotation) in the surface polarization basis, is, therefore in p-polarization:

$$T_{tp}^{TOA} = T_{atm}^{up} + (\tau_d \tau_v \tau_w \tau_I \tau_R) [T_s \cdot [e_{sp} + \Delta e_{rp}] + R_{surf,p}^{tot} \cdot T_{atm}^{dw} + T_{scp} + T_{ssp}] \quad (\text{Eq.3})$$

8.2 Level-2 end to end algorithm functional flow diagram

8.2.1 Input data

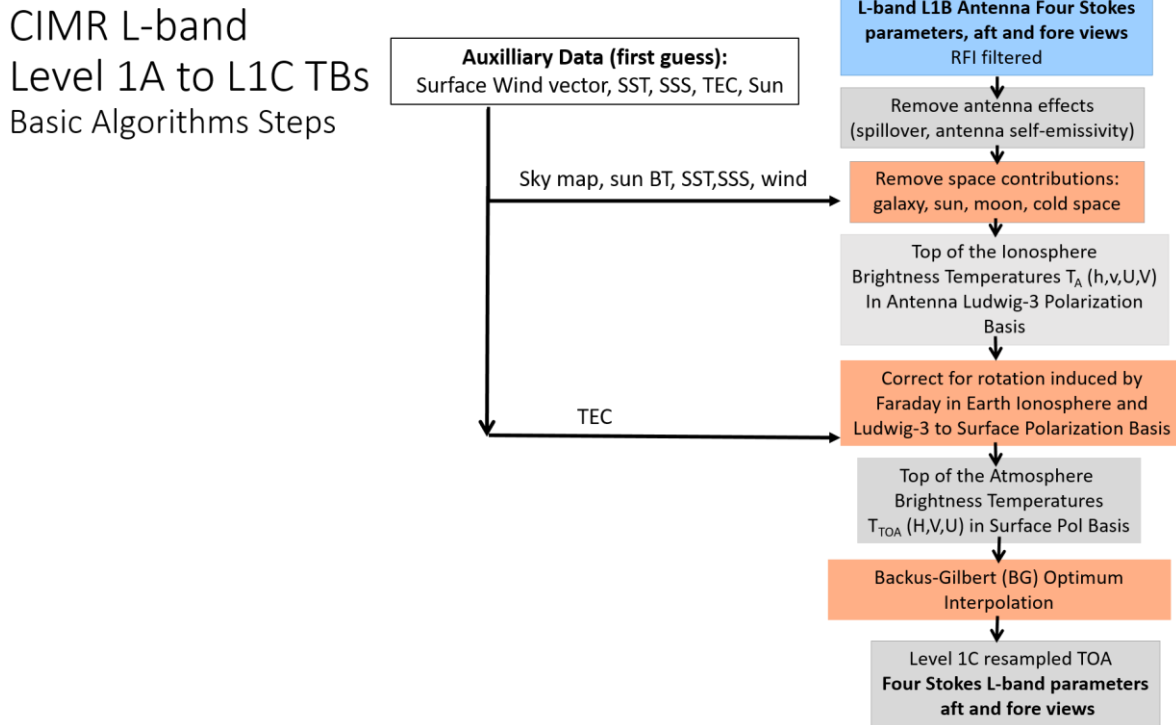


Figure 3: Level-1B to Level-1C L-band algorithm functional flow diagram.

The inputs to the L2B SSS algorithm are the Level 1C TB at L-band in H-, V-, 3rd, and, 4th Stokes for the fore and aft views. As summarized in Fig. 4, we assume here that the TBs data are corrected for antenna spill-over and emissivity, sky and sun direct and earth reflected/scattered radiation, Faraday rotation across the ionosphere, and that they are provided with a proper rotation of the Stokes parameter from the antenna polarization basis to the surface polarization basis (L1B processor). In fine, we will use as input the Leve1b data after proper resampling (so-called Level1c).

It is understood that the corrections for (1) the sky and sun direct and earth reflected/scattered radiation, (2) the model for the rotation of the Stokes parameter due to Faraday rotation across the ionosphere and polarisation basis changes, as well as (3) the L1B resampling approach all shall be applied through the Level 1 algorithms and not in the present L2B SSS algorithm. Nevertheless, we will present hereafter how these contributions can be potentially modelled.

In addition, it is not clear at which level (1) or (2) the land- and ice-ocean transitions effects shall be corrected for on the Tbs (so called land sea contamination). Given that these effects require antenna-pattern -related information, it shall better be applied in the Level 1 algorithms. We shall propose in version 2 of this ATBD some post-launch approaches to derive such corrections.

Another input data are the CIMR L2B SST and Wind products, properly resampled on the L-band acquisitions.

8.2.1 SSS retrieval algorithm

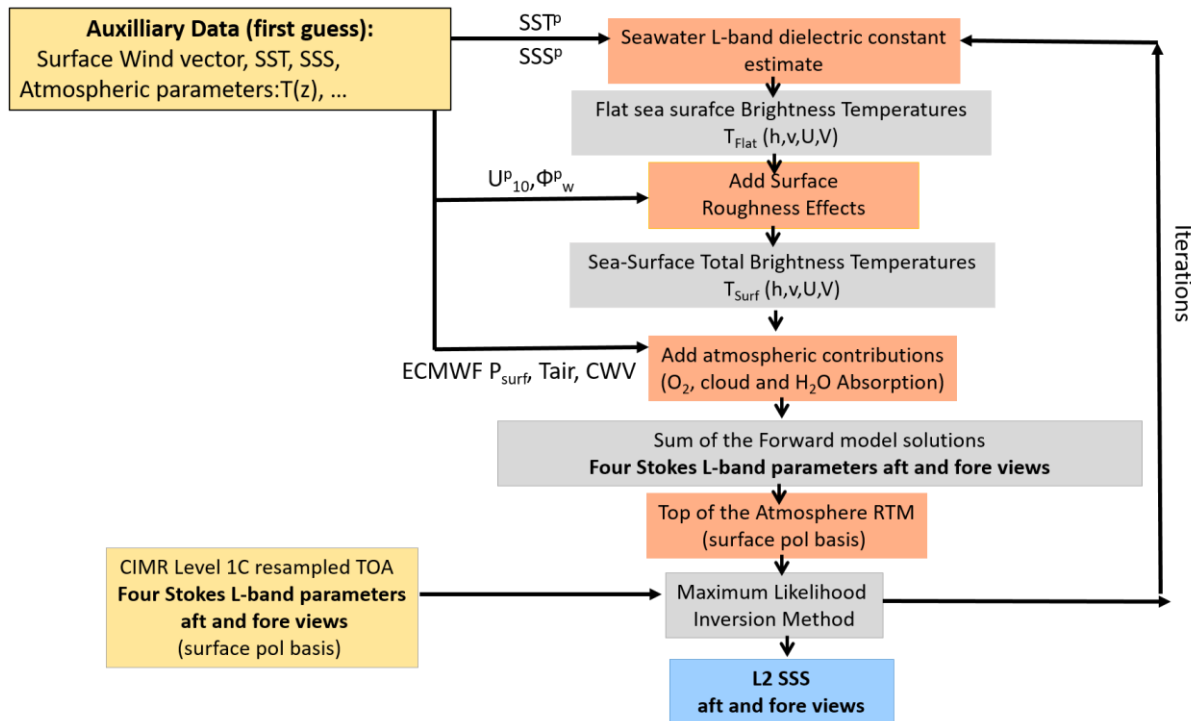


Figure 4: Level-2 SSS end to end algorithm functional flow diagram. Here, SST^p , SSS^p , and U_{10}^p, Φ_w^p are a priori values for the SST, SSS, 10 meter height surface wind speed and direction, respectively.

The principle of the proposed SSS retrieval algorithms rely on a forward radiative transfer modelling of the top of the atmosphere brightness TtpTOA from first guess geophysical values (SSS, SST, U10, etc...), and, the retrieval of the geophysical parameters (SSS, SWS, ..) from a minimization of the differences between the observed and modelled TtpTOA. The Level-2 end to end algorithm functional flow diagram is shown in Fig. 5. The radiative transfer forward model which is needed is based on the following components:

- a sea-water dielectric constant model at 1.4 GHz,
- a perfectly flat, or specular, sea surface emission model,
- a surface roughness and foam-induced correction model,
- a Radiative Transfer Model for Atmospheric corrections,
- a scattering model to correct for sea surface scattered Solar and celestial radiation, and,
- a correction for geometric rotation from surface polarization basis to antenna polarization basis,
- and, to model the TB at antenna level, a model to correct for Faraday rotation in the ionosphere.

We review these forward model components and corrections in the following subsections.

8.3 Models for the Dielectric Constant of seawater at 1.4 GHz

8.3.1 Mathematical description

The Zhou et al. [2021]’s Debye model for the seawater dielectric constant is used in the present algorithm for the L-band channels (1.4 GHz), will be referred to as “GW2020”, and can be expressed by:

$$\varepsilon_{sw}(f, S, T) = \varepsilon_{\infty} + \frac{(\varepsilon_{s-dw}(T)R_{sw-dw}(S,T) - \varepsilon_{\infty})}{1+i\omega\tau(T)} - i \frac{\sigma(f,S,T)}{\omega\varepsilon_0} \quad (\text{Eq.4})$$

where f is the electromagnetic frequency ([Hz]), T and S are the temperature ([degree celsius]) and salinity ([psu]) of seawater, respectively; ε_0 is the dielectric constant of free space; $\varepsilon_{s-dw}(T)$ is the static dielectric constant of distilled water, given by:

$$\varepsilon_{s-dw}(T) = 88.0516 - 4.01796 \times 10^{-1} \cdot T - 5.1027 \times 10^{-5} \cdot T^2 + 2.55892 \times 10^{-5} \quad (\text{Eq.5})$$

and $\tau(T)$ is the relaxation time of distilled water:

$$\tau(T) = 1.75030 \times 10^{-11} - 6.12993 \times 10^{-13} \cdot T + 1.24504 \times 10^{-14} \cdot T^2 - 1.14927 \times 10^{-16} \cdot T^3 \quad (\text{Eq.6})$$

$R_{sw-dw}(S, T)$ is an additional factor in the static dielectric constant of seawater due to the presence of ions, given by:

$$R_{sw-dw}(S, T) = 1 - S \cdot (3.97185 \times 10^{-3} - 2.49205 \times 10^{-5} \cdot T - 4.27558 \times 10^{-5} \cdot S + 3.929825 \times 10^{-7} \cdot S \cdot T + 4.15350 \times 10^{-7} \cdot S^2) \quad (\text{Eq.7})$$

Note that $\sigma(f, S, T)$ needs to be nulled at $S = 0$ since the conductivity of distilled water is close to 0. The expression of $\sigma(f, S, T)$ given in Zhou *et al.* [2021] is:

$$\sigma(f, S, T) = \sigma(f, S, 0) \cdot R_{\sigma}(f, S, T) \quad (\text{Eq.8})$$

where for $f=1.4$ GHz,

$$\sigma(f, S, 0) = 9.50470 \times 10^{-2} \cdot S - 4.30858 \times 10^{-4} \cdot S^2 + 2.16182 \times 10^{-6} \cdot S^3 \quad (\text{Eq.9})$$

and

$$R_{\sigma}(f, S, T) = 1 + T \cdot (3.76017 \times 10^{-2} + 6.32830 \times 10^{-5} \cdot T + 4.83420 \times 10^{-7} \cdot T^2 - 3.97484 \times 10^{-4} \cdot S + 6.26522 \times 10^{-6} \cdot S^2) \quad (\text{Eq.10})$$

8.3.2 Functional flow diagram

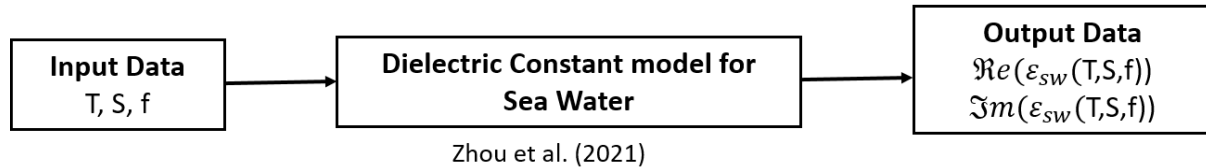


Figure 5: Dielectric Constant model Flow Diagram. Input data are Temperature T [$^{\circ}$ C], salinity S [psu], and, radiometer electromagnetic frequency f [Hz]. Output are the real and imaginary parts of $\epsilon_{sw}(f, S, T)$

8.3.3 Assumption and limitations

The search for a model for the dielectric constant of sea water at 1.4 GHz accurate enough to promote improvements in the retrieval of is not yet complete. There are at least two challenges. One is that making measurements that are consistent with an accuracy of the salinity product of better than 0.2 psu is very hard. At CIMR OZA of 53° and for an SST of 25°C, an accuracy of 0.2 psu corresponds to radiometric accuracy of ~0.16 K for a measurement at 1.4 GHz (see Fig. 8). Assuming equal error, Δ , in the real and imaginary parts of the dielectric constant, an accuracy of about $\Delta=0.25\%$ in the measurement of the dielectric constant is required (at 35 psu and 25°C) to have an error of less than 0.1 K in T_B . The current measurement accuracy of the GW2020 measurements at this temperature and salinity is about 0.35% (Lang *et al.* [2016]). So, there is yet a need for improvement, and if the goal is eventually to achieve 0.1 psu, even more progress is needed.

In the meantime, a problem with many available dielectric constant models is the use of the models outside of their range of validity. There are no physical restrictions, which prevent using any of these models at any frequency, salinity, or temperature, but all the models discussed here are based on measurements of a finite range in S and T and use mathematical functions (usually polynomials) to fit the unknown parameters to the data in this range. The fits are unconstrained outside of the range of the data. This is evident in the case of the KS model. As found by Le Vine *et al.* [2022], the real part of some models diverges strongly from the measurements for high ($T > 30^{\circ}$ C) and low temperatures ($T < 5^{\circ}$ C).

8.4 Perfectly flat or ‘specular’ sea surface emission



Figure 6: Front view of the PALS radiometer instrument measuring the brightness temperature emitted by a perfectly flat surface of a saltwater pond. L-band radiometric measurements were made over a salinity range between 25 and 40 pss and a temperature range of 8.5°C to 32°C (from Wilson et al. [2004]).

8.4.1 Mathematical Description

The dependence of the microwave brightness temperature emitted by the sea surface T_B on SSS and SST is contained in the emissivity, e : $T_B = T \times e$, where T is the sea surface temperature. The emissivity e is a quantity that depends on physical and chemical properties of the water (e.g. salinity and temperature), observational conditions (incidence angle, electromagnetic frequency, polarization), as well as on the sea surface roughness.

For a perfectly flat ocean surface the scattered electric and magnetic fields may be expressed in terms of the incident fields. The reflected electric field components (E'_h, E'_v) are related to the incident components (E_h, E_v) by the diagonal matrix equation:

$$\begin{pmatrix} E'_h(\theta_s, \phi_s) \\ E'_v(\theta_s, \phi_s) \end{pmatrix} = \begin{pmatrix} R_{hh}^{(0)} & 0 \\ 0 & R_{vv}^{(0)} \end{pmatrix} \begin{pmatrix} E_h(\theta_s, \phi_s - 180^\circ) \\ E_v(\theta_s, \phi_s - 180^\circ) \end{pmatrix} \quad (\text{Eq.11})$$

where (θ_s, ϕ_s) is the specular reflection direction for radiation incident from direction $(\theta_s, \phi_s - 180^\circ)$. The superscripts on the reflection coefficients indicate that they correspond to zero order expansion in surface slope, i.e., the flat surface reflection. The flat surface reflection coefficients on the preceding matrix are given by the Fresnel equations:

$$R_{hh}^{(0)}(S, T_s, \theta_s) = \frac{\cos \theta_s - \sqrt{\epsilon_{sw}(S, T_s) - \sin^2 \theta_s}}{\cos \theta_s + \sqrt{\epsilon_{sw}(S, T_s) - \sin^2 \theta_s}} \quad (\text{Eq.12})$$

$$R_{vv}^{(0)}(S, T_s, \theta_s) = \frac{\epsilon_{sw}(S, T_s) \cos \theta_s - \sqrt{\epsilon_{sw}(S, T_s) - \sin^2 \theta_s}}{\epsilon_{sw}(S, T_s) \cos \theta_s + \sqrt{\epsilon_{sw}(S, T_s) - \sin^2 \theta_s}} \quad (\text{Eq.13})$$

Where $\epsilon_{sw}(S, T_s)$ is the dielectric constant for seawater which is a function of the surface salinity S in practical salinity units (pss) and the temperature T_s in kelvin. The Fresnel reflection matrix equation is:

$$T' = \begin{pmatrix} T'_h \\ T'_v \\ U' \\ V' \end{pmatrix} = M^{(0)}T = \begin{pmatrix} \left| R_{hh}^{(0)} \right|^2 \delta^2 & 0 & 0 & 0 \\ 0 & \left| R_{vv}^{(0)} \right|^2 \delta^2 & 0 & 0 \\ 0 & 0 & \Re \left\{ R_{hh}^{(0)} \left(R_{vv}^{(0)} \right)^* \right\} & \Im \left\{ R_{hh}^{(0)} \left(R_{vv}^{(0)} \right)^* \right\} \\ 0 & 0 & -\Im \left\{ R_{hh}^{(0)} \left(R_{vv}^{(0)} \right)^* \right\} & \Re \left\{ R_{hh}^{(0)} \left(R_{vv}^{(0)} \right)^* \right\} \end{pmatrix} \begin{pmatrix} T_h \\ T_v \\ U \\ V \end{pmatrix} \quad (\text{Eq.14})$$

where δ is the Kroneker delta, \Re and \Im are the real and imaginary part, respectively. For a perfectly flat ocean surface with salinity, S , temperature, T_s , and observed at incidence angle θ_s , the emissivity at polarization, p (horizontal or vertical), and electromagnetic frequency, f , (note that we quote the center of a microwave frequency bandwidth associated with a given radiometer) is given by Peake [1959]:

$$e_{sp}^{(0)}(f, S, T_s, \theta_s) = 1 - \left| R_{pp}^{(0)}(\epsilon_{sw}, \theta_s) \right|^2 \quad (\text{Eq.15})$$

Where $R_{pp}^{(0)}$ is the Fresnel reflection coefficient given above in Eq.12 and Eq.13. The specular brightness temperature emitted by the sea surface in horizontal polarization is then

$$T_{esh}(S, T_s, \theta_s) = T_{esh}(\epsilon_{sw}(S, T_s), T_s, \theta_s) = T_s \cdot e_{sh,f}^{(0)}(S, T_s, \theta_s) = T_s \cdot \left[1 - \left| R_{hh}^{(0)}(\epsilon_{sw}, \theta_s) \right|^2 \right] \quad (\text{Eq.16})$$

and in vertical polarization:

$$T_{esv}(S, T_s, \theta_s) = T_{esv}(\epsilon_{sw}(S, T_s), T_s, \theta_s) = T_s \cdot e_{sv,f}^{(0)}(S, T_s, \theta_s) = T_s \cdot \left[1 - \left| R_{vv}^{(0)}(\epsilon_{sw}, \theta_s) \right|^2 \right] \quad (\text{Eq.17})$$

where $e_{sp,f}^{(0)}$ is the specular emissivity at polarization p and frequency f .

As shown in Figure 1, the specular brightness temperature sensitivity to SSS $\partial T_{esp}/\partial SSS$ increases with decreasing electromagnetic frequency, peaking at ~ 1 GHz (L-band) and with increasing incidence angle. As the frequency band 1.400 to 1.427 GHz is protected for radio-astronomy observation, it has been used for SSS remote sensing. Given a model for $\epsilon_{sw}(f, S, T)$, in its simplest form, SSS remote sensing, therefore, consists of measuring/estimating the L-band T_{esp} emitted by the perfectly flat ocean surface together with an auxilliary SST. The intersection of the two values on a graph such as shown in Figure 7 can then be used to retrieve SSS.

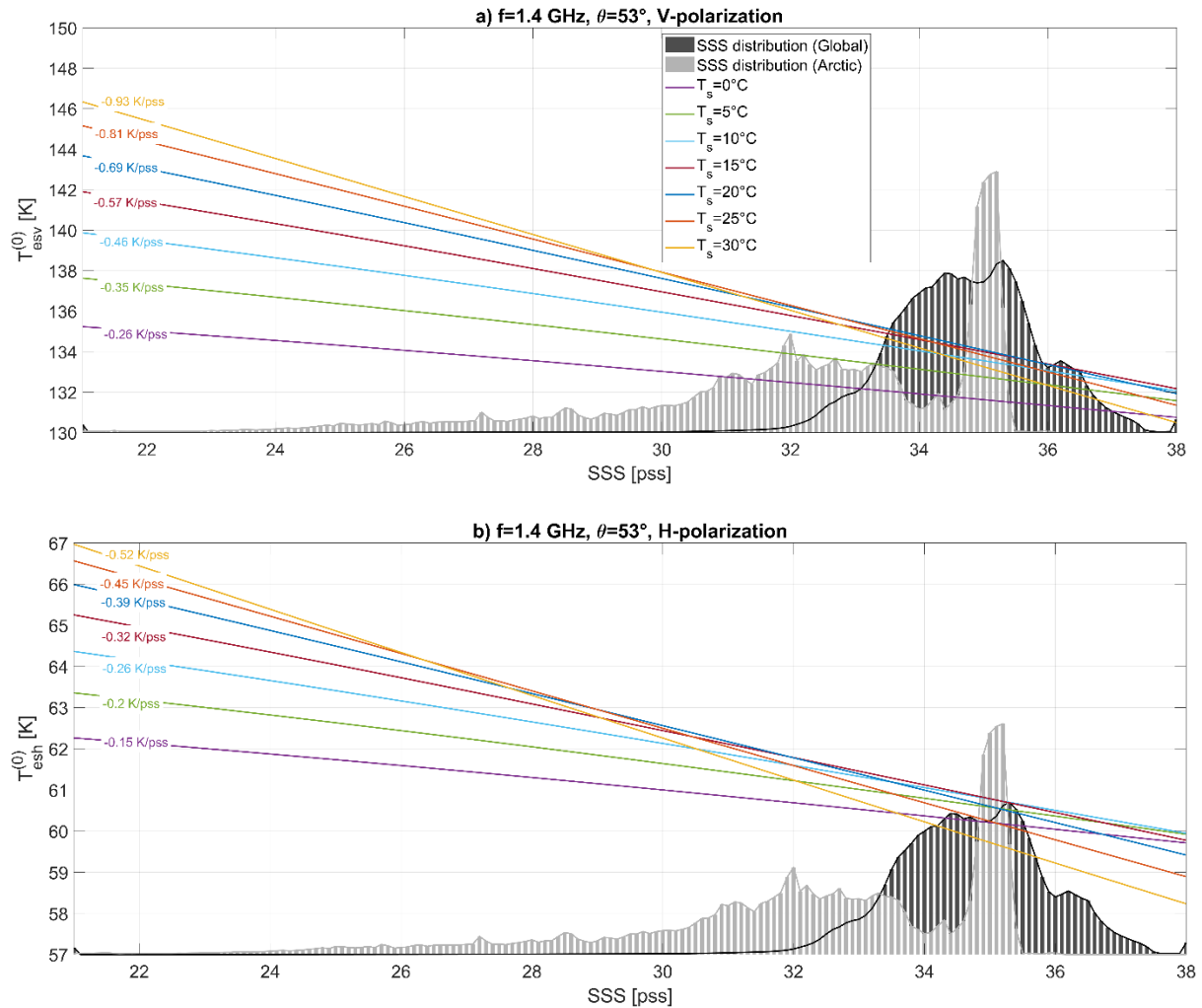


Figure 7: Specular sea surface brightness temperatures at 1.4 GHz, at V- (a) and H- (b) polarization, for the CIMR nominal OZA of 53° and as a function of sea surface salinity (x-axis) for different representative sea surface temperature values (colors). The black and gray histograms represent the normalized distribution of historical in situ SSS observation at global scale and in the Arctic, respectively.

We used the laboratory-measurement based GSW2020's model for the sea water dielectric constant at L-band to simulate the changes in the specular sea surface brightness temperatures at 1.4 GHz, at V- and H-polarization and for the CIMR nominal incidence angle of 53° . The results are shown as a function of sea surface salinity for different representative sea surface temperature values in Figure 7.

As found, the sensitivity of T_{esp} to SSS is quasi-linear for a given SST. $|\partial T_{esp}/\partial SSS|$ is greater in V-polarization than in H-polarization and increases with increasing SST. The sensitivity of V-pol T_{esv} to SSS is dropping from -0.93K/pss at $T_s=30^\circ\text{C}$ to -0.26K/pss at $=0^\circ\text{C}$. With an expected CIMR L-band radiometer NEDT~0.3 K, one can therefore expect instrumental noise errors in instantaneous single polarization recordings of~0.3 pss in the tropics ($T_s=30^\circ\text{C}$), and ~1 pss in cold seas ($T_s=5^\circ\text{C}$).

8.4.2 Functional flow diagram



Figure 8: Specular Sea Surface Emission model Flow Diagram. Input data are the real and imaginary parts of the sea water dielectric constant $\epsilon_{sw}(f, S, T)$, the radiometer incidence angle θ_s and the sea surface temperature T . Output data are the specular brightness temperature $T_{esv}(S, T_s, \theta_s)$ and $T_{esh}(S, T_s, \theta_s)$ in vertical and horizontal polarisation, respectively.

8.5 Rough Sea surface emission

8.5.1 Physics of the problem

At a given microwave frequency f , the total surface emissivity at polarization p , $E_{p,f}$ can be modeled as the sum of the perfectly flat ('specular') sea surface emission and a roughness-induced radio-brightness contrast;

$$E_{p,f}^{surf} = e_{sp}^{(0)}(\theta_s, S, T_s, f) + \Delta e_{rp}^{rough}(\theta_s, S, T_s, f, U_{10}, \phi_r, \phi_w) \quad (\text{Eq.18})$$

where the emission change caused by ocean surface roughness Δe_{rp}^{rough} is a function of the radiometer frequency f , incidence angle θ_s and azimuth ϕ_r , the surface temperature T_s , salinity S , 10- meter height wind speed U_{10} , and the wind direction ϕ_w . Here the linearly polarized electric field components normal to the propagation direction, E_h and E_v , are defined with respect to polarization basis vectors at the target given by $\hat{\mathbf{h}}$ and $\hat{\mathbf{v}}$. These basis vectors, in turn, are defined such that the surface emission propagation direction unit vector $\hat{\mathbf{k}} = \hat{\mathbf{v}} \times \hat{\mathbf{h}}$. Under this *forward scattering alignment* (FSA) polarization basis convention, the relative azimuth angle ϕ_s that appears in the rough surface emission contribution is defined as $\phi_s = \phi_r - \phi_w$, which is the difference between the radiometer azimuth ϕ_r (measured counterclockwise from due east and from the perspective of an observer looking towards the radiometer from the target) and the downwind direction (towards which the wind is blowing, positive counterclockwise from due east). In the literature, azimuthal harmonics are typically presented as a function of $\phi_w - \widetilde{\phi}_r$ where $\widetilde{\phi}_r = \phi_r + 180^\circ$ is not clearly stated.

Wind-induced surface waves are the primary contributor to ocean surface roughness, with internal waves, wind-current interactions, and ship wakes to be important but

secondary contributors (Gasiewski and Kunkee [[1994](#)]). Wind-induced waves can be divided into two primary scales (Yueh [[1997](#)]):

1. The **large-scale waves** cause the local surface incidence angle to differ from the effective earth incidence angle, and mix vertical and horizontal polarizations (Gasiewski and Kunkee [[1994](#)]), and,
2. The **small-scale gravity-capillary** waves riding on top the large-scale gravity waves (Johnson and Zhang [[1999](#)]): the small-scale waves modify the specular surface reflection (or emission) through the bistatic scattering of the radiation incident upon the ocean surface.

In addition, although **foam generated by breaking waves and wind streaks** typically covers only a few percent of the sea surface, it has a profound effect on the average microwave brightness of the ocean surface (Droppleman [[1970](#)]). For surface wind speeds greater than 15 m/s, foam-induced effects may provide as much as half of the total sea surface signature to an orbiting microwave radiometer (Barber Jr. and Wu [[1997](#)]), due to its near-blackbody behavior. As wind speed increases, ocean foam coverage also increases, resulting in a large discrepancy between forward model (e.g., two-scale) emissivity calculations made with and without consideration of foam coverage. The quasi-blackbody models used for both foam emissivity and coverage are in themselves of limited accuracy due to the paucity of in situ observations for both foam coverage and emissivity that have been able to be made in conjunction with brightness temperatures from passive microwave instruments.

Different mechanisms responsible for the rough sea surface emissivity in the microwave domain exhibit several anisotropic features, which, in turn, lead to a **wind directional dependence** of the observed brightness temperatures. The probability density function of the sea surface slope is skewed in the along wind axis and has a larger along wind variance than crosswind variance (Cox and Munk [[1954](#)]). Furthermore, the RMS height of the small gravity-capillary waves, which are riding on top of the large gravity waves, exhibits a noticeable anisotropy. The gravity- capillary waves traveling in the along-wind direction have larger amplitudes than those traveling in the crosswind direction (Mitsuyasu and Honda [[1982](#)]). Both effects cause an up-crosswind asymmetry of the emitted radiation. In addition, up-downwind asymmetries occur. The gravity- capillary waves and sea foam are not uniformly distributed over the underlying structure of large-scale waves. Aircraft radiometer measurements (Smith *et al.* [[2008](#)]) show that the forward plunging side of a breaking wave is emitting warmer microwave emissions than its backside.

Furthermore, the small-scale gravity-capillary waves have the tendency to cluster on the downwind side of the large-scale gravity waves (Cox [[1958](#)]; Keller and Wright [[1975](#)]). Finally, several studies of nonlinear wave-wave interaction suggest that the small-scale ocean surface waves are not propagating in the wind direction (Banner

[1990]; Hwang *et al.* [2000]; Irisov [2000]). This might be an additional source of error in the wind direction retrieval from radiometer data.

It has been empirically observed that the first and second Stokes parameters of the roughness correction are even functions of the relative azimuth angle $\phi_s = \phi_r - \phi_w$ in the FSA convention, while the third and fourth Stokes parameters are odd functions of this angle. Typically, the total surface induced brightness temperature is therefore decomposed into azimuthal harmonics of the relative wind direction ϕ_s , as follows:

$$\begin{pmatrix} E_{h,f}^{surf} \\ E_{v,f}^{surf} \\ E_{U,f}^{surf} \\ E_{V,f}^{surf} \end{pmatrix} = \begin{pmatrix} e_{sh,f}^{(0)} + \Delta e_{h,f}^{(0)} + \Delta e_{h,f}^{(1)} \cos \phi_s + \Delta e_{h,f}^{(2)} \cos 2\phi_s \\ e_{sv,f}^{(0)} + \Delta e_{v,f}^{(0)} + \Delta e_{v,f}^{(1)} \cos \phi_s + \Delta e_{v,f}^{(2)} \cos 2\phi_s \\ \Delta U_f^{(1)} \sin \phi_s + \Delta U_f^{(2)} \sin 2\phi_s \\ \Delta V_f^{(1)} \cos \phi_s + \Delta V_f^{(2)} \sin 2\phi_s \end{pmatrix} \quad (\text{Eq.19})$$

For natural wind-driven ocean surfaces, the zeroth-harmonic components exist only for vertical ($e_{sv,f}^{(0)} + \Delta e_{v,f}^{(0)}$) and horizontal ($e_{sh,f}^{(0)} + \Delta e_{h,f}^{(0)}$) polarizations. Upwind and downwind asymmetry features are accounted for in the first-harmonic component ($\Delta e_{h,f}^{(1)}$, $\Delta e_{v,f}^{(1)}$, $\Delta U_f^{(1)}$, and $\Delta V_f^{(1)}$), and the second-harmonic component ($\Delta e_{h,f}^{(2)}$, $\Delta e_{v,f}^{(2)}$, $\Delta U_f^{(2)}$, and $\Delta V_f^{(2)}$), account for the upwind-crosswind anisotropy. Such symmetry is expected for reflection-symmetric ocean surfaces although it is not physically guaranteed for all ocean surfaces. Nonetheless, this nominal symmetry allows expansion of the four Stokes components in either cosine or sine Fourier series in the azimuth angle. Truncating these series at the second-azimuthal-harmonic captures virtually all of the currently observable azimuthal brightness behavior. In the present algorithm, we rely on well-established empirical Geophysical Model Functions (GMF) for the harmonics coefficients at L-band and associated polarization and incidence angles.

8.5.2 Wind-induced isotropic emissivity

The Aquarius V5's GMF (Meissner *et al.* [2018]) are used here for modelling the L-band $\Delta e_{p,f}^{(0)}(\theta_s, U_{10}, T_s, S)$. Note that the Aquarius L-band GMFs are provided at $\theta_{ref}=29.36^\circ$, 38.44° , and 46.29° . As discussed in Meissner and Wentz [2012], the wind induced emissivity $\Delta e_{p,f}^{(0)}(\theta_s, U_{10}, T_s, S)$ has a small residual SST dependence and the GMFs are also provided for a reference SST of $T_{ref}=20^\circ\text{C}$. The wind induced emissivity is however slightly larger in cold water than in warm water, and to correct for this effect, Meissner and Wentz [2012] used the following model:

$$\Delta e_{p,f}^{(0)}(\theta_{ref}, U_{10}, T_s, S) = \delta_{ref}^{p,f}(U_{10}) \cdot \frac{e_{sp,f}^{(0)}(\theta_{ref}, T_s, S)}{e_{sp,f}^{(0)}(\theta_{ref}, T_{ref}, S)} \quad (\text{Eq.20})$$

where the second multiplicative term is the ratio of the specular sea emission at $\text{SST}=T_s$ to the specular sea emission at $\text{SST}=T_{ref} = 20^\circ\text{C}$ (Eq.16 and 17), and $\delta_{ref}^{p,f}(U_{10}, \theta_s)$ is the wind-speed induced isotropic emissivity for 10-meter height surface wind speed (U_{10}), polarization p , frequency f , at reference EIA θ_{ref} , and at the reference $\text{SST}=20^\circ\text{C}$, and, is fitted by the fifth-order polynomial:

$$\delta_{ref}^{p,f}(U_{10}) = \sum_{k=1}^5 \delta_k^{p,f} \cdot U_{10}^k \quad (\text{Eq.21})$$

where the $\delta_k^{p,f}$ coefficients are given in [Table 2](#) for f=1.4 GHz, both linear polarization and for $\theta_{ref} = 52^\circ$. Note that we linearly-extrapolated the Aquarius L-band GMFs provided at $\theta_s=29.36^\circ$, 38.44° , and 46.29° to derive the L-band coefficients $\delta_k^{p,f}$ at $\theta_{ref} = 52^\circ$.

f [GHz]	p	1	2	3	4	5
1.4	v	1.6097e-3	-2.6751e-4	2.4483e-5	-8.6502e-7	1.0749e-8
1.4	h	4.3588e-3	-5.8672e-4	4.3997e-5	-1.4223e-6	1.6548e-8

Table 2: $\delta_k^{p,f}$ coefficients of Eq.40 for each CIMR frequency and dual polarization for $\theta_{ref} = 55^\circ$ (C- to Ka bands) and $\theta_{ref} = 52^\circ$ (L-band).

Note that at L-band, the OZA is centered on 52° . To account for small θ_s variation from θ_{ref} , one can proceed as follows. At nadir, both $\Delta e_{h,f}^{(0)}(\theta_s = 0)$ and $\Delta e_{v,f}^{(0)}(\theta_s = 0)$ have the same value $\Delta e_f^{(\text{nad},0)}$. The results from Hollinger [[1971](#)] and Sasaki *et al.* [[1987](#)] suggest that $\Delta e_f^{(\text{nad},0)}$ is approximately given by the arithmetic average of the v-pol and h-pol values at around $\theta_{ref}=55^\circ$:

$$\Delta e_f^{(\text{nad},0)}(U_{10}, T_s, S, \theta_s = 0^\circ) \cong \frac{1}{2} [\Delta e_{v,f}^{(0)}(\theta_{ref}, U_{10}, T_s, S) + \Delta e_{h,f}^{(0)}(\theta_{ref}, U_{10}, T_s, S)] \quad (\text{Eq.22})$$

The EIA dependence of $\Delta e_f^{(0)}$ can then be parameterized by a low/high order polynomial in for h-pol/v-pol, as follows:

$$\Delta e_{p,f}^{(0)}(\theta_s, U_{10}, T_s, S) = \Delta e_f^{(\text{nad},0)}(U_{10}, T_s, S) + [\Delta e_{p,f}^{(0)}(\theta_{ref}, U_{10}, T_s, S) - \Delta e_f^{(\text{nad},0)}(U_{10}, T_s, S)] \cdot \left(\frac{\theta_s}{\theta_{ref}}\right)^{x_p} \quad (\text{Eq.23})$$

The form (Eq.23) applies for $\theta_s \leq \theta_{ref}$. Following Meissner and Wentz [[2012](#)], we shall linearly extrapolate the θ_s -dependence for $\theta_s > \theta_{ref}$, which is what we did for the CIMR L-band GMFs.

As illustrated in Figure 9, the proposed GMFs reveal a systematically higher impact of the wind-induced roughness on the isotropic radio-brightness contrast at H-pol than V-pol. In H-pol, the impact of wind-induced roughness on the isotropic emissivity $\Delta e_{h,f}^{(0)}$ is increasing with increasing radiometer incidence angle. Contrarily, at V-pol, the L-band $\Delta e_{v,f}^{(0)}$ is smaller at CIMR nominal OZA than at lower incidences. This behavior is consistent with in situ and aircraft measurements at such angle and frequencies (Hollinger [[1970](#)], Hollinger [[1971](#)], Camps *et al.* [[2004](#)], Martin *et al.* [[2014](#)]), as well as, with the prediction of two-scale emissivity models (Dinnat *et al.* [[2002](#)], Yin *et al.* [[2016](#)], Kilic *et al.* [[2019](#)], Ma *et al.* [[2021](#)]). The processes involve resonance in the scattering functions, occurring at wavelengths larger than $3\lambda_0$ (where λ_0 is the electromagnetic wavelength) for high incidence angles (Johnson and Zhang [[1999](#)]).

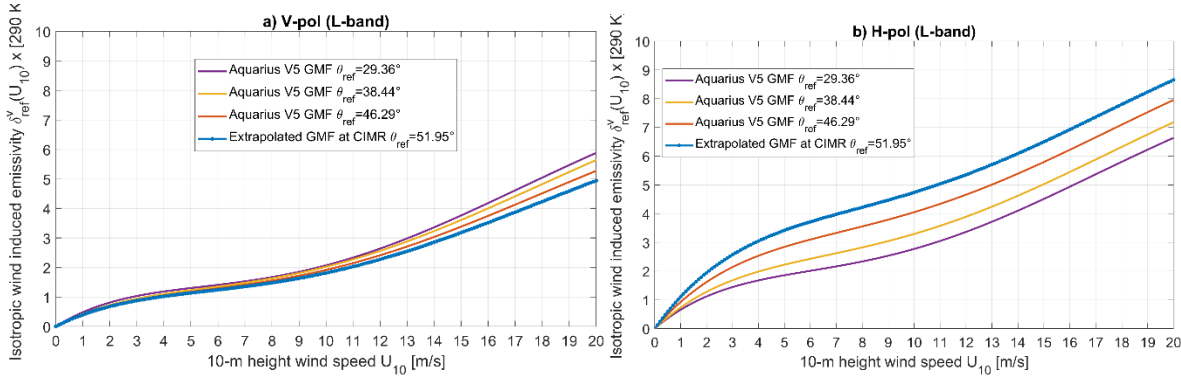


Figure 9: Isotropic wind induced emissivity at L-band for (a) V-polarization and (b) H-polarization. The GMF are for the CIMR L-band horn nominal incidence angle of $\theta_{\text{ref}} = 51.95^\circ$ and SST=290 K. Aquarius GMFs at $\theta_s = 29.36^\circ$, 38.44° , and 46.29° are also indicated.

8.5.3 Wind-induced anisotropic emissivity

We now turn to the model function $\Delta e_p^{(i=1,2)}$ for the four Stokes parameters of the wind direction signal for L-bands entering in Eq.19. The GMFs for the anisotropic components are described in Meissner *et al.* [2018] at $\theta_{\text{ref}} = 29.36^\circ$, 38.44° , and 46.29° for the L-band. They are given by:

$$\Delta e_p^{(i=1,2)}(\theta_{\text{ref}}, U_{10}) = \sum_{k=1}^5 \alpha_{i,k}^p \cdot U_{10}^k \quad (\text{Eq.24})$$

the $\alpha_{i,k}^p$ coefficients are given in Table 3 for $i=1$ and Table 4, for $i=2$. Here again, we linearly extrapolated the lower incidence Aquarius L-band GMFs functions to estimate the $\alpha_{i,k}^{p,f}$ coefficients at 1.4 GHz and $\theta_{\text{ref}} = 52^\circ$.

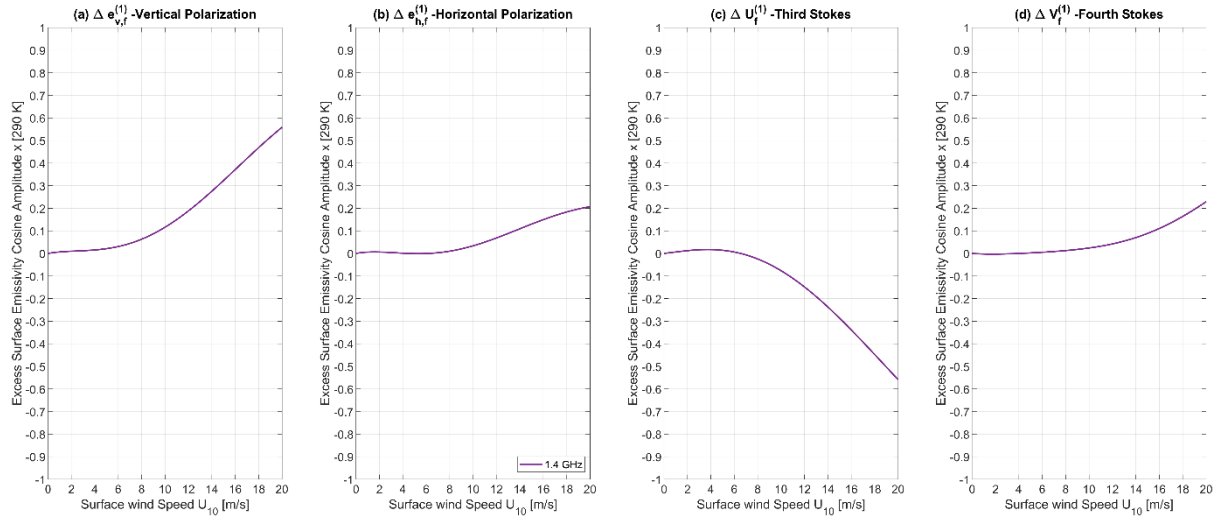


Figure 10: GMF of the first azimuthal harmonic coefficients $\Delta e_{p,f}^{(1)}(\theta_{\text{ref}}, U_{10})$ as a function of surface wind speed at L-band for (a) V-polarization, (b) H-polarization, (c) Third Stokes parameter and (d) fourth Stokes parameter. The GMF are for the L-band reference incidence angle of $\theta_{\text{ref}} = 52^\circ$ and SST=290K.

As shown in Figure 10, the amplitude of the first harmonic coefficients ($\Delta e_{v,f}^{(1)}$, $\Delta e_{h,f}^{(1)}$, $\Delta U_f^{(1)}$, $\Delta V_f^{(1)}$), characterizing the upwind-downwind asymmetry of the excess surface emissivity, is small for low winds and it increases (in an absolute manner) with increasing wind speed. The relative polarization behavior is consistent between

frequency observations at L-band (Yueh *et al.* [1999], Piepmeier and Gasiewski [2001], Yueh *et al.* [2006]): there is larger first harmonic amplitude for vertical polarization than for horizontal polarization, particularly at high winds > 10 m/s. The first harmonic amplitude is also in general significantly higher than the second harmonic amplitude ($\Delta e_{v,f}^{(2)}$, $\Delta e_{h,f}^{(2)}$, $\Delta U_f^{(2)}$, $\Delta V_f^{(2)}$), which represents the upwind–crosswind asymmetry of the excess surface emissivity (see Figure 11).

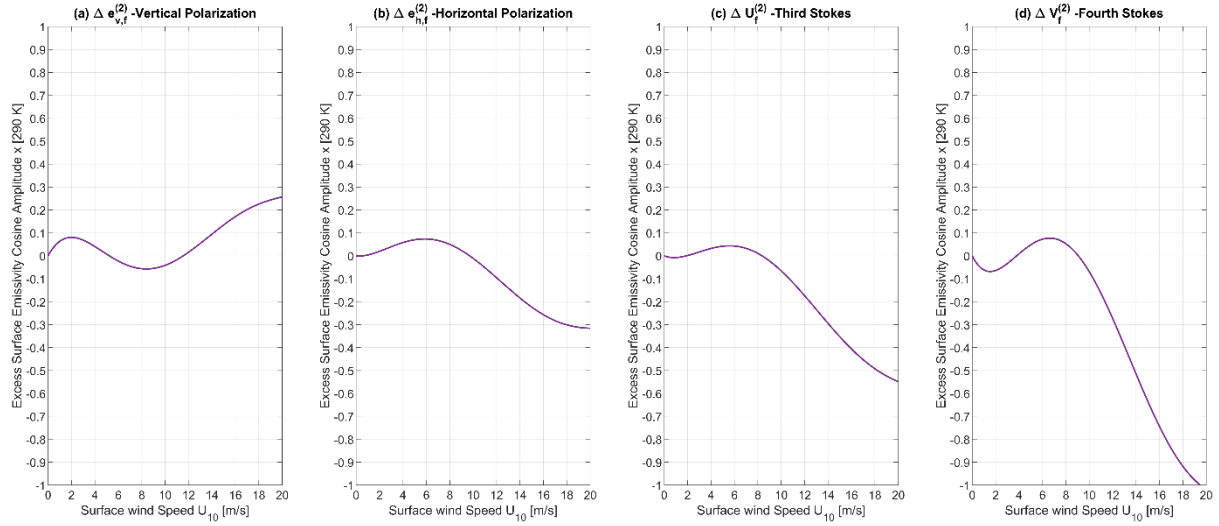


Figure 11: GMF of the second azimuthal harmonic coefficients $\Delta e_{p,f}^{(2)}(\theta_{ref}, U_{10})$ as a function of surface wind speed at L-band for (a) V-polarization, (b) H-polarization, (c) Third Stokes parameter and (d) fourth Stokes parameter. The GMF are for the L-band reference incidence angle of $\theta_{ref} = 52^\circ$ and SST=290 K.

The relative polarization behavior is consistent with the characteristics of higher-frequency observations. At a wind speed of 20 m/s, the peak-to-peak change of $\Delta e_{v,f}^{(1)}$ in vertical-polarization is about 0.5 K at L-band. At the same wind speed in horizontal polarization, the peak-to-peak change of $\Delta e_{h,f}^{(1)}$, decreases to about ~0.1 K. The peak-to-peak change of the second harmonic $\Delta e_{v,f}^{(2)}$, in vertical-polarization is ~0.3 K at L-band. In horizontal-polarization, $\Delta e_{v,f}^{(2)}$, peak-to-peak change is about 0.25 K at L-band. As shown in Figure 10 and Figure 11, the wind direction signal is in all Stokes parameters for sea surface emission (Bespalova *et al.* [1982]; Gasiewski and Kunkee [1994]; Trokhimovski *et al.* [1995]; Yueh [1997]). The Fourth Stokes parameter first harmonic is almost zero for all wind speed and frequencies. The V parameter second harmonic is higher than the first harmonic and can reach peak-to-peak change of 1 K at 1.4 GHz. Note that everything above, say 17 m/s, is pretty much guess work. Some algorithm keep the signals constant above 24.5 m/s or use linear extrapolation of the GMFs. The third stokes harmonics amplitude (and therefore sensitivity to wind direction) are significantly reduced (by about a factor 2) at L-band with respect higher frequencies (X- and Ka-band to stay below 0.5 K peak-to-peak for most wind speed conditions < 15 m/s), making the retrieval of wind direction from L-band third stokes rather challenging. Note however that according to Aquarius and SMAP data, V directional asymmetries seem larger at L-band than at the higher CIMR frequency-band.

f [GHz]	Pol	k=1	k=2	k=3	k=4	k=5
1.4	v	9.1197181e-03	-3.0431623e-03	5.083957e-04	-2.037598e-05	2.458082e-07
1.4	h	9.6160121e-03	-4.3505334e-03	6.07180e-04	-2.753646e-05	4.073317e-07
1.4	U	2.1437e-05	1.84e11e-06	-1.044e-06	4.3478e-08	-5.3051e-10
1.4	V	-1.3375e-05	5.3239e-06	-6.5753e-07	4.2225e-08	-8.0259e-10

Table 3: Coefficients $\alpha_{1,k}^{p,f}$ of the first azimuthal harmonic coefficients in (Eq.41) for the L band at a reference SST of 290K at reference incidence angle $\theta_{ref}=52^\circ$ (L-band).

f [GHz]	Pol	k=1	k=2	k=3	k=4	k=5
1.4	p	9.3408423E-02	9.3408423E-02	9.3408423E-02	9.3408423E-02	9.3408423E-02
1.4	h	-5.197487E-03	-5.197487E-03	-5.197487E-03	-5.197487E-03	-5.197487E-03
1.4	U	-6.5015E-05	-6.5015E-05	-6.5015E-05	-6.5015E-05	-6.5015E-05
1.4	V	-3.4803E-04	1.5574E-04	-2.0192E-05	9.3006E-07	-1.4414E-08

Table 4: Coefficients $\alpha_{2,k}^{p,f}$ of the second azimuthal harmonic coefficients in (Eq.41) for the L-, C-, X-, Ku- and Ka-bands at a reference SST of 290K at reference incidence angle $\theta_{ref}=52^\circ$ (L-band) and $\theta_{ref}=55^\circ$ (C-, X-, Ku- and Ka bands).

8.5.4 Functional flow diagram

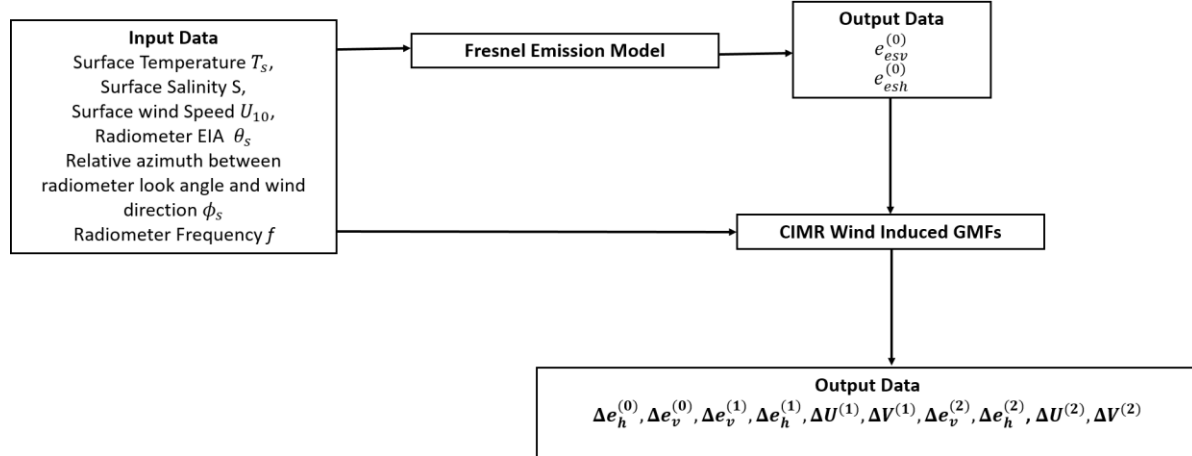


Figure 12: Flowchart of the microwave rough ocean surface emissivity model used in this ATBD

8.6 Atmospheric contributions

Our forward model algorithm for atmospheric corrections for CIMR data consists in:

- Input co-localized auxiliary atmospheric parameters (pressure, temperature, relative humidity, cloud water,...), obtained from e.g., ECMWF atmospheric forecast model on multiple levels,
- Attenuation rates and atmospheric absorption are estimated on N-layers along the vertical from ground to satellite altitude using the Milimeter Wave Propagation Model (MPM) and finally integrated along the path from target to satellite.

8.6.1 Physics of the problem

Electromagnetic Wave Propagation through the Atmosphere

At low microwave frequencies, atmospheric scattering can be neglected for the cases of interest where there is little or no precipitation. To begin the development, the electric field components in the plane normal to the propagation direction may be written as

$$\begin{aligned} E_h(r, t) &= \Re\{\widehat{E}_h(r, t)\} = \Re\{a_h e^{i(kr - \omega t - \phi_h)}\} \\ E_v(r, t) &= \Re\{\widehat{E}_v(r, t)\} = \Re\{a_v e^{i(kr - \omega t - \phi_v)}\} \end{aligned} \quad (\text{Eq.25})$$

where ϕ_h and ϕ_v are constant phases, r is distance along the propagation path, k is wavenumber magnitude, ω is the radiation frequency, t is time, and the real amplitudes $a_h(r)$ and $a_v(r)$ are functions of propagation distance r . In general, as the radiation propagates through the atmosphere it experiences changes in the dielectric properties of the medium. We will assume that the amplitude coefficients satisfy the simple ordinary different equations:

$$\frac{da_h}{dr} = -b(r)a_h(r) \quad (\text{Eq.26})$$

$$\frac{da_v}{dr} = -b(r)a_v(r) \quad (\text{Eq.27})$$

In reality, the amplitude attenuation rate $b(r)$ is a function of space and time and may be computed using molecular oxygen (O_2) and water vapor concentration profiles along with atmospheric physical temperature and pressure profiles. The attenuation rate, or attenuation coefficient, b (typically expressed in units of nepers per meter), generally is a complicated function of atmospheric state (i.e. pressure, temperature, water content in various forms, etc.). Multiplying (Eq.26) by $a_h(r)$ and (Eq.27) by $a_v(r)$ and rearranging yields:

$$\frac{da_h^2}{dr} = -2b(r)a_h^2(r) \quad (\text{Eq.28})$$

$$\frac{da_v^2}{dr} = -2b(r)a_v^2(r) \quad (\text{Eq.29})$$

Similarly, multiplying (Eq.26) by $a_v(r)$ and (Eq.27) by $a_h(r)$ and adding yields

$$\frac{da_v a_h}{dr} = -2b(r)a_v(r)a_h(r) \quad (\text{Eq.30})$$

If the attenuation rate b is independent of spatial location and time, and if we let the electric field amplitudes at some reference location (at which $r = 0$) be a_{ho} and a_{vo} , then

$$a_h(r) = a_{ho}e^{-br}, a_v(r) = a_{vo}e^{-br} \quad (\text{Eq.31})$$

so that

$$\begin{aligned} E_h(r, t) &= \Re\{\widehat{E}_h(r, t)\} = \Re\{a_{ho}e^{i(kr-\omega t-\phi_h)-br}\} \\ E_v(r, t) &= \Re\{\widehat{E}_v(r, t)\} = \Re\{a_{vo}e^{i(kr-\omega t-\phi_v)-br}\} \end{aligned} \quad (\text{Eq.32})$$

where a_{ho} and a_{vo} are the real amplitude of the components at some reference location $r=0$. We may also represent this attenuation rate as an imaginary part of the wavenumber magnitude k , so that we let:

$$\tilde{k} = k + ib = \tilde{k}_r + i\tilde{k}_i \quad (\text{Eq.33})$$

where now $\Re(\tilde{k})$ gives the propagation speed in terms of ω while $\Im(\tilde{k})$ gives the attenuation rate.

$$\begin{aligned} E_h(r, t) &= \Re\{\widehat{E}_h(r, t)\} = \Re\{a_{ho}e^{i(\tilde{k}r-\omega t-\phi_h)}\} \\ E_v(r, t) &= \Re\{\widehat{E}_v(r, t)\} = \Re\{a_{vo}e^{i(\tilde{k}r-\omega t-\phi_v)}\} \end{aligned} \quad (\text{Eq.34})$$

The complex wavenumber magnitude \tilde{k} is the key quantity required to model the radiation propagation (including curvature in propagation path) and attenuation along the path, and here we use the Millimeter-wave Propagation model of [Liebe et al., 1993] (hereafter referred to as the MPM93), which is a refined version of the model presented in [Liebe et al., 1989], to compute \tilde{k} as a function of atmospheric state along the radiation propagation path. As \tilde{k} depends mostly on molecular oxygen concentration and, to a lesser extent, water vapor concentration, the key atmospheric variables required are dry air pressure and water vapor mixing ratio. The Millimeter-wave Propagation model provides an explicit expression for the so-called complex index of refraction, denoted by N , which is defined so that

$$\tilde{k} = k + ib = \tilde{k}_r + i\tilde{k}_i = k + kN = k + k(N_o + N'_o) + iN'' \quad (\text{Eq.35 52})$$

Where N_o , N'_o , and N'' are all real quantities that depend upon the atmospheric state. N_o is independent of frequency while N'_o , and N'' depend on frequency, in general. The real and imaginary parts of complex index of refraction are related to the real and imaginary parts of the complex wavenumber by the equations:

$$\begin{aligned}\widetilde{k}_r &= k(1 + N_0 + N') \\ \widetilde{k}_t &= b(r) = kN''\end{aligned}\quad (\text{Eq.36})$$

Thus, N'' corresponds to the loss portion of \tilde{k} while N_0+N' corresponds to the propagation speed portion of \tilde{k} . It follows that the corresponding amplitude attenuation rate, $b(r)$, expressed in nepers per meter, is:

$$b(r) = kN'' = \left(\frac{2\pi\nu}{c}\right) N'' \quad [\text{Np. m}^{-1}] \quad (\text{Eq.37})$$

and the *power* attenuation rate is

$$a(r) = 2b(r) = 2kN'' = \left(\frac{4\pi\nu}{c}\right) N'' \quad [\text{Np. m}^{-1}] \quad (\text{Eq.38})$$

where c is the speed of light in a vacuum (m s^{-1}) and ν is the electromagnetic frequency in hertz. The index of refraction as provided by the MPM93, $\tilde{N} = \tilde{N}_0 + \tilde{N}' + \tilde{N}''$ is expressed in ppm (i.e., it is scaled by 10^6) so that for $b(r)$ in nepers per meter, we have:

$$\widetilde{k}_t(r) = b(r) = kN'' = \left(\frac{2\pi f\nu}{c}\right) \cdot 10^{-6} \cdot N'' \quad [\text{Np. m}^{-1}] \quad (\text{Eq.39})$$

or for $b(r)$ in dB km⁻¹ with ν in gigahertz,

$$b(r) = kN'' = \left(\frac{2\pi\nu}{c}\right) \cdot \left(\frac{10}{\log_{10} N_p} \frac{\text{dB}}{\text{Np}}\right) \cdot \left(10^3 \frac{\text{m}}{\text{km}}\right) \cdot \left(10^9 \frac{\text{Hz}}{\text{GHz}}\right) \cdot 10^{-6} \cdot \tilde{N}'' \approx 0.0910\nu\tilde{N}'' \quad [\text{dB. km}^{-1}] \quad (\text{Eq.40})$$

The real part of the complex wavenumber, $\tilde{k}_r(r)$, is

$$\tilde{k}_r(r) = \frac{360}{2\pi} \left(\frac{\text{deg}}{\text{rad}}\right) \left(\frac{2\pi\nu}{c}\right) \cdot \left(10^3 \frac{\text{m}}{\text{km}}\right) \cdot \left(10^9 \frac{\text{Hz}}{\text{GHz}}\right) \cdot [1 + 10^{-6} \cdot (\tilde{N}_0 + \tilde{N}')] \quad [\text{deg. km}^{-1}] \quad (\text{Eq.41})$$

The variable part of the preceding expression for $\tilde{k}_r(r)$ is called the *phase dispersion*, β , and is approximately

$$\beta = 1.2\nu(\tilde{N}_0 + \tilde{N}') \quad [\text{deg. km}^{-1}] \quad (\text{Eq.42})$$

with ν expressed in gigahertz and \tilde{N}_0 , and \tilde{N}' expressed in ppm. From $\tilde{k}_r(r)$ we can derive the wave propagation speed $\tilde{c}(r)$:

$$\tilde{c}(r) = 1000 \cdot \frac{\omega}{\tilde{k}_r(r)} \left(\frac{\text{deg.s}^{-1}}{\text{deg.km}^{-1}}\right) = 1000 \cdot \frac{360\nu}{\tilde{k}_r(r)} \left(\frac{\text{deg.s}^{-1}}{\text{deg.km}^{-1}}\right) = c[1 + 10^{-6} \cdot (\tilde{N}_0 + \tilde{N}')]^{-1} \quad [\text{m. s}^{-1}] \quad (\text{Eq.43})$$

where as before c is expressed in meters per second and \tilde{N}_0 and \tilde{N}' are expressed in ppm as in the MPM93. If we were concerned about propagation path curvature, we would need to use

this expression to derive the propagation path for each point in director cosine coordinates. But we will assume that at CIMR L-band frequency, such curvature effects are negligible.

Next, we will examine the formulation of \tilde{N}_0 , and \tilde{N}' in the MPM93 and then relate the total refractive index \tilde{N}_0 , and \tilde{N} to the Stokes vector, which is our primary concern.

Formulation of the Atmospheric Refractive Index

As formulated in the MPM93, the total index of refraction is the sum of indices of refraction owing to

- molecular oxygen (\tilde{N}_D),
- water vapor (\tilde{N}_V),
- cloud water (\tilde{N}_W)
- ice water (\tilde{N}_I), and,
- rain (\tilde{N}_R)

so that:

$$\tilde{N}(T_r, e, p_d, v) = \tilde{N}_0 + \tilde{N}' + iN'' = \tilde{N}_D(T_r, e, p_d, v) + \tilde{N}_V(T_r, e, p_d, v) + \tilde{N}_W(T_r, \rho_w, v) + \tilde{N}_I(T_r, \rho_i, f) + \tilde{N}_R(R, z, f) \quad [\text{ppm}] \quad (\text{Eq.44})$$

where

p_d and e are the partial pressures of dry air and water vapor (hPa), respectively;

ρ_w and ρ_i are the liquid water and ice densities (g m^{-3}), respectively;

R is the rain rate at altitude z ,

T_r is the reciprocal temperature, defined by:

$$T_r = \frac{300}{T_p} \quad (\text{Eq.45})$$

where T_p is the physical temperature in kelvin. The indices of refraction are expressed in the MPM93 in terms of the reciprocal temperature, partial pressures of dry air and water vapor (which is a function of relative humidity and temperature), and cloud water and ice densities (not mixing ratios). The molecular oxygen concentration is a function of the partial pressure of dry air, p_d (expressed in hPa), which is approximately equal to the total pressure p_t minus the partial pressure of water vapor e :

$$p_d = p_t - e \quad (\text{Eq.46})$$

Following Liebe et al., 1993, we introduce the following approximation to the water saturation vapor pressure over a plane surface of water:

$$e_s(T_r) = 2.408 \times 10^{11} T_r^5 e^{-22.644 T_r} \quad (\text{Eq.47})$$

Using this approximation, the partial pressure of water vapor in hectopascals is:

$$e(T_r, r_H) = e_s(T_r) \frac{r_H}{100} \cdot 2.408 \times 10^{11} T_r^5 e^{-22.644 T_r} \quad (\text{Eq.48})$$

where r_H is the relative humidity in percent. The dry air density is given in [kg/m^3],

$$\rho = \frac{p_d \times 100}{(R_d \times T_r)} \quad (\text{Eq.49})$$

where $R_d = 287.1 \text{ J kg}^{-1} \text{ K}^{-1}$ and p_d is the dry air pressure in [hPa]. The density of cloud water in [kg/m^3] is defined as the product of the dry air density ρ by the cloud water mixing ratio m_{clw} , which is defined as the ratio of the mass of water to the mass of dry air, and it has units of [kg/kg].

$$\rho_w = \rho \cdot m_{clw} \quad (\text{Eq.50})$$

The **dry air index of refraction owing to molecular oxygen** (\tilde{N}_D), consists of a nondispersive term \tilde{N}_d , a nonresonant term \tilde{N}_n , and a sum over relevant molecular oxygen absorption lines:

$$\tilde{N}_D(T_r, e, p_d, v) = \tilde{N}_d + \tilde{N}_n + \sum_{k=1}^{44} S_k F_k \quad [\text{ppm}] \quad (\text{Eq.51})$$

The nondispersive term is

$$\tilde{N}_d = 0.2588 p_d T_r \quad [\text{ppm}] \quad (\text{Eq.52})$$

and the nonresonant term is given by the sum of a relaxation spectrum term $S_o F_o$ and a term associated with pressure-induced N_2 absorption (which makes a small contribution above 100 GHz), $S_n F_n$:

$$\tilde{N}_n = S_o F_o + S_n F_n \quad (\text{Eq.53})$$

with

$$S_o = 6.14 \times 10^{-5} p_d T_r^2 \quad [\text{ppm}] \quad (\text{Eq.54})$$

$$F_o = -v[v + i 0.56 \times 10^{-3} (p_d + e) T_r^{0.8}]^{-1} \quad [\text{ppm}] \quad (\text{Eq.55})$$

$$S_n = 1.4 \times 10^{-12} p_d^2 T_r^{3.5} \quad [\text{ppm}] \quad (\text{Eq.56})$$

$$F_n = v[1 + 1.93 \times 10^{-5} v^{1.5}]^{-1} \quad [\text{ppm}] \quad (\text{Eq.57})$$

In the sum over absorption lines, $\sum_{k=1}^{44} S_k F_k$, the individual line strengths are given by:

$$S_k = 1 \times 10^{-6} \frac{a_1}{v_k} p_d T_r^3 \exp[a_2(1 - T_r)] \quad [\text{ppm}] \quad (\text{Eq.58})$$

where a_1 and a_2 are constants for each line. The line form (or line spreading) factor, known as the Van Vleck-Weisskopf function, is given by

$$F_k = \nu \left[\frac{1-i\delta_k}{\nu_k - \nu - i\gamma_k} - \frac{1+i\delta_k}{\nu_k + \nu + i\gamma_k} \right] \quad (\text{Eq.59})$$

with the overlap parameter δ_k given by

$$\delta_k = 1 \times 10^{-3} (a_5 + a_6 T_r) (p_d + e) T_r^{0.8} \quad (\text{Eq.60})$$

where a_5 and a_6 are constants for each line. The width parameter γ_k is given by

$$\gamma_k = (\widetilde{\gamma}_k^2 + 2.25 \times 10^{-6})^{1/2} \quad [\text{GHz}] \quad (\text{Eq.61})$$

With

$$\widetilde{\gamma}_k = 1 \times 10^{-3} a_3 (p_d T_r^{a_4} + 1.1 e T_r) \quad [\text{GHz}] \quad (\text{Eq.62})$$

where a_3 and a_4 are constants for each line. The difference between γ_k and $\widetilde{\gamma}_k$ is related to the Zeeman effect in which absorption lines are split into multiple lines.

The **index of refraction for water vapor** is the sum of a nondispersive term, a continuum term, and a sum over 35 resonant absorption lines (including one pseudo-line at 1780 GHz). At L-band the continuum term is negligible so that

$$\tilde{N}_v(T_r, e, p_d, \nu) = \tilde{N}_v + \sum_{k=1}^{35} S_k^{(\nu)} F_k^{(\nu)} \quad [\text{ppm}] \quad (\text{Eq.63})$$

The nondispersive term is:

$$\tilde{N}_v(T_r, e, p_d, \nu) = (4.163 T_r + 0.239) e T_r \quad [\text{ppm}] \quad (\text{Eq.64})$$

The absorption line strength in the sum over the lines is

$$S_k^{(\nu)} = \left(\frac{b_1}{\nu_k} \right) e T_r^{3.5} \exp [b_2 (1 - T_r)] \quad (\text{Eq.65})$$

where b_1 and b_2 are constants defined for each line k . The line form function has the same form as for oxygen except that there is no line overlap effect:

$$F_k^{(\nu)} = \nu \left[\frac{1}{\nu_k^{(\nu)} - \nu - i\gamma_k^{(\nu)}} - \frac{1}{\nu_k^{(\nu)} + \nu + i\gamma_k^{(\nu)}} \right] \quad (\text{Eq.66})$$

For a total pressure above 0.7 hPa, the width of a pressure-broadened vapor line, $\gamma_k^{(\nu)}$ is given by

$$\gamma_k^{(\nu)} = 1 \times 10^{-3} b_3 (b_4 e(e_s(T_r), r) T_r^{b_6} + p_d T_r^{b_5}) \quad [\text{GHz}] \quad (\text{Eq.67})$$

where b_3 , b_4 , b_5 and b_6 are constants defined for each line k . Below 0.7 hPa doppler broadening can be significant, so that in this case $\gamma_k^{(\nu)}$ is modified to be

$$\gamma_k^{(\nu)} = 0.535 \tilde{\gamma}_k^{(\nu)} + (0.217 (\tilde{\gamma}_k^{(\nu)})^2 + \gamma_D^2)^{1/2} \quad [\text{GHz}] \quad (\text{Eq.68})$$

where $\tilde{\gamma}_k^{(v)}$ is given by

$$\tilde{\gamma}_k^{(v)} = 1 \times 10^{-3} b_3 (b_4 e(e_s(T_r), r) T_r^{b_6} + p_d T_r^{b_5}) \quad [\text{GHz}] \quad (\text{Eq.69})$$

and the Doppler width γ_D is

$$\gamma_D = 1.46 \times 10^{-6} \nu_k^{(v)} T_r^{1/2} \quad (\text{Eq.70})$$

The **liquid water index of refraction** is given by

$$\tilde{N}_W(T_r, \rho_w, v) = 1.5 \rho_w \left(\frac{\epsilon_w - 1}{\epsilon_w + 2} \right) \quad [\text{ppm}] \quad (\text{Eq.71})$$

which is a function of both the cloud water density ρ_w (g m^{-3}) and the complex permittivity of pure water ϵ_w . The complex permittivity of pure water, in turn, is approximated by a double-Debye fit to measured data,

$$\epsilon_w = \epsilon_0 - f \left(\frac{\epsilon_0 - \epsilon_1}{v + i\gamma_1} + \frac{\epsilon_1 - \epsilon_2}{v + i\gamma_2} \right) \quad (\text{Eq.72})$$

With

$$\begin{aligned} \epsilon_0 &= 77.66 + 103.3(T_r - 1) \\ \epsilon_1 &= 0.0671\epsilon_0 \\ \epsilon_2 &= 3.52 - 7.52(T_r - 1) \\ \gamma_1 &= 20.2 - 146.4(T_r - 1) + 316(T_r - 1)^2 \quad [\text{GHz}] \\ \gamma_2 &= 39.8 \gamma_1 \quad [\text{GHz}] \end{aligned} \quad (\text{Eq.73})$$

Here, ϵ_0 and ϵ_1 are the static and high-frequency permittivities, respectively; ϵ_2 is a model parameter which has a slight temperature dependence that has been removed in [Liebe et al., 1993] in order to avoid unphysical behavior for supercooled water above 100 GHz. As we do not consider liquid water effects below freezing, we retain this dependence. The parameters γ_1 and γ_2 are two relaxation frequencies expressed in gigahertz; ρ_w (g m^{-3}) is the liquid water density and v is the radiation frequency in gigahertz.

The **index of refraction for ice** is given by

$$\tilde{N}_I(T_r, \rho_i, f) = 1.5 \left(\frac{\rho_i}{0.916} \right) \left(\frac{\epsilon_i - 1}{\epsilon_i + 1} \right) \quad [\text{ppm}] \quad (\text{Eq.74})$$

where ρ_i is the ice water density (g m^{-3}). The permittivity of ice, ϵ_i is given as a function of electromagnetic frequency and reciprocal temperature by

$$\epsilon_i = 3.15 + i \left(\frac{a_i}{v} + b_i v \right) \quad (\text{Eq.75})$$

Where

$$a_i = (T_r - 0.171) \exp [17.0 - 22.1 T_r] \quad [\text{GHz}] \quad (\text{Eq.76})$$

$$b_i = 1 \times 10^{-5} \left[\left(\frac{0.233}{1 - \frac{0.993}{T_r}} \right)^2 + \frac{6.33}{T_r} - 1.31 \right]_r \quad [\text{GHz}^{-1}] \quad (\text{Eq.77})$$

Formulation of the index of refraction for rain

Refractivity of rain, \tilde{N}_R is governed by absorption and scattering effects. Substantial interactions take place when drop diameters (0.1 to 5 mm) and radio wavelengths become comparable. Bypassing elaborate, lengthy Mie calculations which require drop shape and size distributions as well as the dielectric permittivity of water, the following approximations are used,

$$\tilde{N}_R(R, z, f) = R \cdot (0.012R - 3.7) \cdot \frac{y^{2.5}}{f_R(1+y^{2.5})} + i \cdot C_R \cdot R^Z \quad (\text{Eq.78})$$

where R is the rain rate in [mm/h], z the altitude, $y = f/f_R$, $f_R = 53R(0.37 - 0.0015R)$, $C_R = x_1$ and $z = z = x_2 \cdot f \cdot y_2$, where $x_1 = 3.51e-4$, $y_1 = 1.03$, $x_2 = 0.851$ and $y_2 = 0.158$ for $f = 1.4$ GHz.

8.6.2 Effects on the Stokes vector

For a deterministic signal, the coefficients $a_h(r)$ and $a_v(r)$ in Eq.28- Eq.31 may be considered to be functions of distance, but for a non-deterministic signal these coefficients must be considered to be random variables, and in this case we are primarily interested in the second moments of the electric field vector. As such, we are concerned with the effect of the atmosphere on the Stokes vector,

$$\begin{pmatrix} I \\ Q \\ U \\ V \end{pmatrix} = \mathcal{K} \begin{pmatrix} \langle E_v E_v^* + E_h E_h^* \rangle \\ \langle E_v E_v^* - E_h E_h^* \rangle \\ 2\Re\langle E_v E_h^* \rangle \\ 2\Im\langle E_v E_h^* \rangle \end{pmatrix} = \begin{pmatrix} \langle a_v^2 + a_h^2 \rangle \\ \langle a_v^2 - a_h^2 \rangle \\ 2\langle a_v a_h \cos(\delta_o) \rangle \\ 2\langle a_v a_h \sin(\delta_o) \rangle \end{pmatrix} \quad (\text{Eq.80})$$

where $\kappa = \frac{\lambda^2}{k_b \eta_0 B}$ is a constant coefficient that depends upon the receiver bandwidth B , and the electromagnetic wavelength λ .

The amplitude components are now random variables with a polarized and a non-polarized component. We now assume that the atmospheric attenuation rate $b(r)$ is not a random variable, so that the attenuation coefficients may be extracted from the ensemble averages. In this case, Eq.28, Eq 29, and, Eq.30, become, respectively,

$$\frac{d\langle a_h^2 \rangle}{dr} = -2b(r)\langle a_h^2(r) \rangle \quad (\text{Eq.81})$$

$$\frac{d\langle a_v^2 \rangle}{dr} = -2b(r)\langle a_v^2(r) \rangle \quad (\text{Eq.82})$$

$$\frac{d\langle a_v a_h \rangle}{dr} = -2b(r)\langle a_v(r)a_h(r) \rangle \quad (\text{Eq.83})$$

It follows directly from (80), (81), and (82) that the Stokes vector components satisfy the attenuation equations

$$\frac{d}{dr} \begin{pmatrix} I(r) \\ Q(r) \\ U(r) \\ V(r) \end{pmatrix} = -2b(r) \begin{pmatrix} I(r) \\ Q(r) \\ U(r) \\ V(r) \end{pmatrix} \quad (\text{Eq.84})$$

The modified Stokes vector satisfies a similar equation:

$$\frac{d}{dr} \begin{pmatrix} T_h(r) \\ T_v(r) \\ U(r) \\ V(r) \end{pmatrix} = -2b(r) \begin{pmatrix} T_h(r) \\ T_v(r) \\ U(r) \\ V(r) \end{pmatrix} \quad (\text{Eq.85})$$

8.6.3 Atmospheric Emission

The dispersion relation for electromagnetic radiation in free space is

$$\omega = ck = \frac{2\pi c}{\lambda} \quad (\text{Eq.86})$$

where c is the speed of light in free space (m s^{-1}), ω (rad Hz) and $\lambda(\text{m})$ are the electromagnetic radian frequency and wavelength, respectively. Thus,

$$\frac{d\lambda}{d\omega} = -\frac{2\pi c}{\omega^2} = \frac{(2\pi c)\lambda^2}{(2\pi c)^2} = \frac{\lambda^2}{2\pi c} \quad (\text{Eq.87})$$

To compute the atmospheric emission we assume that the atmosphere is characterized by an emissivity $\epsilon(r)$, and that its emission is unpolarized and well-approximated by the Rayleigh-Jeans approximation for blackbody emission multiplied by the (dimensionless) emissivity ϵ

$$I = \epsilon \frac{2\pi c k_b}{\lambda^4} \cdot T_p \cdot \left(\frac{d\lambda}{d\omega} \right) \quad (\text{Eq.88})$$

where I is the emitted power (specifically, the spectral radiance or brightness) with units ($\text{W m}^{-2} \text{sr}^{-1} \text{Hz}^{-1}$), T_p is the physical temperature. Using (Eq.84), Eq. (88) becomes

$$I = \epsilon \frac{k_b}{\lambda^2} \cdot T_p \quad (\text{Eq.89})$$

In the above, k_b is Boltzmann's constant ($1.38 \cdot 10^{-23} \text{ J K}^{-1}$). The emissivity accounts for the fact that the atmosphere emits much less radiation than a blackbody at the same physical temperature. With this modified Rayleigh-Jeans form, the unpolarized atmospheric emission leads to the following ordinary differential equations for the Stokes and modified Stokes vector,

$$\frac{d}{dr} \begin{pmatrix} I(r) \\ Q(r) \\ U(r) \\ V(r) \end{pmatrix} = \epsilon(r) \begin{pmatrix} T_p(r) \\ 0 \\ 0 \\ 0 \end{pmatrix} \quad (\text{Eq.90})$$

$$\frac{d}{dr} \begin{pmatrix} T_h(r) \\ T_v(r) \\ U(r) \\ V(r) \end{pmatrix} = \epsilon(r) \begin{pmatrix} T_p(r) \\ T_p(r) \\ 0 \\ 0 \end{pmatrix} \quad (\text{Eq.91})$$

where now the emissivity $\epsilon = \epsilon(r)$ is a function of location along the propagation path, and the factor k_b/λ^2 does not appear because the Stokes elements implicitly contain this factor in their definition in terms of moments of the electric field.

8.6.4 Combining Attenuation and Emission

Combining the atmospheric attenuation and emission equations, we have

$$\frac{d}{dr} \begin{pmatrix} I(r) \\ Q(r) \\ U(r) \\ V(r) \end{pmatrix} = -2b(r) \begin{pmatrix} I(r) \\ Q(r) \\ U(r) \\ V(r) \end{pmatrix} + \epsilon(r) \begin{pmatrix} T_p(r) \\ 0 \\ 0 \\ 0 \end{pmatrix} \quad (\text{Eq.92})$$

$$\frac{d}{dr} \begin{pmatrix} T_h(r) \\ T_v(r) \\ U(r) \\ V(r) \end{pmatrix} = -2b(r) \begin{pmatrix} T_p(r) \\ T_p(r) \\ U(r) \\ V(r) \end{pmatrix} + \epsilon(r) \begin{pmatrix} T_p(r) \\ T_p(r) \\ 0 \\ 0 \end{pmatrix} \quad (\text{Eq.93})$$

Interestingly, with the assumptions we have made, the third and fourth Stokes parameters are affected by attenuation but not by emission. Having established the ordinary differential equation that describes the change in the Stokes vector along the propagation path, we now turn to the problem of implementing a solution procedure that is practical for scene modeling. The straightforward approach is to ignore refraction and to integrate along linear paths through the atmosphere, and this is the approach we shall take.

8.6.5 Relating Attenuation to Emission

In general, radiative transfer scattering may be important, so that attenuation may involve both absorption and scattering. At L-band, however, attenuation is dominated by absorption, even in the presence of cloud droplets and ice, so we may assume that the emissivity is equal to the power attenuation rate (twice the amplitude attenuation rate):

$$\epsilon(r) \approx 2b(r) \quad (\text{Eq.94})$$

Given the similar forms for all Stokes vector components, in what follows we will discuss attenuation we will use the compact Stokes vector notation

$$\frac{d}{dr} \mathbf{T} = -2b(r)\mathbf{T} + b(r)\mathbf{T}_p \quad (\text{Eq.95})$$

where \mathbf{T} is the modified Stokes vector (with orthogonal linear components rather than I and Q) above) and

$$\mathbf{T}_p = \epsilon(r) \begin{pmatrix} T_p(r) \\ T_p(r) \\ 0 \\ 0 \end{pmatrix} \quad (\text{Eq.96})$$

We will be concerned about propagation of radiation in the atmosphere at some zenith angle θ from the vertical direction, so we let $r = z \sec \theta$ be the path length in the propagation direction. We assume that, for a given location in the director cosine coordinates system of the CIMR antenna, we can compute the propagation path. As noted in the development above, in general this path will be curved if the propagation speed c (related to the real part of \tilde{k}) is a function of position. However, we will neglect this curvature in what follows. At each point of the director cosine grid for which the line-of-sight intersects the earth, the zenith angle is assumed to be identical to the target incidence angle. At each point of the director cosine grid for which the line-of-sight does not intersect the Earth, the signal entering the radiometer will be equal to the sum of the atmospheric attenuated sky/sun/moon noise plus the integrated atmospheric emission along the path. In this case, the zenith angle can be computed directly in the Geographic Frame. In general, refraction should be taken into account when computing the integration path, but for L-band frequencies this refraction is expected to be negligible and so we have neglected it in our algorithm.

8.6.6 Integration of the Radiative Transfer Equation

As mentioned above, our main concern is attenuation and emission along the propagation path, where the *amplitude* attenuation coefficient is given by

$$b(r) = kN'' = 1 \times 10^{-6} \cdot \left(\frac{2\pi\nu}{c} \right) \cdot \mathcal{I}\{\tilde{N}\} \quad [\text{Np. m}^{-1}] \quad (\text{Eq.97})$$

As before, c is the speed of light in a vacuum in meters per second, ν is the electromagnetic frequency in hertz and \tilde{N} is the sum of the individual indices of refraction for dry air, water vapor, cloud water, and cloud ice as given by in previous section:

$$\tilde{N}(T_r, e, p_d, \rho_w, \rho_i, R, \nu) = \tilde{N}_D(T_r, e, p_d, \nu) + \tilde{N}_V(T_r, e, p_d, \nu) + \tilde{N}_W(T_r, \rho_w, \nu) + \tilde{N}_I(T_r, \rho_i, f) + \tilde{N}_R(R, z, f) \quad [\text{ppm}] \quad (\text{Eq.98})$$

Here we have included explicit dependence of each index of refraction on atmospheric parameters T_r, e, p_d, ρ_w and ρ_i . In the forward model we typically take the atmospheric pressure p (derived from geopotential height as a function of pressure), temperature T , relative humidity r_H , and cloud water mixing ratio fields q_c from an atmospheric model such as ECMWF

forecasts. From the fields in the atmospheric model analyses one can compute the water vapor pressure e , from relative humidity r_H , and temperature T (K); we then compute the partial pressure of dry air, p_d from e and p . We assumed that water is entirely ice below freezing and entirely liquid above freezing, with liquid and ice water densities being $\rho_w = \rho_i = \rho_d q_c$, respectively, in their appropriate temperature ranges.

Having obtained T , p_d , e , ρ_w and ρ_i , we then call four MPM93 functions implementing the above equations to compute the indices of refraction owing to dry air, water vapor, and liquid and ice water. The resulting refractive indices are then used to compute the attenuation rates in units of nepers per meter, which are then stored in another file for later spatial integration of the radiative transfer equation.

The solution procedure involves interpolation of the attenuation rates derived from the ECMWF fields onto a uniformly spaced grid with N_a layers with layer bottom heights z_k ranging from $z_s = 0$ km through $z_t = 30$ km with a $\Delta z = 200$ m grid interval in geopotential height z . The power attenuation rates, denoted by $a_D(z)$, $a_V(z)$, $a_W(z)$ and $a_I(z)$, are twice the corresponding amplitude attenuation rates given by $b_D(z)$, $b_V(z)$, $b_W(z)$ and $b_I(z)$. Using these power attenuation rates, we then compute the total absorption for each of these components along vertical paths from the bottom of the domain to each level. For simplicity, here we first form the total power attenuation rate, $a(z)$, which is the sum of the individual attenuation rates of dry air, water vapor, and liquid and ice water:

$$a(z) = 2b(r) = 2kN'' = a_D(z) + a_V(z) + a_W(z) + a_I(z) + a_R(z) \quad (\text{Eq.99})$$

$$a(z) = 2 \times 10^{-6} \cdot \left(\frac{2\pi\nu}{c} \right) \cdot \mathcal{I}\{\tilde{N}\} \quad [\text{Np.m}^{-1}] \quad (\text{Eq.100})$$

$$\begin{aligned} a(z) \\ = 2 \times 10^{-6} \cdot \left(\frac{2\pi\nu}{c} \right) \\ \cdot \mathcal{I}\left\{ N\tilde{N}_D(T_r, e, p_d, v) + \tilde{N}_V(T_r, e, p_d, v) + \widetilde{N}_W(T_r, \rho_w, v) + \tilde{N}_I(T_r, \rho_i, f) + \tilde{N}_R(R, z, f) \right\} \end{aligned} \quad (\text{Eq.101})$$

The integrated attenuation from the surface at height z_s to height z is

$$A^{(u)}(z) = A(z_s, z) = \int_{z'=z_s}^z a(z') dz' \quad (\text{Eq.102})$$

where the superscript denotes integration from below up to height z . Similarly, the integrated attenuation from height z to the top of the atmosphere is

$$A^{(d)}(z) = A(z, z_t) = \int_{z'=z}^{z_t} a(z') dz' \quad [\text{Np}] \quad (\text{Eq.103})$$

where the superscript denotes integration from above down to height z . The corresponding power transmittances for radiation propagating upward from below and downward from above are, respectively

$$\tau^{(u)}(z) = \tau(z_s, z) = \exp[-A^{(u)}(z)] = \exp[-\int_{z'=z_s}^z a(z') dz'] \quad (\text{Eq.104})$$

$$\tau^{(d)}(z) = \tau(z, z_t) = \exp[-A^{(d)}(z)] = \exp[-\int_{z'=z}^{z_t} a(z') dz'] \quad (\text{Eq.105})$$

In discrete form the integrated upward and downward attenuations in nepers are, respectively,

$$A^{(u)}(z_m) = A_m^{(u)} = \sum_{k=1}^m a(z_k) \Delta z \quad [Np] \quad (\text{Eq.106})$$

$$A^{(d)}(z_m) = A_m^{(d)} = \sum_{k=1}^{N_a} a(z_k) \Delta z \quad [Np] \quad (\text{Eq.107})$$

where $A^{(u)}(z_m)$ and $A^{(d)}(z_m)$ have units of nepers since they are attenuation rates integrated over small height ranges. Here the subscript m is an index into the vector of vertical layers that form a discrete vertical grid with layer center heights z_m . The resulting zenith transmissivity between the surface and layer k is then

$$\tau^{(u)}(z_m) = \tau(z_s, z_m) = \exp[-A_m^{(u)}] \quad (\text{Eq.108})$$

In terms of the individual contributions by dry air, water vapor, cloud water and cloud ice, the total transmissivity from the surface to the top of layer z_m is

$$\tau^{(u)}(z_m) = \tau(z_s, z_m) = \exp[-A_m^{(u)}] = \tau_D^{(u)}(z_m) \tau_V^{(u)}(z_m) \tau_W^{(u)}(z_m) \tau_I^{(u)}(z_m) \tau_R^{(u)}(z_m) \quad (\text{Eq.109})$$

while the total transmissivity from the top of the atmosphere to the base of layer z_m is

$$\tau^{(d)}(z_m) = \tau(z_s, z_m) = \exp[-A_m^{(d)}] = \tau_D^{(d)}(z_m) \tau_V^{(d)}(z_m) \tau_W^{(d)}(z_m) \tau_I^{(d)}(z_m) \tau_R^{(d)}(z_m) \quad (\text{Eq.110})$$

Except at near grazing zenith angles, an arbitrary path will not traverse a horizontal distance of more than a few kilometers, and if we assume that the atmosphere on this spatial scale is horizontally uniform, then the total attenuation along a path at zenith angle θ may be obtained from the preceding total attenuation values by multiplication by $\sec\theta$. The transmissivities at zenith angle θ are obtained by raising these zenith transmissivities to the negative $\sec\theta$ power:

$$\begin{aligned} \tau^{(u)}(z_m, \theta) &= \tau(z_s, z_m, \theta) \\ &= \exp[-A_m^{(u)} \sec\theta] = \left[\tau_D^{(u)}(z_m) \tau_V^{(u)}(z_m) \tau_W^{(u)}(z_m) \tau_I^{(u)}(z_m) \tau_R^{(u)}(z_m) \right]^{\sec\theta} \end{aligned} \quad (\text{Eq.111})$$

$$\begin{aligned} \tau^{(d)}(z_m, \theta) &= \tau(z_s, z_m, \theta) = \exp[-A_m^{(d)} \sec\theta] = \\ &\quad \left[\tau_D^{(d)}(z_m) \tau_V^{(d)}(z_m) \tau_W^{(d)}(z_m) \tau_I^{(d)}(z_m) \tau_R^{(d)}(z_m) \right]^{\sec\theta} \end{aligned} \quad (\text{Eq.112})$$

To complete the model, we must account for atmospheric emission. The (assumed to be unpolarized) brightness temperature emitted by the atmosphere per unit height interval at some

height z above the ground (i.e., a brightness temperature *rate*) is, assuming that the atmosphere is in thermal equilibrium,

$$\hat{T}_{ba}(z) = a(z)T_p(z) \quad (\text{Eq.113})$$

where $T_p(z_k)$ is the physical temperature at height z_k and $\hat{T}_{ba}(z_k)$ is a brightness temperature rate with units of kelvin per meter. The total brightness temperature rate of atmospheric emission at the height z_k is, considering all components,

$$\hat{T}_{ba}(z_k) = \hat{T}_{bD}(z_k) + \hat{T}_{bv}(z_k) + \hat{T}_{bw}(z_k) + \hat{T}_{bi}(z_k) + \hat{T}_{bR}(z_k) \quad (\text{Eq.114})$$

We can then vertically integrate this total brightness temperature rate to derive the upwelling attenuated atmospheric brightness temperature at the top of the atmosphere:

$$T_{ba}^{TOA} = \int_{z'=z_s}^{z_t} \hat{T}_{ba}(z_k) \exp\left[-\int_{z''=z'}^{z_t} a(z'') dz''\right] dz' \quad (\text{Eq.115})$$

which in discrete form becomes:

$$T_{ba}^{TOA} = \sum_{k=1}^m \tau^{(d)}(z_k) T_{bak} = \sum_{k=1}^m \tau(z_k, z_t) T_{bak} = \sum_{k=1}^m \tau(z_k, z_t) a(z_k) T_p(z_k) \Delta z \quad (\text{Eq.116})$$

Where

$$T_{bak} \approx a(z_k) T_p(z_k) \Delta z \quad (\text{Eq.117})$$

is the unattenuated incremental brightness temperature of emission in layer k (with units of kelvin). Similarly, the zenith downwelling brightness temperature at the bottom of the atmosphere is

$$T_{ba}^{BOA} = \int_{z'=z_s}^{z_t} \hat{T}_{ba}(z_k) \exp\left[-\int_{z''=z_s}^{z'} a(z'') dz''\right] dz' \quad (\text{Eq.118})$$

which in discrete form becomes

$$T_{ba}^{BOA} = \sum_{k=1}^m \tau^{(u)}(z_k) T_{bak} = \sum_{k=1}^m \tau(z_s, z_k) T_{bak} = \sum_{k=1}^m \tau(z_s, z_k) a(z_k) T_p(z_k) \Delta z \quad (\text{Eq.119})$$

Although T_{ba}^{boa} and T_{ba}^{toa} do not differ much, they are not identical. Since we must model scenes for a satellite radiometer within the antenna patterns, we also need the self-attenuated atmospheric emission at the flight level in an arbitrary direction within the antenna patterns. In general this is a complicated problem because certain directions may involve near-grazing incidence, or even propagation parallel to the ground, in which case refraction and earth curvature effects may become important even at L-band. Here we choose to simplify the problem by neglecting refraction and earth curvature effects in the propagation path modeling. With this simplification, computing the brightness temperature at antenna level z_a and some zenith angle θ owing to self-attenuated atmospheric emission reduces to one possible integral when the path is directed upward the earth's surface:

$$T_{ba}(z) = \sec\theta \int_{z'=z_a}^{z_t} \hat{T}_{ba}(z') \exp\left[-\sec\theta \int_{z''=z_a}^{z'} a(z'') dz''\right] dz', \quad 0^\circ < \theta < 90^\circ \quad (\text{Eq.120})$$

Where $\hat{T}_{ba}(z)$ is given by (Eq.113) and evaluated at height z above the ground. It is important to realize that this is a significant simplification, since in general we would have to integrate along curved paths over the curved surface of the earth, and such curved paths may both decrease and increase in elevation, or even remain parallel to the ground, leading to very large brightness temperatures that may approach the physical atmospheric temperature.

Even with the simplified linear paths, it is not practical to precompute the preceding integrals for all possible antenna heights and zenith angles, and it is also not practical to compute such integrals for each director cosine gridpoint as part of the scene brightness modeling for each measured Stokes vector. Therefore, a further approximation is necessary for practical implementation. The approach we take is to extract the zenith angle dependence from the inner attenuation integrations by expanding the exponentials in series of powers of the integrated path attenuation. Doing so will lead to approximate expressions for the self-attenuated atmospheric emission brightness temperatures in powers of $\sec\theta$, with coefficients that result from integrations along vertical paths only. Such approximate expressions are expected to be reasonable except for nearly horizontal paths. Using

$$e^x = 1 + x + \mathcal{O}(x^2) \quad (\text{Eq.121})$$

we have

$$\exp\left[-\sec\theta \int_{z''=z_a}^{z'} a(z'') dz''\right] \approx 1 - \sec\theta \int_{z''=z_a}^{z'} a(z'') dz'' \quad (\text{Eq.122})$$

Substituting the preceding two approximate transmissivity expressions into (Eq.120), we obtain the approximate brightness temperature at the antenna height:

$$T_{ba}(z) \approx \sec\theta \left[\int_{z'=z_a}^{z_t} \hat{T}_{ba}(z') dz' \right] - \sec^2\theta \left[\int_{z'=z_a}^{z_t} \hat{T}_{ba}(z') \int_{z''=z_a}^{z'} a(z'') dz'' dz' \right], \quad 0^\circ < \theta < 90^\circ \quad (\text{Eq.123})$$

As may be seen, each approximate expression consists of the difference between the unattenuated integrated emission brightness temperature and a term involving attenuation of the brightness along the path. Since all zenith angle dependence has been removed from the integrals, we may precompute these integrals for a fixed antenna elevation and store the results for later calculations at arbitrary zenith angles. In particular, we precompute the following four integrals (each with units of kelvin):

$$\tilde{T}_{bad}^{(0)}(z_a) = \int_{z'=z_a}^{z_t} \hat{T}_{ba}(z') dz' \quad (\text{Eq.124})$$

$$\tilde{T}_{bau}^{(0)}(z_a) = \int_{z'=z_s}^{z_a} \hat{T}_{ba}(z') dz' \quad (\text{Eq.125})$$

$$\tilde{T}_{bad}^{(1)}(z_a) = \int_{z'=z_a}^{z_t} \hat{T}_{ba}(z') \int_{z''=z_a}^{z'} a(z'') dz'' dz' \quad (\text{Eq.126})$$

$$\tilde{T}_{bau}^{(1)}(z_a) = \int_{z'=z_s}^{z_a} \hat{T}_{ba}(z') \int_{z''=z}^{z_a} a(z'') dz'' dz' \quad (\text{Eq.127})$$

These first two functions are the unattenuated *zenith* brightness temperatures associated with emission from above and below the antenna, respectively; the last two functions represent the extent of brightness temperature attenuation for emission from above and below, respectively, that would be obtained at *zenith*. For the algorithm, one can compute these four functions for a range of discrete heights z_m over the horizontal and temporal domain for which we obtained gridded atmospheric data. Then, in the scene modeling process we interpolated these functions to the antenna height and then computed the actual unpolarized attenuated atmospheric emission brightness temperatures at the antenna for arbitrary zenith angle θ , where θ is a function of director cosine coordinates as well as of the antenna orientation. The final self-attenuated unpolarized atmospheric emission brightness temperatures incident at the antenna are

$$T_{ba}(z_a, \theta) \approx \sec\theta \tilde{T}_{bad}^{(0)}(z_a) - \sec^2\theta \tilde{T}_{bad}^{(1)}(z_a), \quad 0^\circ < \theta < 90^\circ \quad (\text{Eq.128})$$

The final expression constitutes the model for self-attenuated Ku- to L-band atmospheric brightness temperature incident at the antenna. This brightness temperature should be applied equally to both all components of the Stokes vector before the antenna gain pattern is applied to compute the final impact on the antenna temperature. This approximate equation has been found to agree very well with the exact calculation (for linear paths). The difference between this approximate and the exact solutions is less than 0.1 K up to about 86° away from zenith for both upwelling and downwelling radiation. The approximation breaks down badly beyond 89° and therefore should not be used in this zenith angle range. In fact, at large zenith angles path and earth curvature may become significant as well, so that this simplified linear path/flat earth model may introduce significant error.

8.6.7 Functional flow diagram

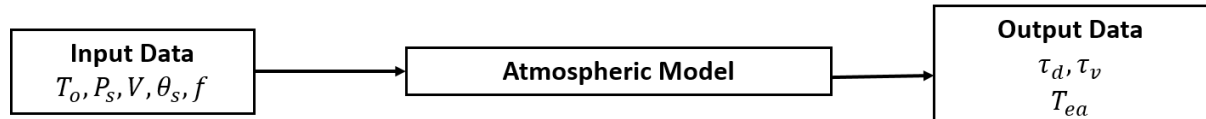


Figure 13: Flowchart of the atmospheric radiative transfer model used in this ATBD. Input data are the air surface temperature T_o , surface pressure P_s , and total column water vapor, and the radiometer incidence angle. Output data are the 1-way atmospheric transmittances associated with molecular oxygen absorption and water vapor along a line of sight at angle from nadir and, the unpolarized brightness temperature of atmospheric 1-way emission.

8.7 Accounting for rotation of the polarization plane in the Stokes vector

In this section, we summarize the Stokes vector transformation that is applied to the forward model from the surface basis to the instrument antenna frame basis, accounting for both a change in polarization basis and the Faraday rotation associated with the passage of radiation through the ionosphere.

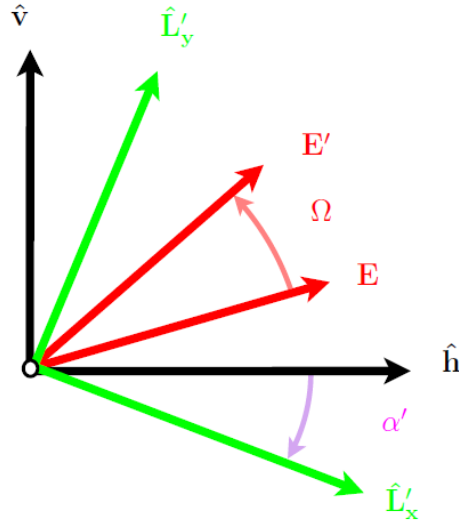


Figure 11. Diagram summarizing the two rotations required to transport a brightness temperature vector from the surface basis $(\hat{\mathbf{h}}, \hat{\mathbf{v}})$ into the instrument Ludwig-3 basis $(\hat{\mathbf{L}}'_x, \hat{\mathbf{L}}'_y)$. Here boresight is into the page so we are looking down towards the target from the instrument. Positive Faraday rotation corresponds to the rotation of the electric field vector \mathbf{E} into \mathbf{E}' by the angle Ω as shown. The additional rotation associated with the change of basis is a further counterclockwise rotation of the electric field vector, or clockwise rotation of the basis $(\hat{\mathbf{h}}, \hat{\mathbf{v}})$ by the angle α' .

8.7.1 From surface polarization basis to Ludwig-3 antenna basis

The first rotation, counterclockwise by angle α' looking down towards the target from the instrument, is associated with the change of polarization basis from the surface basis to the instrument basis (so-called Ludwig-3 basis as defined in Ludwig [1973]), so that:

$$\begin{pmatrix} E_x \\ E_y \end{pmatrix} = \begin{pmatrix} \cos \alpha' & -\sin \alpha' \\ \sin \alpha' & \cos \alpha' \end{pmatrix} \begin{pmatrix} E_h \\ E_v \end{pmatrix} \quad (\text{Eq.129})$$

and the corresponding transformation of the Stokes vector is given by:

$$\begin{pmatrix} T_x \\ T_y \\ U_{xy} \\ V_{xy} \end{pmatrix} = \begin{pmatrix} \cos^2 \alpha' & \sin^2 \alpha' & -\cos \alpha' \sin \alpha' & 0 \\ \sin^2 \alpha' & \cos^2 \alpha' & \cos \alpha' \sin \alpha' & 0 \\ \sin 2\alpha' & -\sin 2\alpha' & \cos 2\alpha' & 0 \\ 0 & 0 & 0 & 1 \end{pmatrix} \begin{pmatrix} T_h \\ T_v \\ U \\ V \end{pmatrix} \quad (\text{Eq.130})$$

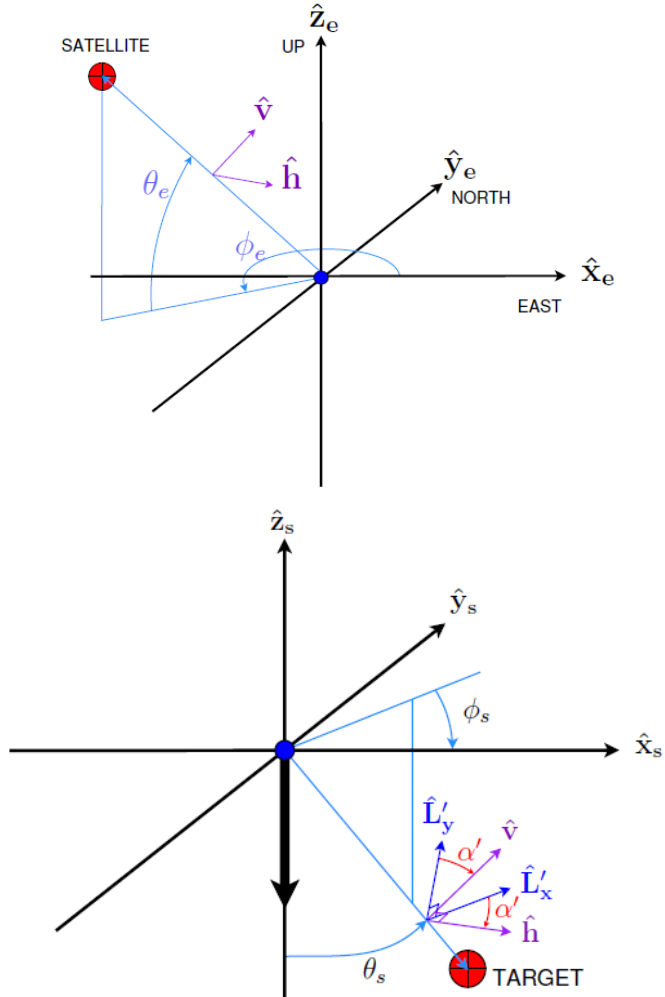


Figure 14: Left : Diagram showing the geometry and polarization basis vectors in the surface target frame, denoted by $(\hat{\mathbf{h}}, \hat{\mathbf{v}})$. The altitude of the emission vector, directed towards the satellite, is θ_e , and the azimuth of this vector, ϕ_e , is measured positive counterclockwise from due east. Right : Diagram showing the geometry in the instrument, or antenna, frame. Ludwig-3 polarization basis vectors are denoted by basis $(\hat{\mathbf{L}}'_x, \hat{\mathbf{L}}'_y)$. The polarisation basis rotation angle α' is the clockwise rotation of the surface $(\hat{\mathbf{h}}, \hat{\mathbf{v}})$ into the instrument Ludwig-3 polarization basis $(\hat{\mathbf{L}}'_x, \hat{\mathbf{L}}'_y)$. Equivalently, this angle is the counterclockwise rotation of the electric field vector looking down towards the target. The angle of the look direction (towards the ground) off of boresight is θ_s , and the azimuth of the look direction ϕ_s , is measured positive clockwise from north.

Figure 14 shows the surface and instrument (Ludwig-3) polarization basis vectors. The polarization basis rotation angle is found using the method introduced by Zundo and Duesman [2010]. In this method, the surface polarization basis vectors have the following cartesian components:

$$\begin{aligned}
 \hat{\mathbf{h}} \cdot \hat{\mathbf{x}}_e &= -\sin \phi_e, \\
 \hat{\mathbf{h}} \cdot \hat{\mathbf{y}}_e &= \cos \phi_e, \\
 \hat{\mathbf{h}} \cdot \hat{\mathbf{z}}_e &= 0, \\
 \hat{\mathbf{v}} \cdot \hat{\mathbf{x}}_e &= -\sin \theta_e \cos \phi_e, \\
 \hat{\mathbf{v}} \cdot \hat{\mathbf{y}}_e &= -\sin \theta_e \sin \phi_e, \\
 \hat{\mathbf{v}} \cdot \hat{\mathbf{z}}_e &= \cos \theta_e
 \end{aligned} \tag{Eq.131}$$

For the instrument polarization basis, the following associations are made:

$$\begin{aligned}\hat{\mathbf{x}}_s &\rightarrow \hat{\mathbf{y}} \\ \hat{\mathbf{y}}_s &\rightarrow \hat{\mathbf{x}} \\ \hat{\mathbf{z}}_s &\rightarrow -\hat{\mathbf{z}}\end{aligned}\quad (\text{Eq.132})$$

Now in the conventional formulation for the Ludwig-3 polarization basis vectors, we denote the vector pointing from the antenna to the target by $\hat{\mathbf{t}}$ and we simply begin by defining the usual « zonal » and « meridional » unit vectors on the sphere and then rotate them about the target vector $\hat{\mathbf{t}}$ by the antenna azimuth ϕ . Thus, we define :

$$\begin{aligned}\hat{e}_\phi &= \frac{\hat{\mathbf{z}} \times \hat{\mathbf{t}}}{\|\hat{\mathbf{z}} \times \hat{\mathbf{t}}\|} = \frac{(\hat{\mathbf{x}} \times \hat{\mathbf{y}}) \times \hat{\mathbf{t}}}{\|(\hat{\mathbf{x}} \times \hat{\mathbf{y}}) \times \hat{\mathbf{t}}\|} = \frac{\hat{\mathbf{y}}(\hat{\mathbf{t}} \cdot \hat{\mathbf{x}}) - \hat{\mathbf{x}}(\hat{\mathbf{t}} \cdot \hat{\mathbf{y}})}{\|\hat{\mathbf{y}}(\hat{\mathbf{t}} \cdot \hat{\mathbf{x}}) - \hat{\mathbf{x}}(\hat{\mathbf{t}} \cdot \hat{\mathbf{y}})\|} \\ \hat{e}_\theta &= (\hat{\mathbf{z}} \times \hat{\mathbf{t}}) \times \hat{\mathbf{t}}\end{aligned}\quad (\text{Eq.133})$$

For convenience, we also define the corresponding unnormalized polarization vectors:

$$\begin{aligned}e_\phi &= \hat{\mathbf{y}}(\hat{\mathbf{t}} \cdot \hat{\mathbf{x}}) - \hat{\mathbf{x}}(\hat{\mathbf{t}} \cdot \hat{\mathbf{y}}) \\ e_\theta &= (\hat{\mathbf{z}} \times \hat{\mathbf{t}}) \times \hat{\mathbf{t}} = (\hat{\mathbf{z}} \cdot \hat{\mathbf{t}})\hat{\mathbf{t}} - \hat{\mathbf{z}}\end{aligned}\quad (\text{Eq.134})$$

which both have the same length, given by $\|\hat{\mathbf{y}}(\hat{\mathbf{t}} \cdot \hat{\mathbf{x}}) - \hat{\mathbf{x}}(\hat{\mathbf{t}} \cdot \hat{\mathbf{y}})\|$. For simplicity, we will use these latter two vectors, rather than the normalized vectors, in what follows. The Ludwig-3 unnormalized components are defined in terms of the preceding unnormalized vectors by a rotation by the target azimuth in the antenna frame. This rotation is defined so that at boresight, the resulting vectors are now a function of azimuth ϕ :

$$\begin{aligned}\mathbf{L}'_y &= e_\theta \cos \phi - e_\phi \sin \phi \\ \mathbf{L}'_x &= e_\theta \sin \phi + e_\phi \cos \phi\end{aligned}\quad (\text{Eq.135})$$

Now $\cos \phi$ and $\sin \phi$ can be expressed in terms of the target vector and the cartesian basis vector as follows:

$$\begin{aligned}\cos \phi &= -\hat{\mathbf{y}} \cdot \left[\frac{\hat{\mathbf{t}} \times \hat{\mathbf{z}}}{\|\hat{\mathbf{t}} \times \hat{\mathbf{z}}\|} \right] \\ \sin \phi &= \hat{\mathbf{x}} \cdot \left[\frac{\hat{\mathbf{t}} \times \hat{\mathbf{z}}}{\|\hat{\mathbf{t}} \times \hat{\mathbf{z}}\|} \right]\end{aligned}\quad (\text{Eq.136})$$

The normalized Ludwig-3 basis vectors are:

$$\begin{aligned}\hat{\mathbf{L}}'_x &= \mathbf{L}'_x / \|\mathbf{L}'_x\| \\ \hat{\mathbf{L}}'_y &= \mathbf{L}'_y / \|\mathbf{L}'_y\|\end{aligned}\quad (\text{Eq.137})$$

Given a target/satellite position with angles (θ_e, ϕ_e) and (θ_s, ϕ_s) , both the surface polarization basis vectors $(\hat{\mathbf{h}}, \hat{\mathbf{v}})$ and Ludwig-3 basis $(\hat{\mathbf{L}}'_x, \hat{\mathbf{L}}'_y)$ can be determined with the previous equations. To find the clockwise basis rotation of the surface basis into the Ludwig-3 basis, we note that this corresponds to a counterclockwise rotation of the electric field vector itself, and so :

$$\begin{pmatrix} E_x \\ E_y \end{pmatrix} = \begin{pmatrix} \hat{\mathbf{L}}'_x \cdot \hat{\mathbf{h}} & \hat{\mathbf{L}}'_x \cdot \hat{\mathbf{v}} \\ \hat{\mathbf{L}}'_y \cdot \hat{\mathbf{h}} & \hat{\mathbf{L}}'_y \cdot \hat{\mathbf{v}} \end{pmatrix} \begin{pmatrix} E_h \\ E_v \end{pmatrix} = \begin{pmatrix} \cos \alpha' & -\sin \alpha' \\ \sin \alpha' & \cos \alpha' \end{pmatrix} \begin{pmatrix} E_h \\ E_v \end{pmatrix} \quad (\text{Eq.138})$$

Therefore, we have :

$$\begin{aligned} \hat{\mathbf{L}}'_x \cdot \hat{\mathbf{h}} &= \cos \alpha' \\ \hat{\mathbf{L}}'_x \cdot \hat{\mathbf{v}} &= -\sin \alpha' \end{aligned} \quad (\text{Eq.139})$$

and so, the polarization rotation angle α' may be computed as:

$$\alpha' = \text{atan2}(-\hat{\mathbf{L}}'_x \cdot \hat{\mathbf{v}}, \hat{\mathbf{L}}'_x \cdot \hat{\mathbf{h}}) \quad (\text{Eq.140})$$

8.7.2 Faraday Rotation

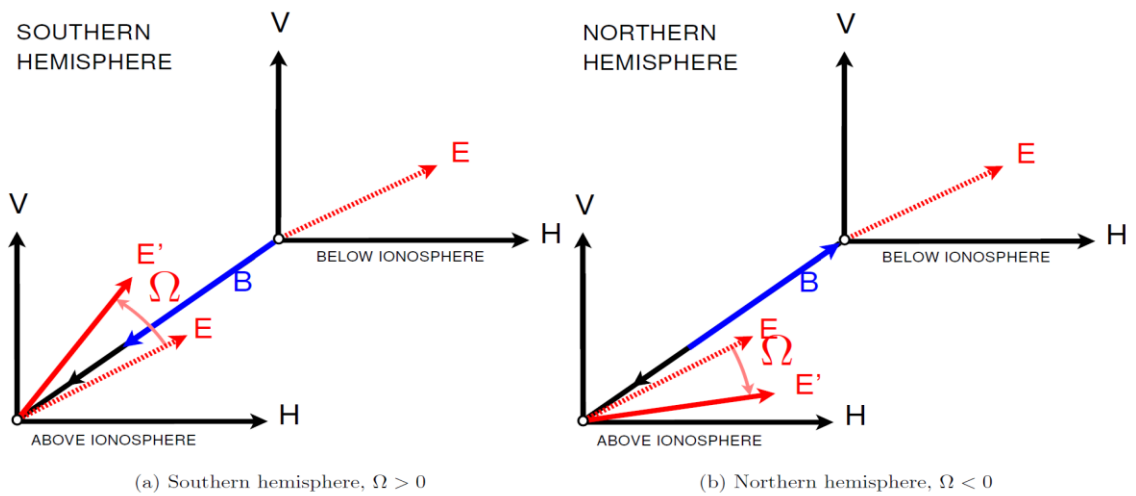


Figure 15: Diagram showing how the sense of Faraday rotation depends upon the relative directions of the magnetic field and energy propagation. Also noted is the expected sense of rotation in each hemisphere.

The polarization vector of an electromagnetic wave of frequency f [Hertz] in the microwave range that propagates from the Earth to the S/C through the geomagnetic field and the Earth's ionosphere undergoes a rotation (Faraday rotation) by the angle Ω (Yueh [2000];Meissner and Wentz [2006]):

$$\Omega = \left(\frac{135}{f^2} \right) \int n_e \vec{B}_{geo} \cdot d\vec{s} \quad (\text{Eq.141})$$

where n_e is the free inospheric electron density [m^{-3}]. \vec{B}_{geo} is the geomagnetic field vector [Gauss] and $d\vec{s}$ is the vector line element in the direction of propagation. When looking into the propagation direction of the electromagnetic wave, the electric field polarization vector rotates clockwise if $\Omega > 0$, i.e., if the geomagnetic field is pointing along the direction of propagation. The Faraday rotation corresponds to the Stokes vector transformation

$$\begin{pmatrix} I'_{hv} \\ Q'_{hv} \\ U'_{hv} \\ V'_{hv} \end{pmatrix} = \begin{pmatrix} 1 & 0 & 0 & 0 \\ 0 & \cos(2\Omega) & \sin(2\Omega) & 0 \\ 0 & -\sin(2\Omega) & \cos(2\Omega) & 0 \\ 0 & 0 & 0 & 1 \end{pmatrix} \begin{pmatrix} I_{hv} \\ Q_{hv} \\ U_{hv} \\ V_{hv} \end{pmatrix} \quad (\text{Eq.142})$$

The corresponding transformation of the modified Stokes vector is

$$\begin{pmatrix} T'_h \\ T'_v \\ U' \\ V' \end{pmatrix} = \begin{pmatrix} (I'_{hv} - Q'_{hv})/2 \\ (I'_{hv} + Q'_{hv})/2 \\ U' \\ V' \end{pmatrix} = \begin{pmatrix} \cos^2 \Omega & \sin^2 \Omega & -\cos \Omega \sin \Omega & 0 \\ \sin^2(\Omega) & \cos^2 \Omega & \cos \Omega \sin \Omega & 0 \\ \sin(2\Omega) & -\sin(2\Omega) & \cos(2\Omega) & 0 \\ 0 & 0 & 0 & 1 \end{pmatrix} \begin{pmatrix} T_h \\ T_v \\ U \\ V \end{pmatrix} \quad (\text{Eq.143})$$

According to Eq.154, the magnitude of the Faraday rotation angle grows with $1/f^2$. For CIMR-like Earth incidence angles and all typical ocean scenes $Q_{hv} \gg U_{hv}$. Therefore, according to Eq.155, for typical values of Ω , the relative impact of Faraday rotation on the third Stokes parameter is much larger than on the second Stokes parameter (vertical and horizontal polarizations). For the CIMR instrument, Faraday rotation plays a significant role only for the third Stokes parameter at 1.4, 6.9, and, 10.7 GHz. At 1.4 GHz, the size of the Faraday rotation is more than 50 times larger than at 10.7 GHz. If not corrected, this would lead to a large relative error in the V- and H-pol brightness temperatures and therefore to inaccurate values for the OWV.

In order to compute the Faraday rotation for CIMR orbits we assume a spherical earth (radius km) and use the thin layer approximation (Le Vine and Abraham [2000]), which assumes that all electrons are concentrated at the ionospheric layer at an altitude $h_I=400$ km above mean sea level:

$$n_e(z, lat, lon) = \delta(z - h_I) VTEC(lat, lon) \quad (\text{Eq.144})$$

where

$$VTEC(lat, lon) = \int_0^{h_{s/c}} n_e(z, lat, lon) dz \quad (\text{Eq.145})$$

is the Vertical Total Electron Content (VTEC) of the ionosphere between the Earth's surface and the S/C altitude $h_{s/c}$. We can then substitute the full profile integral (Eq.141) by

$$\Omega = VTEC \cdot (\vec{B}_I \cdot \vec{k}) \cdot \frac{\partial s(h)}{\partial h} \Big|_{h=h_I} \quad (\text{Eq.146})$$

which can be further expressed as follows:

$$\Omega = (K_f/f^2) \cdot VTEC(h_{s/c}, lat_{400}, lon_{400}) \cdot B_I \cdot \cos \tilde{\theta} \cdot \sec \psi \quad (\text{Eq.147})$$

where $K_f=1.355\times10^4$ TECU⁻¹GHz² T⁻¹, f is the electromagnetic frequency, VTEC is the vertical total electron content reduced to the satellite altitude using the formulation of Flory [2007], B_I is the magnetic field strength [Tesla] evaluated at the ionospheric pierce point (IPP), the point where the ray from the spacecraft to the surface crosses 400 km (lat_{400} , lon_{400}); ψ is the angle the ray makes with the vertical towards the target and $\tilde{\theta}$ is the angle between the magnetic field vector and the ray from spacecraft to the surface. As shown in Figure 15, this angle is generally larger than 90° in the northern hemisphere (with negative Ω) and less than 90° in the southern hemisphere (with positive Ω). The reduction of VTEC to satellite altitude is formulated as two equations, one (morning) for local time within 6 hours of 6 a.m., and the other (evening) for local times within 6 hours of 6 p.m.

$$VTEC(z = h_{s/c}, lat_{400}, lon_{400}) = VTEC(z = \infty, lat_{400}, lon_{400}) \times [(A_m \cdot F_s + B_m) + C_m \cdot \cos(D_m \cdot C_m \cdot lat_{400}(\pi/180))] \quad (\text{Eq.148})$$

Where F_s is the daily solar flux obtained from daily RSGA files [sfu] and the coefficients A_m , B_m , C_m and D_m were determined by N. Flory from ESA to be as provided in Table 4.

The $VTEC(z = \infty, lat_{400}, lon_{400})$ can be obtained from the 1-day forecast produced Centre for Orbit Determination in Europe (CODE), University of Berne, Switzerland.

Coefficient	Morning value (between 00 and 12 LT)	Evening value (between 12 and 24 LT)
A_m	-1.43×10^{-4} [sfu ⁻¹]	-9.67×10^{-5} [sfu ⁻¹]
B_m	8.66×10^{-1} [nd]	8.76×10^{-1} [nd]
C_m	3.75×10^{-3} [nd]	8.98×10^{-3} [nd]
D_m	3.7 [deg ⁻¹]	2.03 [deg ⁻¹]

Table 5: Coefficients in Flory TEC Altitude Correction

The Magnetic field vector is obtained from the 12th generation of the International Geomagnetic Reference Field (IGRF), evaluated at 400 km above the earth's surface along the line of sight using the software provided in <https://www.ngdc.noaa.gov/IAGA/vmod/igrf12.f> as converted into a callable FORTRAN function available here: <https://gist.github.com/myjr52/62ca6c3e9c78ea0411>.

The function outputs magnetic field strength in nanoTeslas (1e-9 Teslas) which is converted into Gauss (1e-4 Teslas). This model is valid to the year 2020 and should be updated when a new version of the model becomes available. Further information on the derivation of the associated geomagnetic model may be found here: <https://www.ngdc.noaa.gov/IAGA/vmod/igrf.html>

8.7.3 Total rotation from surface basis to antenna basis

Of course, Faraday rotation is just one of two rotations necessary to transport a surface Stokes vector into the instrument basis. The second rotation, counterclockwise by angle α' looking down towards the target from the instrument, is associated with the change of polarization basis from the surface basis to the instrument basis. For the chosen CIMR geometry conventions, this polarization basis rotation angle is defined with the same sign convention as that for Ω so that:

$$\begin{pmatrix} E_h^{Ant} \\ E_v^{Ant} \end{pmatrix} = \begin{pmatrix} \cos \alpha' & -\sin \alpha' \\ \sin \alpha' & \cos \alpha' \end{pmatrix} \begin{pmatrix} E'_h \\ E'_v \end{pmatrix} \quad (\text{Eq.149})$$

and

$$\begin{pmatrix} T_h^{Ant} \\ T_v^{Ant} \\ U_{hv}^{Ant} \\ V_{hv}^{Ant} \end{pmatrix} = \begin{pmatrix} \cos^2 \alpha' & \sin^2 \alpha' & -\cos \alpha' \sin \alpha' & 0 \\ \sin^2 \alpha' & \cos^2 \alpha' & \cos \alpha' \sin \alpha' & 0 \\ \sin 2\alpha' & -\sin 2\alpha' & \cos 2\alpha' & 0 \\ 0 & 0 & 0 & 1 \end{pmatrix} \begin{pmatrix} T_h \\ T_v \\ U \\ V \end{pmatrix} \quad (\text{Eq.150})$$

Considering both angles together we then have

$$\begin{pmatrix} E_h^{Ant} \\ E_v^{Ant} \end{pmatrix} = \begin{pmatrix} \cos(\alpha' + \Omega) & -\sin(\alpha' + \Omega) \\ \sin(\alpha' + \Omega) & \cos(\alpha' + \Omega) \end{pmatrix} \begin{pmatrix} E_h \\ E_v \end{pmatrix} \quad (\text{Eq.151})$$

And

$$\begin{pmatrix} T_h^{Ant} \\ T_v^{Ant} \\ U_{hv}^{Ant} \\ V_{hv}^{Ant} \end{pmatrix} = \begin{pmatrix} \cos^2(\alpha' + \Omega) & \sin^2(\alpha' + \Omega) & -\cos(\alpha' + \Omega) \sin(\alpha' + \Omega) & 0 \\ \sin^2(\alpha' + \Omega) & \cos^2(\alpha' + \Omega) & \cos(\alpha' + \Omega) \sin(\alpha' + \Omega) & 0 \\ \sin 2(\alpha' + \Omega) & -\sin 2(\alpha' + \Omega) & \cos 2(\alpha' + \Omega) & 0 \\ 0 & 0 & 0 & 1 \end{pmatrix} \begin{pmatrix} T_h^{TOA} \\ T_v^{TOA} \\ U_{hv}^{TOA} \\ V_{hv}^{TOA} \end{pmatrix} \quad (\text{Eq.152})$$

and we define the rotation matrix :

$$\Psi(\phi) = \begin{pmatrix} \cos^2(\alpha' + \Omega) & \sin^2(\alpha' + \Omega) & -\cos(\alpha' + \Omega) \sin(\alpha' + \Omega) & 0 \\ \sin^2(\alpha' + \Omega) & \cos^2(\alpha' + \Omega) & \cos(\alpha' + \Omega) \sin(\alpha' + \Omega) & 0 \\ \sin 2(\alpha' + \Omega) & -\sin 2(\alpha' + \Omega) & \cos 2(\alpha' + \Omega) & 0 \\ 0 & 0 & 0 & 1 \end{pmatrix} \quad (\text{Eq.153})$$

where $\phi = (\alpha' + \Omega)$.

8.8 Sum of contributions at the Top of the atmosphere and antenna pattern integration

Considering all components of the scene brightness temperature, the complete Radiative Transfer Model solution for T_p^{TOA} , in the surface polarization basis, is:

$$\begin{pmatrix} T_{th}^{TOA,RTM} \\ T_{tv}^{TOA,RTM} \\ U^{TOA,RTM} \\ V^{TOA,RTM} \end{pmatrix} = \begin{pmatrix} T_{atm}^{up} + (\tau_d \tau_v \tau_w \tau_I \tau_R) [T_{surf,h}^{tot} + R_{surf,h}^{tot} \cdot T_{atm}^{dw} + T_{sch} + T_{ssh}] \\ T_{atm}^{up} + (\tau_d \tau_v \tau_w \tau_I \tau_R) [T_{surf,v}^{tot} + R_{surf,v}^{tot} \cdot T_{atm}^{dw} + T_{scv} + T_{ssv}] \\ (\tau_d \tau_v \tau_w \tau_I \tau_R) T_{erU} \\ (\tau_d \tau_v \tau_w \tau_I \tau_R) T_{erV} \end{pmatrix} \quad (\text{Eq.154})$$

where

- T_{atm}^{up} and T_{atm}^{dw} are the unpolarized upwelling and downwelling brightness temperature of atmospheric 1-way emission which can be derived from (Eq.131) and (Eq.132),
- τ_d is the 1-way atmospheric transmittance associated with molecular oxygen absorption, determined from (Eq.127),
- τ_v is the 1-way atmospheric transmittance associated with water vapor absorption, determined from (Eq.127),
- τ_w is the 1-way atmospheric transmittance associated with cloud liquid water absorption, determined from (Eq.127),
- τ_I is the 1-way atmospheric transmittance associated with cloud ice absorption, determined from (Eq.127),
- $T_{surf,p}^{tot}$ and $R_{surf,p}^{tot}$, the p-pol brightness temperature, and reflectivity, of the total sea surface emission, including specular emission determined from (Eq.33) and (Eq.34), and the rough and foamy sea surface induced emission from (Eq. 36),
- T_{erU} and T_{erV} are the third and fourth Stokes brightness temperature of rough surface emission, respectively, determined in from (Eq.41)
- T_{scp} is the p-pol brightness temperature of scattered celestial sky radiation (not part of the present algorithm, see for L-band the L2SSS ATBD's dedicated [page](#)),
- T_{ssp} , is the p-pol brightness temperature of scattered solar radiation (sunglint), (not part of the present algorithm, see for L-band the L2SSS ATBD's dedicated [page](#)).

Note that in order to be able comparing CIMR data and the RTM solutions, one finally need to integrate over the CIMR antenna patterns:

$$T_{tp}^{TOA,RTM} = \frac{1}{4\pi} \int_{Earth} \mathbf{G}(\mathbf{b}) \Psi(\boldsymbol{\phi}) T_{tp}^{TOA,RTM} \frac{\partial\Omega}{\partial A} dA \quad (\text{Eq.155})$$

The integral is over the surface of the earth visible to the sensor, where the differential surface area is dA and $d\Omega$ is the differential solid angle. The ratio of the differential solid angle to the differential surface area is

$$\frac{\partial\Omega}{\partial A} = f_{lat} \frac{\cos\theta_s}{r^2} \quad (\text{Eq.156})$$

where θ_s is the incidence angle and r is the range. For a spherical Earth, the leading term f_{lat} would be unity. However, the Earth is modeled as an oblate spheroid and as a consequence this term is a function of latitude, deviating about $\pm 1\%$ from unity. The matrix $\mathbf{G}(\mathbf{b})$ is a 4×4 matrix describing the antenna gain function. Each element in this matrix is a function of the look direction \mathbf{b} which is the unit vector pointing from the antenna to dA . The term $\Psi(\phi)$ is the rotation matrix defined in previous section ([Eq.165](#)).

8.9 CIMR Leve1b re-sampling approach

We recommend the Backus-Gilbert (BG) Optimum Interpolation for the CIMR Leve1b re-sampling approach, which is an established and widely used method for sampling and gridding passive microwave satellite data ([Poe \[1990\]](#)). It finds a set of weights A_i in the neighborhood of a chosen synthetic target footprint and computes the antenna temperature T_A of the target $T_{A,rspl}$, as weighted sum of the individual observations $T_{A,i}$:

$$T_{A,rspl} = \sum_i A_i \cdot T_{A,i} \quad (\text{Eq.157})$$

The weights A_i are determined by minimizing the least square deviation of the fit:

$$Q = \iint [G_T(x, y) - \sum_i A_i \cdot G_i(x, y)]^2 dx dy \quad (\text{Eq.158})$$

between the chosen target response (gain) GT and the resampled gain. The index i runs over all samples in the neighborhood of the target cell that have a sufficiently large weight A_i to be included in the average $T_{A,rspl}$. One can include all samples within a 180 km radius of the target cell.

Carrying out this optimization requires the computation of the normalization integral:

$$u_i = \iint G_i(x, y) dx dy \quad (\text{Eq.159})$$

and the two overlap integrals

$$v_i = \iint G_T(x, y) \cdot G_i(x, y) dx dy \quad (\text{Eq.160})$$

$$g_{ij} = \iint G_T(x, y) \cdot G_i(x, y) + \beta \cdot \delta_{ij} dx dy \quad (\text{Eq.161})$$

The gain functions $G_i(x, y)$ of the individual CIMR observations are given by the pre-launch measured antenna patterns of the CIMR multi-frequency horns and are the individual CIMR gain patterns of the effective field of view (EFOV) of 36 x 64 km for L-band.

The result of the optimization can be summarized as follows (using vector/matrix notation, the superscript T denotes the transposed vector):

$$\mathbf{A} = \mathbf{g}^{-1} \cdot \left[\mathbf{v} + \frac{(1 - \mathbf{u}^T \cdot \mathbf{g}^{-1} \cdot \mathbf{v})}{\mathbf{u}^T \cdot \mathbf{g}^{-1} \cdot \mathbf{u}} \mathbf{u} \right] \quad (\text{Eq.162})$$

The parameter β is a small smoothing parameter. Its value is chosen to optimize the noise reduction factor $NRF = \sum_i A_i^2$ compared to the original gain pattern $g_i(x, y)$ in a tradeoff for the quality of fit Q . A smaller/larger value for β results in a better/worse fit value Q and in a worse/better NRF .

The values of the resampling weights A_i , the fit Q and the NRF depend all on the scanning geometry and the scan azimuth angle.

The target cells for the CIMR L2 SSS products at Moderate spatial Resolution are centered on the center points of a fixed 0.4° Earth grids whose vertices are located at $0^\circ, 0.4^\circ, 0.8^\circ, \dots$ longitude and at $0^\circ, \pm 0.4^\circ, \pm 0.80^\circ, \dots$, latitude. The target gain patterns g_i are the same as the original EFOV L-band footprints. For the smoothing factor β a value of 0.5 is chosen. This results in an average NRF of about 0.4.

The BG OI that can be applied in the CIMR L1B processing of the OVV retrieval algorithm can actually be done in two steps. The first step in the resampling is to take a single scan and adjustment the position of the observations to corresponds to integer azimuth angles (i.e. 0° to 359°). The sampling in the along-scan direction well exceeds Nyquist sampling, and therefore the fit accuracy of the resampled data shall be very high. The second step is the resampling onto the fixed $0.4^\circ \times 0.4^\circ$ grids.

8.10 Sea Surface Salinity inversion algorithm

To retrieve the surface salinity, we use a Bayesian inversion approach in which the posterior distribution of the retrieved SSS: ρ is taken to be the product of the likelihood function \mathcal{L} and prior distribution functions P and P' for wind speed, and SST, respectively:

$$\rho(\widetilde{SSS} | \mathbf{T}_{pi}; \sigma_u, u_{10}^p, \sigma_T, SST_p) = \mathcal{L}(\widetilde{u_{10}}, \widetilde{SST}, \widetilde{SSS}, \mathbf{T}_{pi}) \cdot P(\widetilde{u_{10}} | \sigma_u, u_{10}^p) \cdot P'(\widetilde{SST} | \sigma_T, SST_p) \quad (\text{Eq.163})$$

where

- ρ is the posterior distribution of the retrieved SSS,

- \mathcal{L} is a likelihood function,

- \mathbf{T}_{pi} are the input CIMR TOA L-band resampled Tbs, either:

$$\mathbf{T}_{pi} = [T_{h,L}^{TOA,fore}, T_{v,L}^{TOA,fore}, U_L^{TOA,fore}, V_L^{TOA,fore}] \text{ for the fore view, or,}$$

$$\mathbf{T}_p = [T_{h,L}^{TOA,aft}, T_{v,L}^{TOA,aft}, U_L^{TOA,aft}, V_L^{TOA,aft}] \text{ for the aft view,}$$

- P is the prior distribution of wind speed,

- P' is the prior distribution of SST,

- σ_u is the standard deviation of the prior wind speed

- σ_T is the standard deviation of the prior SST,

- T_{sp} is the prior SST,

- u_{10p} is the prior wind speed, and,

- ϕ_{wp} is the prior wind direction.

As discussed in Monahan et al. (2018), the bivariate Rice distribution for wind speed follows from assuming that the wind components have Gaussian and isotropic fluctuations. The prior distribution for wind speed can thus takes the form of a Rice distribution:

$$P(\tilde{u}_{10} | \sigma_u, u_{10p}) = \frac{\tilde{u}_{10}}{\sigma_u^2} \exp \left[-\frac{\tilde{u}_{10}^2 + u_{10p}^2}{2\sigma_u^2} \right] \cdot I_0 \left(\frac{\tilde{u}_{10} \cdot u_{10p}}{\sigma_u^2} \right) \quad (\text{Eq.164})$$

where I_0 is the modified Bessel function of the first kind with order zero.

For the prior distribution of SST, one can assume a gaussian distribution:

$$P'(\tilde{T}_s | \sigma_T, T_{sp}) = \frac{1}{2\pi\sigma_T^2} \exp \left[\frac{(\tilde{T}_s - T_{sp})^2}{2\sigma_T^2} \right] \quad (\text{Eq.165})$$

In fact, while SST display nonzero skewness and kurtosis (Sura, 2008), these non-Gaussian features are sufficiently modest that the specification of Gaussian fluctuations in SST is a reasonable first approximation.

Alternatively, these two distributions can also be set to $P = P' = \mathbf{1}$, to give zero impacts of priors on the end retrievals (see next section on algorithm performance assessment). Note that in practice for the test card inversion simulations, we indeed used such an approach and further assumed that $u_{10p}=7$ m/s, and $T_{sp}=15^\circ\text{C}$ are constant and uniform for all the scene. In an operational algorithm, u_{10p} and, T_{sp} can be derived from e.g., the CIMR retrieved L2 OWV and L2 SST, respectively. Alternatively, ECMWF forecast fields can be also used.

The likelihood function \mathcal{L} is computed using the previously described RTM, here represented by the geophysical model function G , and which can be evaluated using (Eq.154) and the input CIMR TOA Tbs T_{pi} :

$$\mathcal{L}(SSS, T_{pi}) = \prod_{i=0}^N \exp \left[\frac{-\left(T_{pi} - G(u_{10}, \tilde{T}_s, SSS, V, CLW, Tair, \dots)\right)_2}{2\sigma_{pi}^2} \right] \quad (\text{Eq.164})$$

where σ_{pi} is the standard deviation of the CIMR TOA Tbs. It can be first taken to be the respective NEDT of the L-band channel and can be re-evaluated post-launch using a large collected Tb TOA dataset.

The nominal Bayesian SSS solution is taken to be the Maximum likelihood estimate (mode of the posterior distribution), following:

$$SSS = \arg \max \varphi(\widetilde{SSS} | \mathbf{T}_p; \sigma_u, u_{10}^p, \sigma_T, SST_p) \quad (\text{Eq.165})$$

This non-linear problem is solved iteratively using a Levenberg-Marquardt (1963) algorithm to find the local maxima.

9. A Level-2 SSS retrieval prototype algorithm for CIMR

This notebook implements a prototype for a Level-2 SSS algorithm in python for the CIMR mission. We refer to the corresponding [ATBD](#) and especially the [Baseline Algorithm Definition](#).

In particular, the figure below illustrates the overall concept of the processing:

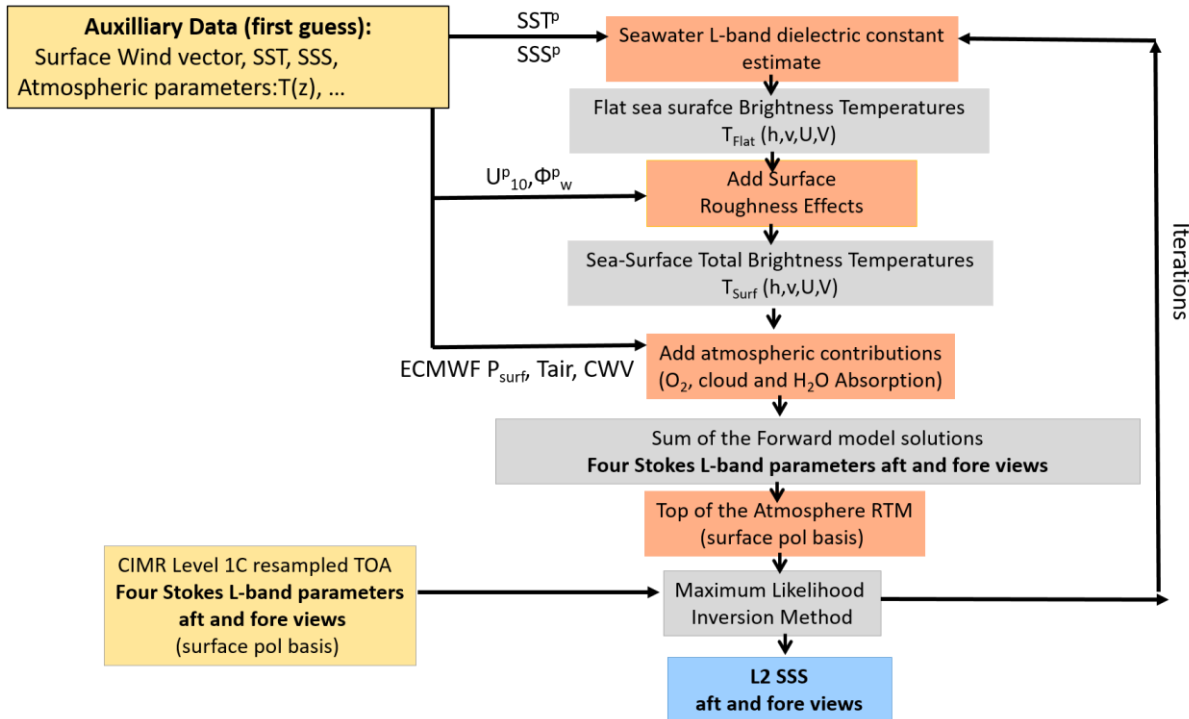


Figure 16: Level-2 SSS end to end algorithm functional flow diagram. Here,, , and are a priori values for the SST, SSS, 10 meter height surface wind speed and direction, respectively.

In what follows, we successively provide codes and running results for each component of the Algorithm:

9.1) Sea Water Dielectric Constant model at L-band

In this section we first provide the code for the dielectric constant model at L-band. Illustrative plots of the real & imaginary parts of $\epsilon_{sw}(S, T)$ as a function of Salinity (S) and Temperature (T) are then provided.

```

from importlib import reload

import sys
import os
import numpy as np
import xarray as xr
  
```

```

import cmath as cm
from math import *

from matplotlib import pylab as plt

#####
#
#      epsilon=cdiel_cimr_L(S,T)      [complex]
#
# Compute the complex dielectric constant of sea water
# as function of the following inputs:
#   -Salinity S [pss]
#   -Temperature T [K]
#
# at electromagnetic frequency f=1.4e9 [Hz] (L-band)
#
# The output epsilon
#   is a complex matrix of size=[Length(S),Length(T)]
#   and gives a value of epsilon for each value of S and T.
#   The model used is either Zhou et al. (2021) for L-band
#
# References:
#
# 1) Y. Zhou, R. H Lang, E.P. Dinnat, and
# D. M Le Vine. Seawater debye model function at L-band
# and its impact on salinity retrieval from aquarius
# satellite data. IEEE Transactions on Geoscience and
# Remote Sensing, 59(10):8103-8116, 2021.
#
#
# Code written by Reul. N. @Ifremer, March 2023
#####

def cdieL_cimr_L(S, T):

    T = T-273.15 # temperature in degree celsius [°C]

    # Input Parameters
    lS = np.size(S)                      #Length of vector S
    lT = np.size(T)                      #Length of vector T
    f = 1.4*1e9

    epsilon0 = 8.854e-12 #free-space permittivity.....[F/m]

    # Transformation of T and S into matrices [lSxLT]

    arr = np.array([S])
    repetitions = lT
    Sm = np.tile(arr,repetitions)
    arr = np.array([T])
    repetitions = lS
    Tm = np.tile(arr,repetitions)

#####
#####

```

```

# Zhou et al. [2021]'s Debye model (GW2020) for the seawater dielectric constant is used for
# the L-band channels (1.4 GHz) and is referred to as <>GW2020>>
#####
#####

# static dielectric constant of distilled water
eps_sdw = 88.0516 - 4.01796e-1 * Tm - 5.1027e-5 * Tm**2 + 2.55892e-5 * Tm**3
# relaxation time of distilled water:
tau = 1.75030e-11 - 6.12993e-13 * Tm + 1.24504e-14 * Tm**2 - 1.14927e-16 * Tm**3
# factor in the static dielectric constant of seawater due to the presence of ions
R_swdw = 1 - Sm * (3.97185e-3 - 2.49205e-5 * Tm - 4.27558e-5 * Sm + 3.92825e-7 * Sm * Tm + 4
.15350e-7 * Sm**2)
# conductivity of distilled water
sigma_fS0 = 9.50470e-2 * Sm - 4.30858e-4 * Sm**2 + 2.16182e-6 * Sm**3
R_sigma = 1 + Tm * (3.76017e-2 + 6.32830e-5 * Tm + 4.83420e-7 * Tm**2 - 3.97484e-4 * Sm +
6.26522e-6 * Sm**2)
# conductivity of sea water
sigma = sigma_fS0 * R_sigma
# dielectric constant of distilled water at infinite frequency
epsilon_inf = 4.9
# electromagnetic pulsation
omega = 2 * pi * f # * 1e-9 # f is in GHz
# dielectric constant of sea water
j = cm.sqrt(-1)
epsilon = epsilon_inf + ((eps_sdw * R_swdw - epsilon_inf) / (1 + j * omega * tau)) - ((j *
sigma) / (omega * epsilon_0))
epsilon = np.conj(epsilon)

return epsilon

```

In the following, the real and imaginary parts of the dielectric constant at **L-band** are plotted as a function of S and T

```

from importlib import reload

import sys
import os
import numpy as np
import xarray as xr
import cmath as cm
from math import *

from matplotlib import pylab as plt

#####
#####
# Plot the dielectric constant over S and T ranges at the CIMR L-band frequency      #
#####
#####

# Vectors of Sea Surface salinity So and Temperature To

```

```
So = np.arange(0, 40, 0.1)
To = 0+273.15
T1 = 5+273.15
T2 = 10+273.15
T3 = 15+273.15
T4 = 20+273.15
T5 = 25+273.15
T6 = 30+273.15

f = 1.4*1e9

test = cdiel_cimr_L(So, To)
real_epsilon_L0 = test.real
imag_epsilon_L0 = test.imag

test = cdiel_cimr_L(So, T1)
real_epsilon_L1 = test.real
imag_epsilon_L1 = test.imag

test = cdiel_cimr_L(So, T2)
real_epsilon_L2 = test.real
imag_epsilon_L2 = test.imag

test = cdiel_cimr_L(So, T3)
real_epsilon_L3 = test.real
imag_epsilon_L3 = test.imag

test = cdiel_cimr_L(So, T4)
real_epsilon_L4 = test.real
imag_epsilon_L4 = test.imag

test = cdiel_cimr_L(So, T5)
real_epsilon_L5 = test.real
imag_epsilon_L5 = test.imag

test = cdiel_cimr_L(So, T6)
real_epsilon_L6 = test.real
imag_epsilon_L6 = test.imag

fig0, ((ax1, ax2), (ax3, ax4)) = plt.subplots(2, 2, figsize=(10,10))
fig0.suptitle('Sea Water Dielectric Constant model at 1.4 GHz (L-band)', fontweight='bold', fontsize=15)
fig0.gca().tick_params(axis='both', which='major', labelsize=15)
ax1.plot(So,np.transpose(real_epsilon_L0), '--', linewidth=2)
ax1.plot(So,np.transpose(real_epsilon_L1), '--', linewidth=2)
ax1.plot(So,np.transpose(real_epsilon_L2), '--', linewidth=2)
ax1.plot(So,np.transpose(real_epsilon_L3), '--', linewidth=2)
ax1.plot(So,np.transpose(real_epsilon_L4), '--', linewidth=2)
ax1.plot(So,np.transpose(real_epsilon_L5), '--', linewidth=2)
ax1.plot(So,np.transpose(real_epsilon_L6), '--', linewidth=2)
# Set axis limits and labels
ax1.axis([0, 40, 65, 90])
ax1.set_xlabel('Sea Surface Salinity [psu]', fontsize=15)
```

```
ax1.set_ylabel('Real part($\u03B5$)', fontsize=15)
ax1.set_title('a)', fontsize=15)
ax1.set_xticks(np.arange(0, 40, 4))
#ax1.set_yticks(np.arange(68.5, 90, 2.5))
ax1.tick_params(axis='x', labelsize=15)
ax1.tick_params(axis='y', labelsize=15)
ax1.grid()
ax1.legend(['T=0°C', 'T=5°C', 'T=10°C', 'T=15°C', 'T=20°C', 'T=25°C', 'T=30°C'],
loc='best', fontsize=12)

ax2.plot(So,np.transpose(imag_epsilon_L0), '--', linewidth=2)
ax2.plot(So,np.transpose(imag_epsilon_L1), '--', linewidth=2)
ax2.plot(So,np.transpose(imag_epsilon_L2), '--', linewidth=2)
ax2.plot(So,np.transpose(imag_epsilon_L3), '--', linewidth=2)
ax2.plot(So,np.transpose(imag_epsilon_L4), '--', linewidth=2)
ax2.plot(So,np.transpose(imag_epsilon_L5), '--', linewidth=2)
ax2.plot(So,np.transpose(imag_epsilon_L6), '--', linewidth=2)
# Set axis limits and labels
ax2.axis([0, 40, 0, 100])
ax2.set_xlabel('Sea Surface Salinity [pss]', fontsize=15)
ax2.set_ylabel('Imaginary part($\u03B5$)', fontsize=15)
ax2.set_title('b)', fontsize=15)
ax2.set_xticks(np.arange(0, 40, 4))
ax2.tick_params(axis='x', labelsize=15)
ax2.tick_params(axis='y', labelsize=15)
ax2.grid()
ax2.legend(['T=0°C', 'T=5°C', 'T=10°C', 'T=15°C', 'T=20°C', 'T=25°C', 'T=30°C'],
loc='best', fontsize=12)

# Vectors of Sea Surface salinity So and Temperature To
To = np.arange(-2, 40, 0.1)+273.15
So = 10
S1 = 15
S2 = 20
S3 = 25
S4 = 30
S5 = 35
S6 = 40

test = cdiel_cimr_L(So, To)
real_epsilon_L7 = test.real
imag_epsilon_L7 = test.imag

test = cdiel_cimr_L(S1, To)
real_epsilon_L8 = test.real
imag_epsilon_L8 = test.imag

test = cdiel_cimr_L(S2, To)
real_epsilon_L9 = test.real
imag_epsilon_L9 = test.imag

test = cdiel_cimr_L(S3, To)
real_epsilon_L10 = test.real
imag_epsilon_L10 = test.imag
```

```
test = cdiel_cimr_L(S4, To)
real_epsilon_L11 = test.real
imag_epsilon_L11 = test.imag

test = cdiel_cimr_L(S5, To)
real_epsilon_L12 = test.real
imag_epsilon_L12 = test.imag

test = cdiel_cimr_L(S6, To)
real_epsilon_L13 = test.real
imag_epsilon_L13 = test.imag

ax3.plot(To-273.15,np.transpose(real_epsilon_L7), '--', linewidth=2)
ax3.plot(To-273.15,np.transpose(real_epsilon_L8), '--', linewidth=2)
ax3.plot(To-273.15,np.transpose(real_epsilon_L9), '--', linewidth=2)
ax3.plot(To-273.15,np.transpose(real_epsilon_L10), '--', linewidth=2)
ax3.plot(To-273.15,np.transpose(real_epsilon_L11), '--', linewidth=2)
ax3.plot(To-273.15,np.transpose(real_epsilon_L12), '--', linewidth=2)
ax3.plot(To-273.15,np.transpose(real_epsilon_L13), '--', linewidth=2)
# Set axis limits and labels
ax3.axis([-2, 32, 65, 90])
ax3.set_xlabel('Sea Surface Temperature [°C]', fontsize=15)
ax3.set_ylabel('Real part($\u03B5$)', fontsize=15)
ax3.set_title('c', fontsize=15)
ax3.set_xticks(np.arange(-2, 32, 4))
ax3.grid()
ax3.legend(['S=10', 'S=15', 'S=20', 'T=25', 'S=30', 'S=35', 'S=40'], loc='best', fontsize=12)
ax3.tick_params(axis='x', labelsize=15)
ax3.tick_params(axis='y', labelsize=15)

ax4.plot(To-273.15,np.transpose(imag_epsilon_L7), '--', linewidth=2)
ax4.plot(To-273.15,np.transpose(imag_epsilon_L8), '--', linewidth=2)
ax4.plot(To-273.15,np.transpose(imag_epsilon_L9), '--', linewidth=2)
ax4.plot(To-273.15,np.transpose(imag_epsilon_L10), '--', linewidth=2)
ax4.plot(To-273.15,np.transpose(imag_epsilon_L11), '--', linewidth=2)
ax4.plot(To-273.15,np.transpose(imag_epsilon_L12), '--', linewidth=2)
ax4.plot(To-273.15,np.transpose(imag_epsilon_L13), '--', linewidth=2)
# Set axis limits and labels
ax4.axis([-2, 32, 0, 100])
ax4.set_xlabel('Sea Surface Temperature [°C]', fontsize=15)
ax4.set_ylabel('Imaginary part($\u03B5$)', fontsize=15)
ax4.set_title('d', fontsize=15)
ax4.set_xticks(np.arange(-2, 32, 4))
ax4.tick_params(axis='x', labelsize=15)
ax4.tick_params(axis='y', labelsize=15)
ax4.grid()
ax4.legend(['S=10', 'S=15', 'S=20', 'T=25', 'S=30', 'S=35', 'S=40'], loc='best', fontsize=12)
# set the spacing between subplots
# set the spacing between subplots
plt.subplots_adjust(left=0.1,
```

```

    bottom=0.1,
    right=0.9,
    top=0.9,
    wspace=0.3,
    hspace=0.4)
plt.show()

```

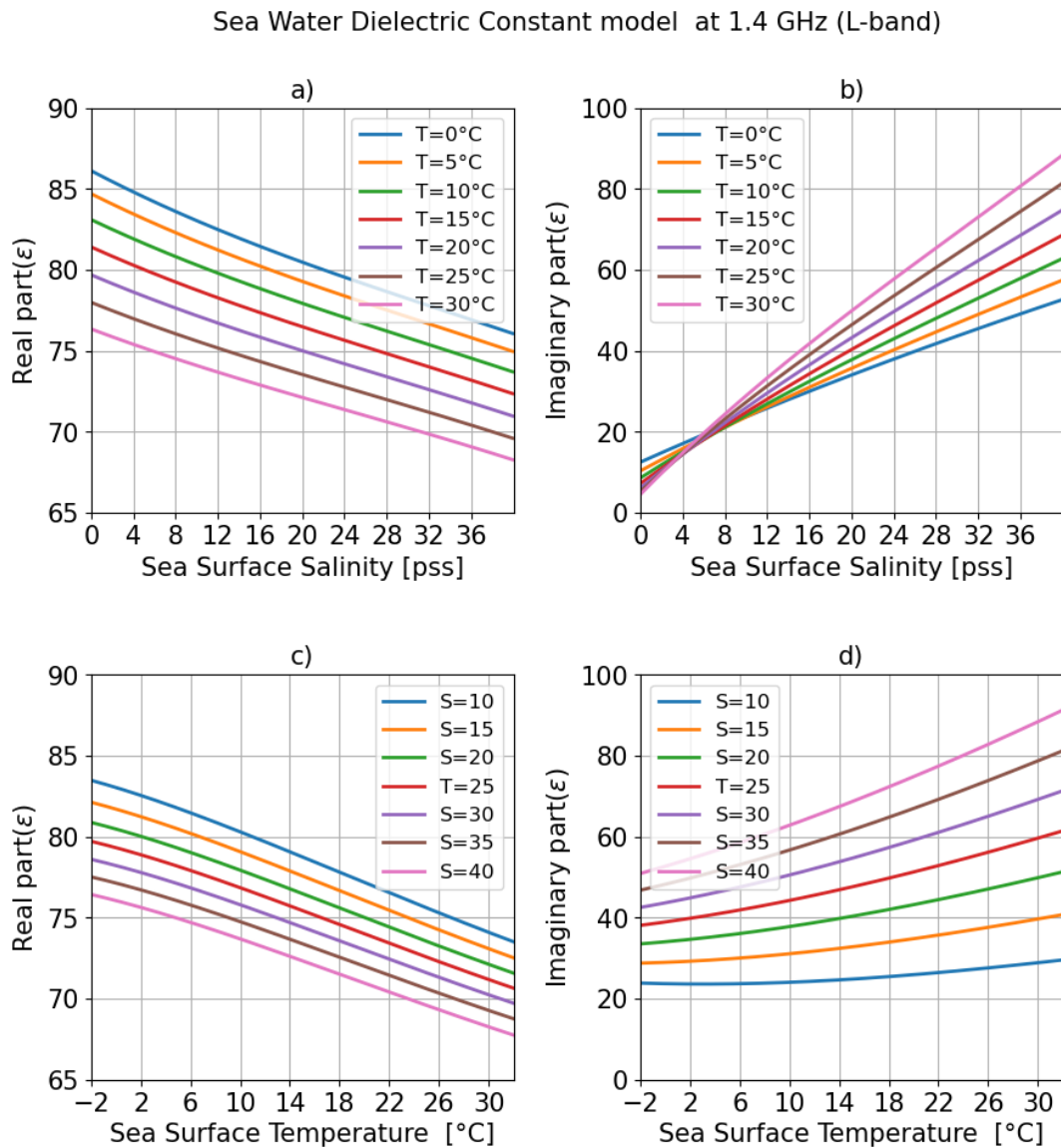


Figure 17: Real (a,c) and Imaginary (b,d) parts of the Sea water Dielectric Constant model of Zhou et al. (2021) at L-band as a function of sea water salinity (a,b) and Temperature (c,d).

9.2) Brightness Temperature of a perfectly flat Sea Surface

Here we provide the codes to evaluate the Brightness temperature emitted by a perfectly flat sea surface

```
from importlib import reload
```

```
import sys
import os
import numpy as np
import xarray as xr
import cmath as cm
from math import *

from matplotlib import pylab as plt

#####
#          specular_sea_emission(S, T, theta, f)      [real]
#
# Compute the brightness temperature of a
# perfectly flat sea water surface with the following
# inputs:
#
# -Sea water surface Salinity S [pss]
# -Sea water Surface Temperature T [degree Kelvin]
#
# as observed by a radiometer at
#
# -Earth incidence angle theta [rad]
#
# and operated at
#
# -electromagnetic frequency f [Hz]
#
# The outputs are:
#
# T_spec_v: the perfectly flat sea surface brightness
#             temperature in V-polarization [Kelvins]
#
# T_spec_h: the perfectly flat sea surface brightness
#             temperature in H-polarization [Kelvin]
#
# References:
#
# Peake, William. Interaction of electromagnetic waves
# with some natural surfaces. IRE Transactions on Antennas
# and Propagation 7.5 (1959): 324-329.
#
# Nb: This code uses the subfunction cdiel_cimr which
# evaluates the complex sea water dielectric constant
# for salinity S, temperature T and electromagnetic
# frequency f.
#
# Code written by Reul. N. @Ifremer, March 2023
#
#####

def specular_sea_emission(S, T, theta, f):
```

```

# 1) Evaluate the complex sea water dielectric constant
#   for salinity S, temperature T and electromagnetic
#   frequency f.
if f < 2*1e9 :
    epsilon = cdiel_cimr_L(S, T)
else :
    epsilon = cdiel_cimr(S, T, f*1e-9)

i = 1j
# 2) Evaluate the Fresnel Reflection coefficients in H and V polarizations
from sea water dielectric constant
#   epsilon [complex] and radiometer incidence angle theta [rad]

Rh = (np.cos(theta) - np.sqrt(epsilon - np.sin(theta) ** 2)) / (np.cos(theta) + np.sqrt(epsilon - np.sin(theta) ** 2))
Rv = (epsilon * np.cos(theta) - np.sqrt(epsilon - np.sin(theta) ** 2)) / (epsilon * np.cos(theta) + np.sqrt(epsilon - np.sin(theta) ** 2))

# 2) Evaluate the the brightness temperature of a perfectly flat sea water
in vertical (v) and horizontal (h) polarization

T_spec_v = T * (1 - np.abs(Rv) ** 2)
T_spec_h = T * (1 - np.abs(Rh) ** 2)

return T_spec_v, T_spec_h

```

In the following, we plot the **perfectly flat sea surface brightness temperature emitted at L-band** as a function of S and T, and at EIA=51.9°

```

from importlib import reload

import sys
import os
import numpy as np
import xarray as xr
import cmath as cm
from math import *

from matplotlib import pylab as plt

#####
# Plot the dielectric constant over S and T ranges at the CIMR Ka-band frequency      #
#####
#####                                     # Vectors of Sea Surface salinity So and Temperature To [K]
So = np.arange(0, 40, 0.1)
To = 0+273.15
T1 = 5+273.15
T2 = 10+273.15
T3 = 15+273.15

```

```

T4 = 20+273.15
T5 = 25+273.15
T6 = 30+273.15

fL=1.4e9
thetaL=51.9 * np.pi/180

[T_spec_vo, T_spec_ho]=specular_sea_emission(So, To, thetaL, fL)
[T_spec_v1, T_spec_h1]=specular_sea_emission(So, T1, thetaL, fL)
[T_spec_v2, T_spec_h2]=specular_sea_emission(So, T2, thetaL, fL)
[T_spec_v3, T_spec_h3]=specular_sea_emission(So, T3, thetaL, fL)
[T_spec_v4, T_spec_h4]=specular_sea_emission(So, T4, thetaL, fL)
[T_spec_v5, T_spec_h5]=specular_sea_emission(So, T5, thetaL, fL)
[T_spec_v6, T_spec_h6]=specular_sea_emission(So, T6, thetaL, fL)

fig1, ((ax1, ax2), (ax3, ax4)) = plt.subplots(2, 2, figsize=(10,10))
fig1.suptitle('Brightness Temperature of a Perfectly Flat Ocean at 1.4 GHz  
(L-band) at EIA $\u03b8B$=51.9°, fontsize=15)
fig1.gca().tick_params(axis='both', which='major', labelsize=15)
ax1.plot(So,T_spec_vo[0,:], '--', linewidth=2)
ax1.plot(So,T_spec_v1[0,:], '--', linewidth=2)
ax1.plot(So,T_spec_v2[0,:], '--', linewidth=2)
ax1.plot(So,T_spec_v3[0,:], '--', linewidth=2)
ax1.plot(So,T_spec_v4[0,:], '--', linewidth=2)
ax1.plot(So,T_spec_v5[0,:], '--', linewidth=2)
ax1.plot(So,T_spec_v6[0,:], '--', linewidth=2)
# Set axis limits and labels
ax1.axis([0, 40, 125, 160])
ax1.set_xlabel('Sea Surface Salinity [pss]', fontsize=15)
ax1.set_ylabel('Brightness Temperature $T_{\{B\}}$ [K]', fontsize=15)
ax1.set_title('a) V-pol', fontsize=15)
ax1.set_xticks(np.arange(0, 40, 4))
#ax1.set_yticks(np.arange(30, 70, 5))
ax1.grid()
ax1.legend(['T=0°C', 'T=5°C', 'T=10°C', 'T=15°C', 'T=20°C', 'T=25°C', 'T=30°C'],
loc='best', fontsize=12)

ax2.plot(So,T_spec_ho[0,:], '--', linewidth=2)
ax2.plot(So,T_spec_h1[0,:], '--', linewidth=2)
ax2.plot(So,T_spec_h2[0,:], '--', linewidth=2)
ax2.plot(So,T_spec_h3[0,:], '--', linewidth=2)
ax2.plot(So,T_spec_h4[0,:], '--', linewidth=2)
ax2.plot(So,T_spec_h5[0,:], '--', linewidth=2)
ax2.plot(So,T_spec_h6[0,:], '--', linewidth=2)
# Set axis limits and labels
ax2.axis([0, 40, 55, 77.5])
ax2.set_xticks(np.arange(0, 40, 4))
ax2.set_xlabel('Sea Surface Salinity [pss]', fontsize=15)
ax2.set_ylabel('Brightness Temperature $T_{\{B\}}$ [K]', fontsize=15)
ax2.set_title('b) H-pol', fontsize=15)
ax2.grid()
ax2.legend(['T=0°C', 'T=5°C', 'T=10°C', 'T=15°C', 'T=20°C', 'T=25°C', 'T=30°C'],
loc='best', fontsize=12)

```

```
loc='best', fontsize=12)

# Vectors of Sea Surface salinity So and Temperature To
To = np.arange(-2, 40, 0.1)+273.15
So = 10
S1 = 15
S2 = 20
S3 = 25
S4 = 30
S5 = 35
S6 = 40

[T_spec_v7, T_spec_h7]=specular_sea_emission(So, To, thetaL, fL)
[T_spec_v8, T_spec_h8]=specular_sea_emission(S1, To, thetaL, fL)
[T_spec_v9, T_spec_h9]=specular_sea_emission(S2, To, thetaL, fL)
[T_spec_v10, T_spec_h10]=specular_sea_emission(S3, To, thetaL, fL)
[T_spec_v11, T_spec_h11]=specular_sea_emission(S4, To, thetaL, fL)
[T_spec_v12, T_spec_h12]=specular_sea_emission(S5, To, thetaL, fL)
[T_spec_v13, T_spec_h13]=specular_sea_emission(S6, To, thetaL, fL)

ax3.plot(To-273.15,T_spec_v7[0,:], '--', linewidth=2)
ax3.plot(To-273.15,T_spec_v8[0,:], '--', linewidth=2)
ax3.plot(To-273.15,T_spec_v9[0,:], '--', linewidth=2)
ax3.plot(To-273.15,T_spec_v10[0,:], '--', linewidth=2)
ax3.plot(To-273.15,T_spec_v11[0,:], '--', linewidth=2)
ax3.plot(To-273.15,T_spec_v12[0,:], '--', linewidth=2)
ax3.plot(To-273.15,T_spec_v13[0,:], '--', linewidth=2)
# Set axis limits and labels
ax3.axis([-2, 32, 125, 165])
ax3.set_xlabel('Sea Surface Temperature [°C]', fontsize=15)
ax3.set_ylabel('Brightness Temperature $T_{\{B\}}$ [K]', fontsize=15)
ax3.set_title('c) V-pol', fontsize=15)
ax3.set_xticks(np.arange(-2, 32, 4))
ax3.grid()
ax3.legend(['S=10', 'S=15', 'S=20', 'T=25', 'S=30', 'S=35', 'S=40'], loc='best', fontsize=12)
ax3.tick_params(axis='x', labelsize=15)
ax3.tick_params(axis='y', labelsize=15)

ax4.plot(To-273.15,T_spec_h7[0,:], '--', linewidth=2)
ax4.plot(To-273.15,T_spec_h8[0,:], '--', linewidth=2)
ax4.plot(To-273.15,T_spec_h9[0,:], '--', linewidth=2)
ax4.plot(To-273.15,T_spec_h10[0,:], '--', linewidth=2)
ax4.plot(To-273.15,T_spec_h11[0,:], '--', linewidth=2)
ax4.plot(To-273.15,T_spec_h12[0,:], '--', linewidth=2)
ax4.plot(To-273.15,T_spec_h13[0,:], '--', linewidth=2)
# Set axis limits and labels
ax4.axis([-2, 32, 55, 77.5])
ax4.set_xlabel('Sea Surface Temperature [°C]', fontsize=15)
ax4.set_ylabel('Brightness Temperature $T_{\{B\}}$ [K]', fontsize=15)
ax4.set_title('d) H-pol', fontsize=15)
ax4.set_xticks(np.arange(-2, 32, 4))
```

```
ax4.grid()
ax4.tick_params(axis='x', labelsize=15)
ax4.tick_params(axis='y', labelsize=15)
ax4.legend(['S=10', 'S=15', 'S=20', 'T=25', 'S=30', 'S=35', 'S=40'], loc='best', fontsize=12)

# set the spacing between subplots
plt.subplots_adjust(left=0.1,
                    bottom=0.1,
                    right=0.9,
                    top=0.9,
                    wspace=0.3,
                    hspace=0.4)
plt.show()
```

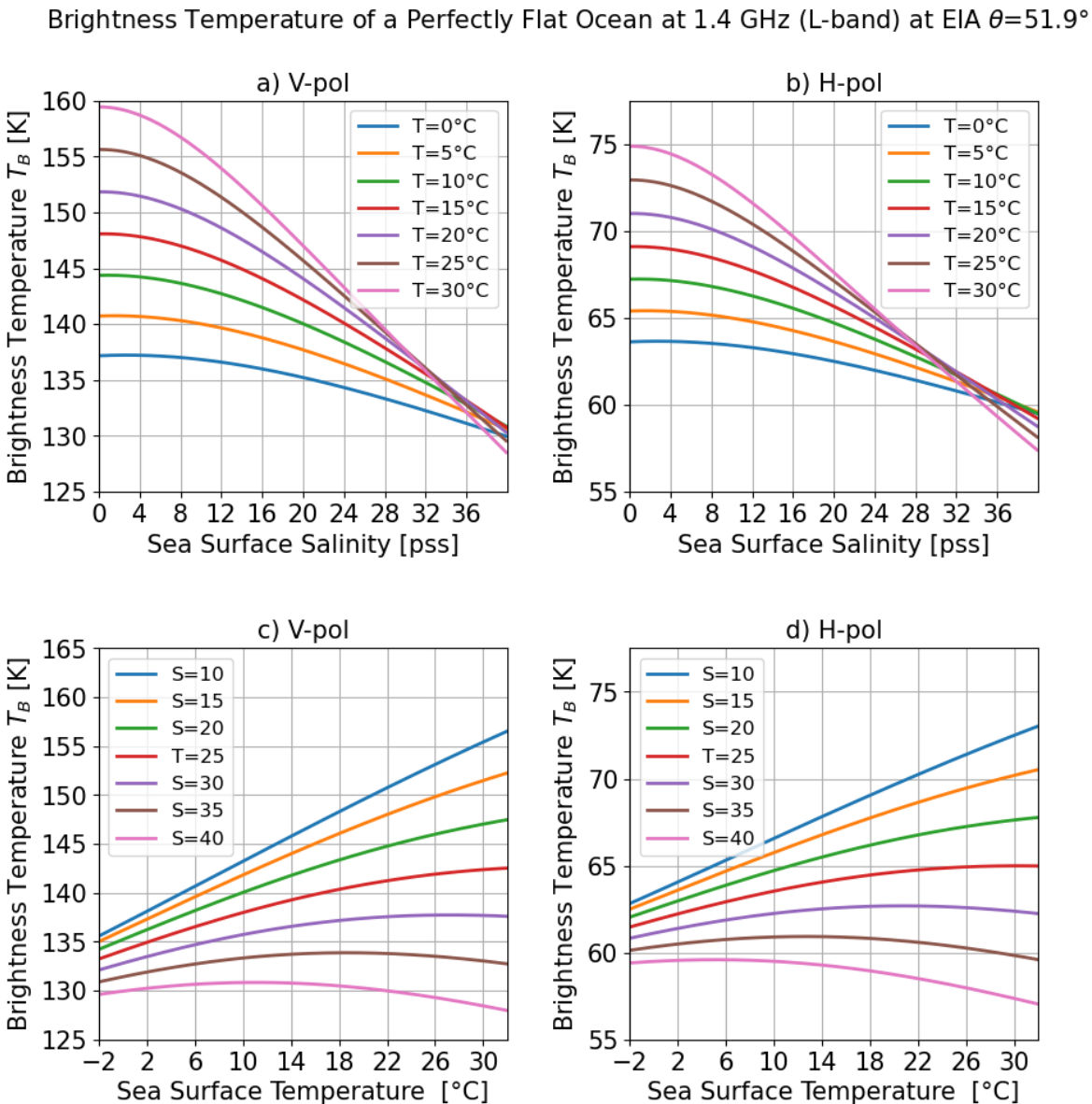


Figure 18: Perfectly flat sea surface brightness temperature emitted at L-band as a function of sea water salinity (a,b) and Temperature (c,d) for V-polarization (a,c) and H-polarization (b,d). EIA = 51.9°

9.3) Sea Surface Roughness-Induced Brightness temperature

The codes to evaluate the isotropic and anisotropic components of roughness(wind)-induced Brightness Temperature contrast for all 4 Stokes parameters at L-band are provided herebelow. Illustration are also given.

9.3.1) Isotropic components of the wind-induced radio-brightness contrast T_B

```
from importlib import reload
import numpy
import sys
import os
import numpy as np
import xarray as xr
import cmath as cm
```

```
import matplotlib.pyplot as plt
from math import *
from matplotlib import pylab as plt
import scipy.io

#####
# This code evaluate & plot the low-to-moderate wind speed (0-17 m/s) wind-induced emissivity azimuthal harmonic components using the CIMR's GMFS expressed in          #
# https://cimr-algos.github.io/OceanWindVectors_ATBD/baseline_algorithm_definition.html #
# for the CIMR L-band central frequency                                     #
#
#
#           Code written by Reul.N      nicolas.reul@ifremer.fr
#
#
#
#           April 2023
#
#
#####

#####
# 1) 10 meter height Wind speed Vector from 0 to 25 m/s      #
#####
#   Input Parameters
U10 = np.arange(0, 25.1, 0.1)

phi_r_deg = np.arange(0, 360, 10)
phi_r_rad = phi_r_deg * numpy.pi /180

lU = np.size(U10)                                     #Length of vector U10
lphi = np.size(phi_r_rad)                            #Length of vector phi_r

#   Transformation of U10 and phi_r into matrices [lUxLphi]

U10m = np.zeros((lU, lphi))
cosphim = np.zeros((lU, lphi))
cos2phim = np.zeros((lU, lphi))
sinphim = np.zeros((lU, lphi))
sin2phim = np.zeros((lU, lphi))

for i in range(lphi):
    U10m[:,i] = U10

for i in range(lU):
    cosphim[i,:] = np.cos(phi_r_rad)
    cos2phim[i,:] = np.cos(2 * phi_r_rad)
    sinphim[i,:] = np.sin(phi_r_rad)
    sin2phim[i,:] = np.sin(2 * phi_r_rad)
```

```
#####
#####
# 2) Isotropic wind-induced emissivity component at the 5 CIMR frequencies #
#####
#####
```

L-band isotropic coefficients (from table 3 in the ATBD)

```
delta_14v = [1.6097e-3, -2.6751e-4, 2.4483e-5, -8.6502e-7, 1.0749e-8]
delta_14h = [4.3588e-3, -5.8672e-4, 4.3997e-5, -1.4223e-6, 1.6548e-8]

Delta_e0_L_v = delta_14v[0] * U10 + delta_14v[1] * U10**2 + delta_14v[2] *
U10**3 + delta_14v[3] * U10**4 + delta_14v[4] * U10**5
Delta_e0_L_h = delta_14h[0] * U10 + delta_14h[1] * U10**2 + delta_14h[2] *
U10**3 + delta_14h[3] * U10**4 + delta_14h[4] * U10**5
```

Here below, we provide a code to plot the isotropic wind-induced emissivity H and V components

```
#####
#####
```

```
# Create a figure for the H-pol isotropic wind-induced emissivity @L-band
#####
fig1, ((ax1), (ax2)) = plt.subplots(1, 2, figsize=(10,5))

fig1.suptitle('Isotropic Wind-Induced Brightness Temperature at L-band')

fig1.gca().tick_params(axis='both', which='major', labelsize=15)

h1, = ax1.plot(U10, 290 * Delta_e0_L_h, '-', linewidth=2, color=[0.49, 0.18, 0.56])

ax1.axis([0, 25, 0, 12])

ax1.set_xlabel('10-meter height Wind Speed $U_{10}$ [m/s]', fontsize=12)

ax1.set_ylabel('Isotropic Wind Induced Emissivity $\u0394 E_{W0} \times [290 K]', fontsize=12)

ax1.set_title('a) H-pol')

ax1.set_xticks(np.arange(0, 25, 2))

#ax1.set_yticks(np.arange(-2, 26, 2))

ax1.set_yticks(np.arange(0, 12, 1))

ax1.grid()

ax1.axhline(0, linestyle='--', color='k', linewidth=2)
```

```
ax1.legend([h1], loc='best')

#####
##### # Create a figure for the V-pol isotropic wind-induced emissivity component at L-band #####
#####

h1, = ax2.plot(U10, 290 * Delta_e0_L_v, '- ', linewidth=2, color=[0.49, 0.18, 0.56])

# Set axis limits and labels
ax2.axis([0, 25, 0, 12])
ax2.set_xlabel('10-meter height Wind Speed $U_{10}$ [m/s]', fontsize=12)
ax2.set_ylabel('Isotropic Wind Induced Emissivity $\u0394 E_{W0} \times [290 K]', fontsize=12)
ax2.set_title('b) V-pol')
ax2.set_xticks(np.arange(0, 25, 2))
#ax2.set_yticks(np.arange(-2, 26, 2))
ax2.set_yticks(np.arange(0, 12, 1))
ax2.grid()
ax2.axhline(0, linestyle='--', color='k', linewidth=2)
ax2.legend([h1, h2, h3, h4, h5],
           ['CIMR L-band GMF at $\u03b8_{ref}=51.95^\circ'], loc='best', fontsize=12)
ax2.tick_params(axis='x', labelsize=11)
ax2.tick_params(axis='y', labelsize=11)
fig1.tight_layout()

# set the spacing between subplots
plt.subplots_adjust(left=0.1,
                    bottom=0.1,
                    right=0.9,
                    top=0.9,
                    wspace=0.3,
                    hspace=0.4)

plt.show()
```

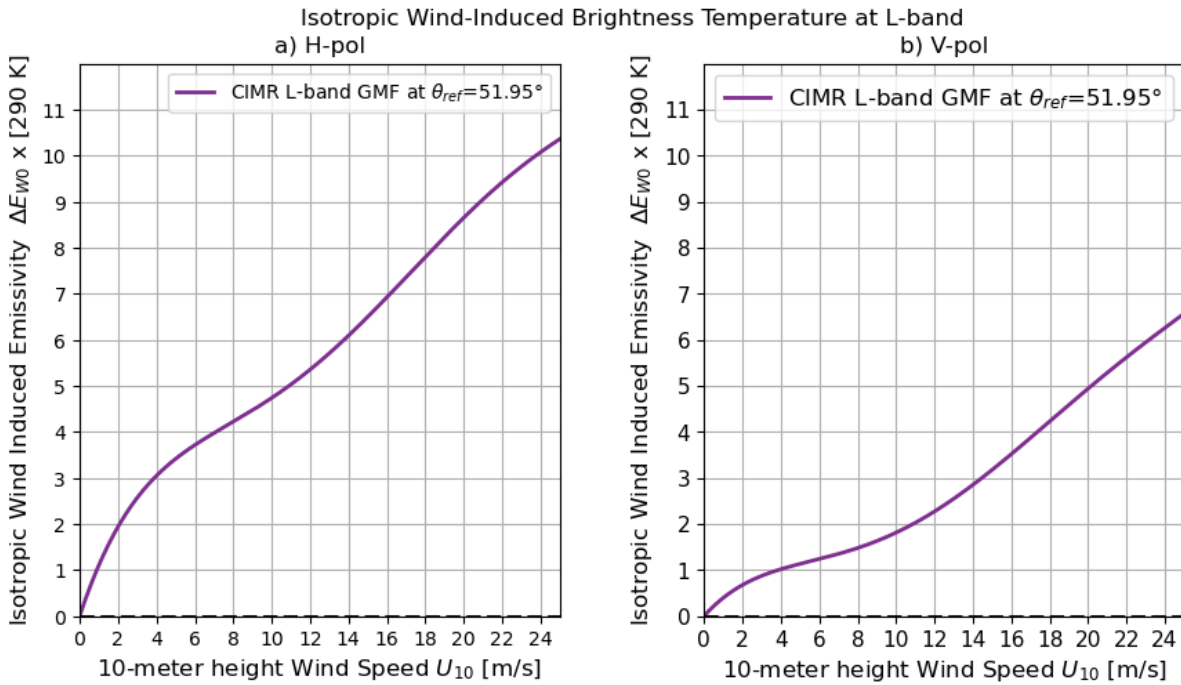


Figure 19 Isotropic wind induced T_B at L-band for (a) H-polarization and (b) V-polarization. The GMF are for the CIMR L-band horn nominal incidence angle of $\theta_{ref}=51.95^\circ$ and the SST is assumed to be equal to 290 K.

9.3.2) Anisotropic components of the wind-induced Radio-Brightness Contrast T_B

```
#####
# 3) Anisotropic wind-induced emissivity components #
#####

# 3.1) Coefficients for L-band
#####

# 3.1.1) First azimuthal harmonic coefficients at L-band
#####

a1L_V = np.array([9.1197181127e-3/290, -3.0431623312e-3/290, 5.0839571367e
-4/290, -2.0375986729e-5/290, 2.4580823525e-7/290]) # V-pol
a1L_H = np.array([9.6160121528e-3/290, -4.3505334225e-3/290, 6.0718079191e
-4/290, -2.7536464802e-5/290, 4.0733177632e-7/290]) # H-pol
U1L = np.array([2.1437e-05, 1.8411e-06, -1.044e-06, 4.3478e-08, -5.3051e-1
0]) # Third Stokes
V1L = np.array([-1.3375e-05, 5.3239e-06, -6.5753e-07, 4.2225e-08, -8.0259e
-10]) # Fourth Stokes

# 3.1.2) Second azimuthal harmonic coefficients at L-band
#####

a2L_V = np.array([9.3408423686e-002/290, -3.3492931571e-002/290, 3.8025601
```

```

997e-003/290, -1.6925890570e-004/290, 2.6396519557e-006/290]) # V-pol
a2L_H = np.array([-5.1974877527e-003/290, 1.0855313411e-002/290, -1.841173
5248e-003/290, 9.5714130699e-005/290, -1.6059448322e-006/290]) # H-pol
U2L = np.array([-6.5015e-05, 4.6888e-05, -7.2679e-06, 3.5813e-07, -5.7833e
-09]) # Third Stokes
V2L = np.array([-3.4803E-04, 1.5574E-04, -2.0192E-05, 9.3006E-07, -1.4414E
-08]) # Fourth Stokes

# 3.6) First azimuthal harmonic emissivity components
#####
# First azimuthal harmonic Components at L-band

Delta_e1_L_V = a1L_V[0] * U10m + a1L_V[1] * U10m**2 + a1L_V[2] * U10m**3 +
a1L_V[3] * U10m**4 + a1L_V[4] * U10m**5 # V-pol
Delta_e1_L_H = a1L_H[0] * U10m + a1L_H[1] * U10m**2 + a1L_H[2] * U10m**3 +
a1L_H[3] * U10m**4 + a1L_H[4] * U10m**5 # H-pol
Delta_U1_L = U1L[0] * U10m + U1L[1] * U10m**2 + U1L[2] * U10m**3 + U1L[3]
] * U10m**4 + U1L[4] * U10m**5 # Third Stokes
Delta_V1_L = V1L[0] * U10m + V1L[1] * U10m**2 + V1L[2] * U10m**3 + V1L[3]
] * U10m**4 + V1L[4] * U10m**5 # Fourth Stokes

# 3.7) Second azimuthal harmonic emissivity components
#####
#Second azimuthal harmonic Components at L-band
Delta_e2_L_V = a2L_V[0] * U10m + a2L_V[1] * U10m**2 + a2L_V[2] * U10m**3 +
a2L_V[3] * U10m**4 + a2L_V[4] * U10m**5 # V-pol
Delta_e2_L_H = a2L_H[0] * U10m + a2L_H[1] * U10m**2 + a2L_H[2] * U10m**3 +
a2L_H[3] * U10m**4 + a2L_H[4] * U10m**5 # H-pol
Delta_U2_L = U2L[0] * U10m + U2L[1] * U10m**2 + U2L[2] * U10m**3 + U2L[3]
* U10m**4 + U2L[4] * U10m**5 # Third Stokes
Delta_V2_L = V2L[0] * U10m + V2L[1] * U10m**2 + V2L[2] * U10m**3 + V2L[3]
* U10m**4 + V2L[4] * U10m**5 # Fourth Stokes

# Evaluate the wind direction-dependent emissivity components at each frequency and polarization

Delta_E_phi_L_h = Delta_e1_L_H * cosphim+Delta_e2_L_H * cos2phim
Delta_E_phi_L_v = Delta_e1_L_V * cosphim+Delta_e2_L_V * cos2phim
Delta_E_phi_L_3 = Delta_U1_L * sinphim+Delta_U2_L * sin2phim
Delta_E_phi_L_4 = Delta_V1_L * sinphim+Delta_V2_L * sin2phim

Plot the relative wind direction-dependent emissivity components at L-band and all Four Stokes components

# Plot the relative wind direction-dependent emissivity components at L-band and all Four Stokes components

fig1, ((ax1, ax2), (ax3, ax4)) = plt.subplots(2, 2, figsize=(10,10))
fig1.suptitle('Relative Wind Direction Dependence at 1.4 GHz (L-band)')

```

```
fig1.gca().tick_params(axis='both', which='major', labelsize=15)
ax1.plot(phi_r_deg, 290 * Delta_E_phi_L_h[51,:], '--', linewidth=2)
ax1.plot(phi_r_deg, 290 * Delta_E_phi_L_h[101,:], '--', linewidth=2)
ax1.plot(phi_r_deg, 290 * Delta_E_phi_L_h[151,:], '--', linewidth=2)
ax1.grid()
ax1.set_title("a) h-pol")
ax1.set_ylabel('$\Delta E_{\phi} \times [290 K]')
ax1.axis([0, 360, -3, 3])
ax1.set_xlabel('Relative Wind Direction [°]')
ax1.set_xticks(np.arange(0, 360, 45))
ax1.set_yticks(np.arange(-3, 3, .5))
ax1.legend(['$U_{10}=5 m/s', '$U_{10}=10 m/s', '$U_{10}=15 m/s'], loc='best')
ax2.plot(phi_r_deg, 290 * Delta_E_phi_L_v[51,:], '--', linewidth=2)
ax2.plot(phi_r_deg, 290 * Delta_E_phi_L_v[101,:], '--', linewidth=2)
ax2.plot(phi_r_deg, 290 * Delta_E_phi_L_v[151,:], '--', linewidth=2)
ax2.grid()
ax2.set_title("b) v-pol")
ax2.set_ylabel('$\Delta E_{\phi} \times [290 K]')
ax2.axis([0, 360, -3, 3])
ax2.set_xlabel('Relative Wind Direction [°]')
ax2.set_xticks(np.arange(0, 360, 45))
ax2.set_yticks(np.arange(-3, 3, .5))
ax3.plot(phi_r_deg, 290 * Delta_E_phi_L_3[51,:], '--', linewidth=2)
ax3.plot(phi_r_deg, 290 * Delta_E_phi_L_3[101,:], '--', linewidth=2)
ax3.plot(phi_r_deg, 290 * Delta_E_phi_L_3[151,:], '--', linewidth=2)
ax3.grid()
ax3.set_title("c) Third Stokes")
ax3.set_ylabel('$\Delta E_{\phi} \times [290 K]')
ax3.axis([0, 360, -3, 3])
ax3.set_xlabel('Relative Wind Direction [°]')
ax3.set_xticks(np.arange(0, 360, 45))
ax3.set_yticks(np.arange(-3, 3, .5))
ax4.plot(phi_r_deg, 290 * Delta_E_phi_L_4[51,:], '--', linewidth=2)
ax4.plot(phi_r_deg, 290 * Delta_E_phi_L_4[101,:], '--', linewidth=2)
ax4.plot(phi_r_deg, 290 * Delta_E_phi_L_4[151,:], '--', linewidth=2)
ax4.grid()
ax4.set_title("d) Fourth Stokes")
ax4.set_ylabel('$\Delta E_{\phi} \times [290 K]')
ax4.axis([0, 360, -3, 3])
ax4.set_yticks(np.arange(-3, 3, .5))
ax4.set_xlabel('Relative Wind Direction [°]')
ax4.set_xticks(np.arange(0, 360, 45))
ax4.tick_params(axis='x', labelsize=10)
ax4.tick_params(axis='y', labelsize=10)
```

Relative Wind Direction Dependence at 1.4 GHz (L-band)

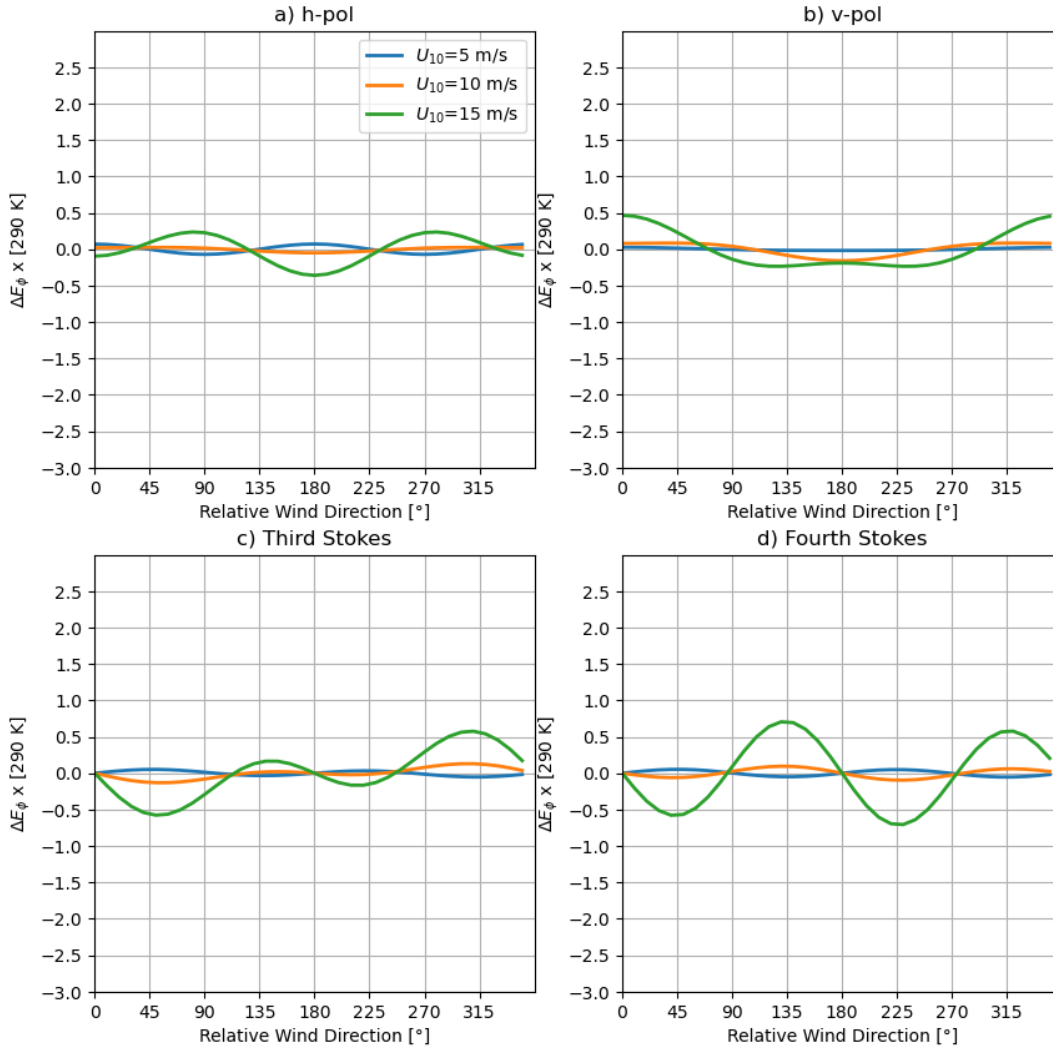


Figure 20: Anisotropic wind induced T_B at L-band for (a) H-polarization, (b) V-polarization, (c) Third Stokes and (d) Fourth Stokes parameters. The GMF are for the CIMR L-band horn nominal incidence angle of $\theta_{ref}=51.95^\circ$. The x-axis is the relative direction between the wind and the radiometer. The SST is assumed to be equal to 290 K

9.4) Atmospheric Contributions

In what follows, we first provide codes to successively evaluate the indices of refraction owing to dry air, water vapor, cloud liquid water, cloud ice, and rain

9.4.1) complex index of atmospheric refraction owing to dry air (molecular oxygen)

```

import numpy as np
import matplotlib.pyplot as plt
import scipy.io

#####
# This subfunction is part of the millimeter-wave propagation model (MPM93)

```

```
) software      #
# package and computes the complex index of refraction
#
# owing to dry air (molecular oxygen).
#
#
#                                     ND=mpm_dry(freq, e, pd, Tr)
#
#
#                                     #
#
#
# Outputs
#
#-----
#
# ND: index of refraction owing to dry air (molecular oxygen):
#
#
#
# Inputs:
#
#-----
#
# freq: Electromagnetic frequency          [GHz]
#
# e:    Partial pressure of the water vapour [hPa]
#
# pd:   Partial pressure of dry air          [hPa]
#
# Tr : reciprocal temperature              [1/K]
#
#           Tr=300/Tp where Tp is the physical air temperature in [K]
#
#
#
# oxygen93.txt: numerical table of size 7 x 44 with the 7 following parameters
#                           given for each of the 44 Oxygen Lines:
#
#
#
#           nu_k == oxygen[0, k]    : frequency of the k-th O2 absorption line
#           a1    == oxygen[1, k]    : constant for each line "k"
#           a2    == oxygen[2, k]    : constant for each line "k"
#           a3    == oxygen[3, k]    : constant for each line "k"
#           a4    == oxygen[4, k]    : constant for each line "k"
#           a5    == oxygen[5, k]    : constant for each line "k"
```

```

#
#           a6    == oxygen[6, k]   : constant for each line "k"
#
#
#
#
#
#
# Reference:
#
#
#
#
# H.J.Liebe, G.A.Hufford, and M.G.Cotton: Propagation Modeling OF Moist a
ir and          #
# Suspended Water/Ice Particles at frequencies Below 1000 GHz. In AGARD
52nd          #
# Specialists' Meeting of the Electromagnetic Wave Propagation Panel, Mal
Lorca, Spain, #
# May 1993
#
#
#
#
#           Code written by Reul.N      nicolas.reul@ifremer.fr
#
#
#
#
#           August 2023
#
# ##########
##########

def mpm_dry(freq, e, pd, Tr):

    # Load Data of the oxygen lines
    oxygen93 = np.loadtxt('oxygen93.txt')
    oxygen=np.transpose(oxygen93)

    ND = []
    for f in freq: # Loop for frequency

        nd = 0.2588 * pd * Tr # non-dispersive contribution

        for k in range(oxygen.shape[1]): # Loop for lines
            Sk = 1e-6 * oxygen[1, k] / oxygen[0, k] * pd * Tr**3 * np.exp(
oxygen[2, k] * (1 - Tr)) # line strength with correction 1e-6
            gammak = oxygen[3, k] / 1000 * (pd * Tr**oxygen[4, k] + 1.1 *
e * Tr) # line width
            gammak = np.sqrt(gammak**2 + 2.25e-6) # Zeeman-Effect
            deltak = 1e-3 * (oxygen[5, k] + oxygen[6, k] * Tr) * (pd + e)
* Tr**0.8 # Overlap parameter with correction 1e-3
            Fk = f * ((1 - 1j * deltak) / (oxygen[0, k] - f - 1j * gammak)
- (1 + 1j * deltak) / (oxygen[0, k] + f + 1j * gammak)) # lines form func
tion
            nd = nd + Sk * Fk

```

```

# non-resonant contribution
So = 6.14e-5 * pd * Tr**2
Fo = -f / (f + 1j * 0.56e-3 * (pd + e) * Tr**0.8)
Sn = 1.4e-12 * pd**2 * Tr**3.5
Fn = f / (1 + 1.93e-5 * f**1.5) # correction 1.9 -> 1.93
nd = nd + So * Fo + 1j * Sn * Fn
ND.append(nd)

return ND

```

9.4.2) Complex index of atmospheric refraction owing to water vapor

```

import numpy as np
import matplotlib.pyplot as plt
import scipy.io

#####
##### This subfunction is part of the MPM93 software package and computes
#
# the complex index of refraction for water vapor. The index of refraction
for water      #
# vapor is the sum of a nondispersive term, a continuum term, and a sum ov
er 35          #
# resonant absorption lines (including one pseudo-line at 1780 GHz).
#
# At the CIMR frequencies the continuum term is negligible.
#
#
#
# NV= mpm_vapor(freq, e, pd, Tr)
#
#
#
#-----#
# NV: index of refraction owing to water vapor:
#
#
#
#-----#
# Inputs:
#
#
#-----#
# freq: Electromagnetic frequency [GHz]
#
# e:    Partial pressure of the water vapour [hPa]
#

```



```

def mpm_vapor(freq, e, pd, Tr):

    # Load data for water vapor Lines
    water93 = np.loadtxt('water93.txt')
    water    = np.transpose(water93)

    NV = []
    for f in freq: # Loop over frequency
        nv = (4.163 * Tr + 0.239) * e * Tr # non-dispersive contribution

            for k in range(water.shape[1]): # Loop over Lines
                S = water[1, k] / water[0, k] * e * Tr**3.5 * np.exp(water[2,
k] * (1 - Tr)) # Line strength
                gammak = water[3, k] / 1000 * (water[4, k] * e * Tr**water[6,
k] + pd * Tr**water[5, k]) # Line width
                dopp = np.where(pd + e < 0.7)[0] # Doppler broadening
                if len(dopp) > 0:
                    gammak[dopp] = 0.535 * gammak[dopp] + np.sqrt(0.217 * gamm
ak[dopp]**2 + (1.46e-6 * gammak[dopp] * np.sqrt(Tr[dopp])))**2)
                    F = f * (1 / (water[0, k] - f - 1j * gammak) - 1 / (water[0, k]
] + f + 1j * gammak)) # Lines form function
                    nv = nv + S * F

    NV.append(nv)

return NV

```

9.4.3) Complex index of atmospheric refraction due to cloud liquid water

```
import numpy as np
import matplotlib.pyplot as plt
import scipy.io

#####
#####
# This subfunction is part of the MPM93 software package and computes
#
# the complex index of refraction for cloud liquid water.
#
#
#
#           Nw=mpm_water(freq, Tr, rho_clw)
#
#
#
#                                         #
#
#
#
# Outputs
#
#-----
#
# NW: complex index of refraction owing to cloud liquid water [ppm]
```

```

#
#
# Inputs:
#
#-----#
#
# freq: Electromagnetic frequency [GHz]
#
# rho_clw: Cloud Water droplet density [g/m^3]
#
# Tr : reciprocal temperature [1/K]
#
# Tr=300/Tp where Tp is the physical air temperature in [K]
#
#
#
#
# Code written by Reul. N. @Ifremer, May 2023
#
#
#
# Reference:
#
#
#
# H.J.Liebe, G.A.Hufford, and M.G.Cotton: Propagation Modeling OF Moist air and
# Suspended Water/Ice Particles at frequencies Below 1000 GHz. In AGARD
# 52nd Specialists' Meeting of the Electromagnetic Wave Propagation Panel, Mal
# lorca, Spain, #
# May 1993
#
#
#
# ##########
#####
```

```

def mpm_water(freq, Tr, rho_clw):

    # static and high-frequency permittivities
    eo = 77.66 + 103.3 * (Tr - 1)
    e1 = 0.0671 * eo
    e2 = 3.52 - 7.52 * (Tr - 1)

    # relaxation frequencies expressed in gigahertz;

    gamma1 = 20.2 - 146.4 * (Tr - 1) + 316 * (Tr - 1) ** 2
    gamma2 = 39.8 * gamma1

    NW = []

```

```

    for f in freq:
        ew = eo - f * ((eo - e1) / (f + 1j * gamma1) + (e1 - e2) / (f + 1j
* gamma2))
        NW.append(1.5 * (rho_clw) * (ew - 1) / (ew + 2))

    return NW

```

9.4.4 Complex index of atmospheric refraction for cloud ice water

```

import numpy as np
import matplotlib.pyplot as plt
import scipy.io

#####
#####
# This subfunction is part of the MPM93 software package and computes
#
# the complex index of refraction for cloud ice water.
#
#
#
# NI=mpm_ice(freq, Tr, rho_ice)
#
#
#
# -----
#
# NI: complex index of refraction owing to cloud ice water [ppm]
#
#
#
# Inputs:
#
# -----
#
# freq: Electromagnetic frequency [GHz]
#
# rho_ice: Cloud ice Water density [g/m^3]
#
# Tr : reciprocal temperature [1/K]
#
# Tr=300/Tp where Tp is the physical air temperature in [K]
#
#
#
#
#
# Code written by Reul. N. @Ifremer, May 2023

```

```

#
#
#
#   Reference:
#
#
#
#   H.J.Liebe, G.A.Hufford, and M.G.Cotton: Propagation Modeling OF Moist air and      #
#   Suspended Water/Ice Particles at frequencies Below 1000 GHz. In AGARD 52nd      #
#   Specialists' Meeting of the Electromagnetic Wave Propagation Panel, Mal Lorca, Spain, #
#   May 1993
#
#
#
# #####
#####

def mpm_ice(freq, Tr, rho_ice):

    ai = (Tr - 0.171) * np.exp(17.0 - 22.1 * Tr)
    bi = ((0.233 / (1 - 0.993 / Tr)) ** 2 + 6.33 / Tr - 1.31) * 1e-5

    NI = []

    for f in freq:
        ei = 3.15 + 1j * (ai / f + bi * f)
        NI.append(1.5 * (rho_ice/0.916) * ((ei - 1) / (ei + 2)))

    return NI

```

9.4.5 Complex index of atmospheric refraction owing to rain

```

import numpy as np
import matplotlib.pyplot as plt
import scipy.io

#####
#####

# This subfunction is part of the MPM93 software package and computes
#
# the complex index of refraction because of rain.
#
#
#
#           NR=mpm_rain(freq, R)
#
#
#
#                                     #

```

```
# Outputs
#
#-----
#
# NR: index of refraction owing to rain:
#
#
#
# Inputs:
#
#-----
#
# freq: Electromagnetic frequency [GHz]
#
# R   : Rain rate [mm/h]
#
#
#
#
#
# Code written by Reul. N. @Ifremer, May 2023
#
#
#
#
# Reference:
#
#
#
# H.J.Liebe, G.A.Hufford, and M.G.Cotton: Propagation Modeling OF Moist air and
# Suspended Water/Ice Particles at frequencies Below 1000 GHz. In AGARD
# 52nd
# Specialists' Meeting of the Electromagnetic Wave Propagation Panel, Mal
# lorca, Spain,
# May 1993
#
#
#
# #####
#####

def mpm_rain(freq, R):
    NR = []

    for f in freq:
        x1, y1, x2, y2 = 0, 0, 0, 0

        if 1 <= f <= 2.9:
            x1 = 3.51e-4
            y1 = 1.03
        elif 2.9 < f <= 54:
```

```

        x1 = 2.31e-4
        y1 = 1.42
    elif 54 < f <= 180:
        x1 = 0.225
        y1 = -0.301
    elif 180 < f <= 1000:
        x1 = 18.6
        y1 = -1.151

    if 1 <= f <= 8.5:
        x2 = 0.851
        y2 = 0.158
    elif 8.5 < f <= 25:
        x2 = 1.41
        y2 = -0.0779
    elif 25 < f <= 164:
        x2 = 2.63
        y2 = -0.272
    elif 164 < f <= 1000:
        x2 = 0.616
        y2 = 0.0126

    fr = 53 - R * (0.37 - 0.0015 * R)
    y = f / fr
    cr = x1 * f**y1
    z = x2 * f**y2

    NR.append((R * (0.012 * R - 3.7) * y**2.5) / (fr * (1 + y**2.5)) +
    1j * cr * R**z)

return NR

```

9.4.6 Example of Atmospheric contributions to TOA Brightness Temperatures

Here, we evaluate the upwelling and downwelling brightness temperature for vertical atmospheric profiles from the standard 1976 US atmosphere

9.4.6.1 standard 1976 atmosphere profiles

```

import numpy as np
import matplotlib.pyplot as plt
import scipy.io

#####
##### Load standard 1976 atmosphere used for illustration
#####

Stand_atm=np.loadtxt('Standard_1976_atmo.txt')

# Extract the columns

```

```

Z = Stand_atm[:, 0]      # Total Reporting Altitudes [0<=alt<=1000 km] [km]
]
T = Stand_atm[:, 1]      # Temperature array [0<=alt<=1000 km] [K]
P = Stand_atm[:, 2]      # Pressure array [0<=alt<=1000 km] [Pa]
rho = Stand_atm[:, 3]    # Density array [0<=alt<=1000 km] [kg/m^3]
print(np.size(T))

# Convert pressure to hPa
P = 0.01 * P

# Compute the reciprocal temperature in [1/K].
Tr = 300.0 / T

# Compute saturation vapor pressure in [hPa].
esat = 2.408e11 * Tr**5.0 * np.exp(-22.644 * Tr)

# Partial pressure of the water vapor
# We assume a constant 50% relative humidity versus altitude
rh = 50 * np.ones(len(Z)) # rh is relative humidity
e = esat * rh / 100

# Partial pressure of dry air
pd = P - e

# Compute dry air density in [kg/m^3].
# Recall pd is dry air pressure in [hPa].
Rd = 287.0
rho = pd * 100 / (Rd * Tr)

# The cloud Liquid water is assumed to be concentrated at a single altitude,
# and to have the temperature of the air at that altitude
# cloud liquid water density (usually called Liquid Water Content LWC)
clw = np.zeros(len(Z))
clw[10] = 1e-4 # m

# Compute density of cloud water in [kg/m^3].
# clw is assumed to be cloud water mixing ratio, which is
# defined as (mass of water) / (mass of dry air), and it has units of [kg/kg].
rho_water = rho * clw

# Separate into liquid and ice.
rho_ice = rho_water.copy()
ind = np.where(T < 273.15)[0]
rho_water[ind] = 0.0
ind = np.where(T >= 273.15)[0]
rho_ice[ind] = 0.0

# Plot T, P, rho as a function of Z for the 1976 U.S. Standard Atmosphere
plt.figure(1, figsize=(15, 5))

plt.subplot(131)
plt.plot(T, Z, '-', linewidth=2)

```

```

plt.xlabel('Atmospheric Temperature $T_p$ [K]', fontsize=18)
plt.ylabel('Height above Sea Level [km]', fontsize=18)
plt.grid(True)
plt.tick_params(labelsize=15)

plt.subplot(132)
plt.plot(P, Z, '--', linewidth=2)
plt.xlabel('Atmospheric Pressure [hPa]', fontsize=18)
plt.ylabel('Height above Sea Level [km]', fontsize=18)
plt.grid(True)
plt.tick_params(labelsize=15)

plt.subplot(133)
plt.plot(rho, Z, '--', linewidth=2)
plt.xlabel('Atmospheric Density [$kg/m^3$]', fontsize=18)
plt.ylabel('Height above Sea Level [km]', fontsize=18)
plt.grid(True)
plt.tick_params(labelsize=15)

plt.suptitle('1976 U.S. Standard Atmosphere', fontsize=25)
plt.tight_layout()
plt.show()

```

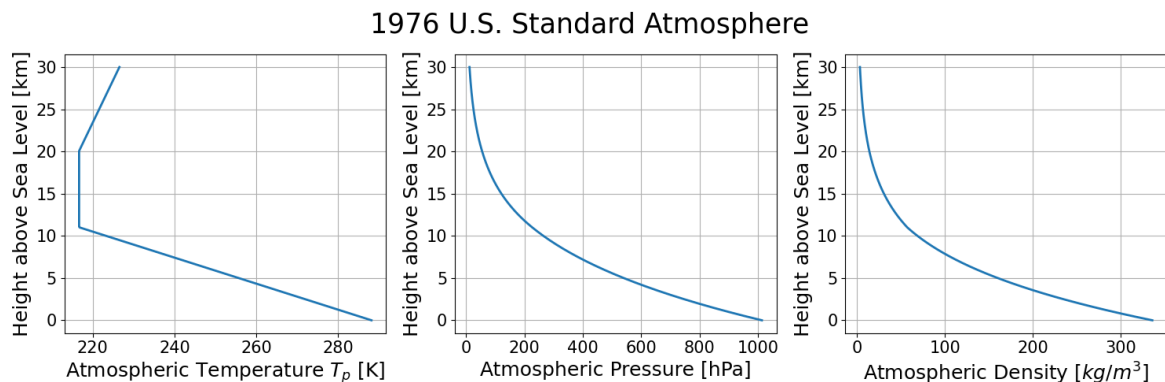


Figure 21 Vertical Profiles of left) Atmospheric Temperature, middle) Atmospheric Pressure, and, right) Atmospheric Density according to the 1976 U.S. Standard Atmosphere.

9.4.6.2 Evaluation at each vertical level and integration

```

# L-band indices of refractions

freqL = [1.4]

ND_L = mpm_dry(freqL, e, pd, Tr)
NV_L = mpm_vapor(freqL, e, pd, Tr)
NW_L = mpm_water(freqL, Tr, rho_water / 10000) # Here we must pass liquid
water density in units of [gm/cm^3].
NI_L = mpm_ice(freqL, Tr, rho_ice / 10000) # Here we must pass liquid water
density in units of [gm/cm^3]. 

# dB to nepers conversion factor.
db_to_nepers = np.log(10) / 10.0

```

```

# Convert index of refraction to power attenuation/distance (specific attenuation) in units of [nepers/m].
# Note that the MPM computes specific attenuation in units of [nepers/km], not [nepers/m].
# These attenuation coefficients apply to power not amplitude. Divide by two to get amplitude coefficients.
dry_alpha_L = db_to_nepers * 0.1820 * np.array(freqL) * np.imag(ND_L) / 1000
vapor_alpha_L = db_to_nepers * 0.1820 * np.array(freqL) * np.imag(NV_L) / 1000
water_alpha_L = db_to_nepers * 0.1820 * np.array(freqL) * np.imag(NW_L) / 1000
ice_alpha_L = db_to_nepers * 0.1820 * np.array(freqL) * np.imag(NI_L) / 1000

# C-band indices of refractions

freqC = [6.9]

ND_C = mpm_dry(freqC, e, pd, Tr)
NV_C = mpm_vapor(freqC, e, pd, Tr)
NW_C = mpm_water(freqC, Tr, rho_water / 10000) # Here we must pass liquid water density in units of [gm/cm^3].
NI_C = mpm_ice(freqC, Tr, rho_ice / 10000) # Here we must pass liquid water density in units of [gm/cm^3].

# Convert index of refraction to power attenuation/distance (specific attenuation) in units of [nepers/m].
# Note that the MPM computes specific attenuation in units of [nepers/km], not [nepers/m].
# These attenuation coefficients apply to power not amplitude. Divide by two to get amplitude coefficients.
dry_alpha_C = db_to_nepers * 0.1820 * np.array(freqC) * np.imag(ND_C) / 1000
vapor_alpha_C = db_to_nepers * 0.1820 * np.array(freqC) * np.imag(NV_C) / 1000
water_alpha_C = db_to_nepers * 0.1820 * np.array(freqC) * np.imag(NW_C) / 1000
ice_alpha_C = db_to_nepers * 0.1820 * np.array(freqC) * np.imag(NI_C) / 1000

# X-band indices of refractions

freqX = [10.7]

ND_X = mpm_dry(freqX, e, pd, Tr)
NV_X = mpm_vapor(freqX, e, pd, Tr)
NW_X = mpm_water(freqX, Tr, rho_water / 10000) # Here we must pass liquid water density in units of [gm/cm^3].
NI_X = mpm_ice(freqX, Tr, rho_ice / 10000) # Here we must pass liquid water density in units of [gm/cm^3].

# Convert index of refraction to power attenuation/distance (specific attenuation) in units of [nepers/m].

```

```
# Note that the MPM computes specific attenuation in units of [nepers/km],  
not [nepers/m].  
# These attenuation coefficients apply to power not amplitude. Divide by t  
wo to get amplitude coefficients.  
dry_alpha_X = db_to_nepers * 0.1820 * np.array(freqX) * np.imag(ND_X) / 10  
00  
vapor_alpha_X = db_to_nepers * 0.1820 * np.array(freqX) * np.imag(NV_X) /  
1000  
water_alpha_X = db_to_nepers * 0.1820 * np.array(freqX) * np.imag(NW_X) /  
1000  
ice_alpha_X = db_to_nepers * 0.1820 * np.array(freqX) * np.imag(NI_X) / 10  
00  
  
# Ku-band indices of refractions  
  
freqKu = [18.7]  
  
ND_Ku = mpm_dry(freqKu, e, pd, Tr)  
NV_Ku = mpm_vapor(freqKu, e, pd, Tr)  
NW_Ku = mpm_water(freqKu, Tr, rho_water / 10000) # Here we must pass liq  
id water density in units of [gm/cm^3].  
NI_Ku = mpm_ice(freqKu, Tr, rho_ice / 10000) # Here we must pass liquid w  
ater density in units of [gm/cm^3].  
  
# Convert index of refraction to power attenuation/distance (specific atte  
nuation) in units of [nepers/m].  
# Note that the MPM computes specific attenuation in units of [nepers/km],  
not [nepers/m].  
# These attenuation coefficients apply to power not amplitude. Divide by t  
wo to get amplitude coefficients.  
dry_alpha_Ku = db_to_nepers * 0.1820 * np.array(freqKu) * np.imag(ND_Ku) /  
1000  
vapor_alpha_Ku = db_to_nepers * 0.1820 * np.array(freqKu) * np.imag(NV_Ku)  
/ 1000  
water_alpha_Ku = db_to_nepers * 0.1820 * np.array(freqKu) * np.imag(NW_Ku)  
/ 1000  
ice_alpha_Ku = db_to_nepers * 0.1820 * np.array(freqKu) * np.imag(NI_Ku) /  
1000  
  
# Ka-band indices of refractions  
  
freqKa = [36.5]  
  
ND_Ka = mpm_dry(freqKa, e, pd, Tr)  
NV_Ka = mpm_vapor(freqKa, e, pd, Tr)  
NW_Ka = mpm_water(freqKa, Tr, rho_water / 10000) # Here we must pass liq  
id water density in units of [gm/cm^3].  
NI_Ka = mpm_ice(freqKa, Tr, rho_ice / 10000) # Here we must pass liquid w  
ater density in units of [gm/cm^3].  
  
# Convert index of refraction to power attenuation/distance (specific atte  
nuation) in units of [nepers/m].  
# Note that the MPM computes specific attenuation in units of [nepers/km],  
not [nepers/m].
```

```
# These attenuation coefficients apply to power not amplitude. Divide by two to get amplitude coefficients.
dry_alpha_Ka = db_to_nepers * 0.1820 * np.array(freqKa) * np.imag(ND_Ka) / 1000
vapor_alpha_Ka = db_to_nepers * 0.1820 * np.array(freqKa) * np.imag(NV_Ka) / 1000
water_alpha_Ka = db_to_nepers * 0.1820 * np.array(freqKa) * np.imag(NW_Ka) / 1000
ice_alpha_Ka = db_to_nepers * 0.1820 * np.array(freqKa) * np.imag(NI_Ka) / 1000

from scipy import integrate

# CIMR beams central incidence angle at each frequency (L,C,X,Ku,Ka)

EIA = [51.95, 55.2, 55.2, 55.2, 55.2]

Z = Stand_atm[:,0]          # Total Reporting Altitudes [0<=alt<=1000 km] [km]
Z = Z * 1e3    # height in meters

#####
##### Compute integrated absorption from the surface to each level.
#####

# L-band
att_dry_up_L = integrate.cumtrapz(dry_alpha_L * 1/np.cos(np.radians(EIA[0])), Z, initial=0)
att_vapor_up_L = integrate.cumtrapz(vapor_alpha_L * 1/np.cos(np.radians(EIA[0])), Z, initial=0)
att_water_up_L = integrate.cumtrapz(water_alpha_L * 1/np.cos(np.radians(EIA[0])), Z, initial=0)
att_ice_up_L = integrate.cumtrapz(ice_alpha_L * 1/np.cos(np.radians(EIA[0])), Z, initial=0)
att_tot_up_L = att_dry_up_L + att_vapor_up_L + att_water_up_L + att_ice_up_L

# C-band
att_dry_up_C = integrate.cumtrapz(dry_alpha_C * 1/np.cos(np.radians(EIA[1])), Z, initial=0)
att_vapor_up_C = integrate.cumtrapz(vapor_alpha_C * 1/np.cos(np.radians(EIA[1])), Z, initial=0)
att_water_up_C = integrate.cumtrapz(water_alpha_C * 1/np.cos(np.radians(EIA[1])), Z, initial=0)
att_ice_up_C = integrate.cumtrapz(ice_alpha_C * 1/np.cos(np.radians(EIA[1])), Z, initial=0)
att_tot_up_C = att_dry_up_C + att_vapor_up_C + att_water_up_C + att_ice_up_C

# X-band
att_dry_up_X = integrate.cumtrapz(dry_alpha_X * 1/np.cos(np.radians(EIA[2])), Z, initial=0)
```

```

att_vapor_up_X = integrate.cumtrapz(vapor_alpha_X * 1/np.cos(np.radians(EI
A[2])), Z, initial=0)
att_water_up_X = integrate.cumtrapz(water_alpha_X * 1/np.cos(np.radians(EI
A[2])), Z, initial=0)
att_ice_up_X = integrate.cumtrapz(ice_alpha_X * 1/np.cos(np.radians(EIA[2]
))), Z, initial=0)
att_tot_up_X = att_dry_up_X + att_vapor_up_X + att_water_up_X + att_ice_up
_X

# Ku-band
att_dry_up_Ku = integrate.cumtrapz(dry_alpha_Ku * 1/np.cos(np.radians(EIA[
3])), Z, initial=0)
att_vapor_up_Ku= integrate.cumtrapz(vapor_alpha_Ku * 1/np.cos(np.radians(E
IA[3])), Z, initial=0)
att_water_up_Ku = integrate.cumtrapz(water_alpha_Ku * 1/np.cos(np.radians(
EIA[3])), Z, initial=0)
att_ice_up_Ku = integrate.cumtrapz(ice_alpha_Ku * 1/np.cos(np.radians(EIA[
3])), Z, initial=0)
att_tot_up_Ku = att_dry_up_Ku + att_vapor_up_Ku + att_water_up_Ku + att_ic
e_up_Ku

# Ka-band
att_dry_up_Ka = integrate.cumtrapz(dry_alpha_Ka * 1/np.cos(np.radians(EIA[
4])), Z, initial=0)
att_vapor_up_Ka= integrate.cumtrapz(vapor_alpha_Ka * 1/np.cos(np.radians(E
IA[4])), Z, initial=0)
att_water_up_Ka = integrate.cumtrapz(water_alpha_Ka * 1/np.cos(np.radians(
EIA[4])), Z, initial=0)
att_ice_up_Ka = integrate.cumtrapz(ice_alpha_Ka * 1/np.cos(np.radians(EIA[
4])), Z, initial=0)
att_tot_up_Ka = att_dry_up_Ku + att_vapor_up_Ka + att_water_up_Ka + att_ic
e_up_Ka

#####
#####
# Compute integrated absorption from the top down to each level.
#####
#####

# L-band
tatt_dry_down_L = -integrate.cumtrapz(dry_alpha_L * 1/np.cos(np.radians(
EIA[0])), Z[::-1]);
tatt_vapor_down_L = -integrate.cumtrapz(vapor_alpha_L * 1/np.cos(np.radian
s(EIA[0])), Z[::-1]);
tatt_water_down_L = -integrate.cumtrapz(water_alpha_L * 1/np.cos(np.radian
s(EIA[0])), Z[::-1]);
tatt_ice_down_L = -integrate.cumtrapz(ice_alpha_L * 1/np.cos(np.radians(
EIA[0])), Z[::-1]);
att_dry_down_L = tatt_dry_down_L[::-1];
att_vapor_down_L = tatt_vapor_down_L[::-1];
att_water_down_L = tatt_water_down_L[::-1];
att_ice_down_L = tatt_ice_down_L[::-1];
att_tot_down_L = att_dry_down_L + att_vapor_down_L + att_water_down_L +

```

```

att_ice_down_L;

# C-band

tatt_dry_down_C = -integrate.cumtrapz(dry_alpha_C * 1/np.cos(np.radians(
EIA[1])), Z[::-1]);
tatt_vapor_down_C = -integrate.cumtrapz(vapor_alpha_C * 1/np.cos(np.radians(
EIA[1])), Z[::-1]);
tatt_water_down_C = -integrate.cumtrapz(water_alpha_C * 1/np.cos(np.radians(
EIA[1])), Z[::-1]);
tatt_ice_down_C = -integrate.cumtrapz(ice_alpha_C * 1/np.cos(np.radians(
EIA[1])), Z[::-1]);
att_dry_down_C = tatt_dry_down_C[::-1];
att_vapor_down_C = tatt_vapor_down_C[::-1];
att_water_down_C = tatt_water_down_C[::-1];
att_ice_down_C = tatt_ice_down_C[::-1];
att_tot_down_C = att_dry_down_C + att_vapor_down_C + att_water_down_C +
att_ice_down_C;

# X-band

tatt_dry_down_X = -integrate.cumtrapz(dry_alpha_X * 1/np.cos(np.radians(
EIA[2])), Z[::-1]);
tatt_vapor_down_X = -integrate.cumtrapz(vapor_alpha_X * 1/np.cos(np.radians(
EIA[2])), Z[::-1]);
tatt_water_down_X = -integrate.cumtrapz(water_alpha_X * 1/np.cos(np.radians(
EIA[2])), Z[::-1]);
tatt_ice_down_X = -integrate.cumtrapz(ice_alpha_X * 1/np.cos(np.radians(
EIA[2])), Z[::-1]);
att_dry_down_X = tatt_dry_down_X[::-1];
att_vapor_down_X = tatt_vapor_down_X[::-1];
att_water_down_X = tatt_water_down_X[::-1];
att_ice_down_X = tatt_ice_down_X[::-1];
att_tot_down_X = att_dry_down_X + att_vapor_down_X + att_water_down_X +
att_ice_down_X;

# Ku-band

tatt_dry_down_Ku = -integrate.cumtrapz(dry_alpha_Ku * 1/np.cos(np.radians(
EIA[3])), Z[::-1]);
tatt_vapor_down_Ku = -integrate.cumtrapz(vapor_alpha_Ku * 1/np.cos(np.radians(
EIA[3])), Z[::-1]);
tatt_water_down_Ku = -integrate.cumtrapz(water_alpha_Ku * 1/np.cos(np.radians(
EIA[3])), Z[::-1]);
tatt_ice_down_Ku = -integrate.cumtrapz(ice_alpha_Ku * 1/np.cos(np.radians(
EIA[3])), Z[::-1]);
att_dry_down_Ku = tatt_dry_down_Ku[::-1];
att_vapor_down_Ku = tatt_vapor_down_Ku[::-1];
att_water_down_Ku = tatt_water_down_Ku[::-1];
att_ice_down_Ku = tatt_ice_down_Ku[::-1];
att_tot_down_Ku = att_dry_down_Ku + att_vapor_down_Ku + att_water_down_Ku +
att_ice_down_Ku;

# Ka-band

```

```

tatt_dry_down_Ka = -integrate.cumtrapz(dry_alpha_Ka * 1/np.cos(np.radians(EIA[4])), Z[::-1]);
tatt_vapor_down_Ka = -integrate.cumtrapz(vapor_alpha_Ka * 1/np.cos(np.radians(EIA[4])), Z[::-1]);
tatt_water_down_Ka = -integrate.cumtrapz(water_alpha_Ka * 1/np.cos(np.radians(EIA[4])), Z[::-1]);
tatt_ice_down_Ka = -integrate.cumtrapz(ice_alpha_Ka * 1/np.cos(np.radians(EIA[4])), Z[::-1]);
att_dry_down_Ka = tatt_dry_down_Ka[::-1];
att_vapor_down_Ka = tatt_vapor_down_Ka[::-1];
att_water_down_Ka = tatt_water_down_Ka[::-1];
att_ice_down_Ka = tatt_ice_down_Ka[::-1];
att_tot_down_Ka = att_dry_down_Ka + att_vapor_down_Ka + att_water_down_Ka + att_ice_down_Ka;

#####
##### Compute transmission from each Level to the bottom of the atmosphere at zenith.
# This is also the transmission from the bottom to each level in the atmosphere.
#####

# L-band
trans_dry_up_L = np.exp(-att_dry_up_L);
trans_vapor_up_L = np.exp(-att_vapor_up_L);
trans_water_up_L = np.exp(-att_water_up_L);
trans_ice_up_L = np.exp(-att_ice_up_L);
trans_total_up_L = trans_dry_up_L * trans_vapor_up_L * trans_water_up_L * trans_ice_up_L

# C-band
trans_dry_up_C = np.exp(-att_dry_up_C);
trans_vapor_up_C = np.exp(-att_vapor_up_C);
trans_water_up_C = np.exp(-att_water_up_C);
trans_ice_up_C = np.exp(-att_ice_up_C);
trans_total_up_C = trans_dry_up_C * trans_vapor_up_C * trans_water_up_C * trans_ice_up_C

# X-band
trans_dry_up_X = np.exp(-att_dry_up_X);
trans_vapor_up_X = np.exp(-att_vapor_up_X);
trans_water_up_X = np.exp(-att_water_up_X);
trans_ice_up_X = np.exp(-att_ice_up_X);
trans_total_up_X = trans_dry_up_X * trans_vapor_up_X * trans_water_up_X * trans_ice_up_X

# Ku-band
trans_dry_up_Ku = np.exp(-att_dry_up_Ku);
trans_vapor_up_Ku = np.exp(-att_vapor_up_Ku);
trans_water_up_Ku = np.exp(-att_water_up_Ku);
trans_ice_up_Ku = np.exp(-att_ice_up_Ku);

```

```

trans_total_up_Ku = trans_dry_up_Ku * trans_vapor_up_Ku * trans_water_up
_Ku * trans_ice_up_Ku

# Ka-band
trans_dry_up_Ka = np.exp(-att_dry_up_Ka);
trans_vapor_up_Ka = np.exp(-att_vapor_up_Ka);
trans_water_up_Ka = np.exp(-att_water_up_Ka);
trans_ice_up_Ka = np.exp(-att_ice_up_Ka);
trans_total_up_Ka = trans_dry_up_Ka * trans_vapor_up_Ka * trans_water_up
_Ka * trans_ice_up_Ka

#####
#####
# Compute transmission from each Level to the top of the atmosphere at zenith.
#####
#####

# L-band
trans_dry_down_L = np.exp(-att_dry_down_L);
trans_vapor_down_L = np.exp(-att_vapor_down_L);
trans_water_down_L = np.exp(-att_water_down_L);
trans_ice_down_L = np.exp(-att_ice_down_L);
trans_total_down_L = trans_dry_down_L * trans_vapor_down_L * trans_water_d
own_L * trans_ice_down_L

# C-band
trans_dry_down_C = np.exp(-att_dry_down_C);
trans_vapor_down_C = np.exp(-att_vapor_down_C);
trans_water_down_C = np.exp(-att_water_down_C);
trans_ice_down_C = np.exp(-att_ice_down_C);
trans_total_down_C = trans_dry_down_C * trans_vapor_down_C * trans_water_d
own_C * trans_ice_down_C

# X-band
trans_dry_down_X = np.exp(-att_dry_down_X);
trans_vapor_down_X = np.exp(-att_vapor_down_X);
trans_water_down_X = np.exp(-att_water_down_X);
trans_ice_down_X = np.exp(-att_ice_down_X);
trans_total_down_X = trans_dry_down_X * trans_vapor_down_X * trans_water_d
own_X * trans_ice_down_X

# Ku-band
trans_dry_down_Ku = np.exp(-att_dry_down_Ku);
trans_vapor_down_Ku = np.exp(-att_vapor_down_Ku);
trans_water_down_Ku = np.exp(-att_water_down_Ku);
trans_ice_down_Ku = np.exp(-att_ice_down_Ku);
trans_total_down_Ku = trans_dry_down_Ku * trans_vapor_down_Ku * trans_wate
r_down_Ku * trans_ice_down_Ku

# Ka-band
trans_dry_down_Ka = np.exp(-att_dry_down_Ka);

```

```

trans_vapor_down_Ka = np.exp(-att_vapor_down_Ka);
trans_water_down_Ka = np.exp(-att_water_down_Ka);
trans_ice_down_Ka   = np.exp(-att_ice_down_Ka);
trans_total_down_Ka = trans_dry_down_Ka * trans_vapor_down_Ka * trans_water_down_Ka * trans_ice_down_Ka

#####
##### Compute unpolarized brightness temperature at each level. These variables may be viewed
# as incremental brightnesses which are then attenuated by intervening atmosphere.
#####

ltb_dry_L      = T * dry_alpha_L;
ltb_vapor_L    = T * vapor_alpha_L;
ltb_water_L    = T * water_alpha_L;
ltb_ice_L      = T * ice_alpha_L;
ltb_L          = ltb_dry_L + ltb_vapor_L + ltb_water_L + ltb_ice_L;

ltb_dry_C      = T * dry_alpha_C;
ltb_vapor_C    = T * vapor_alpha_C;
ltb_water_C    = T * water_alpha_C;
ltb_ice_C      = T * ice_alpha_C;
ltb_C          = ltb_dry_C + ltb_vapor_C + ltb_water_C + ltb_ice_C;

ltb_dry_X      = T * dry_alpha_X;
ltb_vapor_X    = T * vapor_alpha_X;
ltb_water_X    = T * water_alpha_X;
ltb_ice_X      = T * ice_alpha_X;
ltb_X          = ltb_dry_X + ltb_vapor_X + ltb_water_X + ltb_ice_X;

ltb_dry_Ku     = T * dry_alpha_Ku;
ltb_vapor_Ku   = T * vapor_alpha_Ku;
ltb_water_Ku   = T * water_alpha_Ku;
ltb_ice_Ku     = T * ice_alpha_Ku;
ltb_Ku         = ltb_dry_Ku + ltb_vapor_Ku + ltb_water_Ku + ltb_ice_Ku;

ltb_dry_Ka     = T * dry_alpha_Ka;
ltb_vapor_Ka   = T * vapor_alpha_Ka;
ltb_water_Ka   = T * water_alpha_Ka;
ltb_ice_Ka     = T * ice_alpha_Ka;
ltb_Ka         = ltb_dry_Ka + ltb_vapor_Ka + ltb_water_Ka + ltb_ice_Ka;

#####
##### Compute integrated unpolarized brightness temp. at the top of the atmosphere.
#####

```

```

tb_top_L = integrate.cumtrapz(trans_total_down_L * ltb_L[0,0:300] * 1/np.
cos(np.radians(EIA[0])), Z[0:300], initial=0)
tb_top_C = integrate.cumtrapz(trans_total_down_C * ltb_C[0,0:300] * 1/np.
cos(np.radians(EIA[1])), Z[0:300], initial=0)
tb_top_X = integrate.cumtrapz(trans_total_down_X * ltb_X[0,0:300] * 1/np.
cos(np.radians(EIA[2])), Z[0:300], initial=0)
tb_top_Ku = integrate.cumtrapz(trans_total_down_Ku * ltb_Ku[0,0:300] * 1/
np.cos(np.radians(EIA[3])), Z[0:300], initial=0)
tb_top_Ka = integrate.cumtrapz(trans_total_down_Ka * ltb_Ka[0,0:300] * 1/
np.cos(np.radians(EIA[4])), Z[0:300], initial=0)

#####
##### Compute integrated unpolarized brightness temp. at the bottom of the atm
##### osphere.
#####

trans_total_up_reversed_L = trans_total_up_L[0,:,:-1]
ltb_reversed_L = ltb_L[:,::-1]
secd_EIA = 1/np.cos(np.radians(EIA[0]))
# Perform the cumulative trapezoidal integration
tv = integrate.cumtrapz(trans_total_up_reversed_L * ltb_reversed_L * secd_
EIA, Z, initial=0)
tb_bottom_L= tv[:,::-1]

trans_total_up_reversed_C = trans_total_up_C[0,:,:-1]
ltb_reversed_C = ltb_C[:,::-1]
secd_EIA = 1/np.cos(np.radians(EIA[1]))
# Perform the cumulative trapezoidal integration
tv = integrate.cumtrapz(trans_total_up_reversed_C * ltb_reversed_C * secd_
EIA, Z, initial=0)
tb_bottom_C= tv[:,::-1]

trans_total_up_reversed_X = trans_total_up_X[0,:,:-1]
ltb_reversed_X = ltb_X[:,::-1]
secd_EIA = 1/np.cos(np.radians(EIA[2]))
# Perform the cumulative trapezoidal integration
tv = integrate.cumtrapz(trans_total_up_reversed_X * ltb_reversed_X * secd_
EIA, Z, initial=0)
tb_bottom_X= tv[:,::-1]

trans_total_up_reversed_Ku = trans_total_up_Ku[0,:,:-1]
ltb_reversed_Ku = ltb_Ku[:,::-1]
secd_EIA = 1/np.cos(np.radians(EIA[3]))
# Perform the cumulative trapezoidal integration
tv = integrate.cumtrapz(trans_total_up_reversed_Ku * ltb_reversed_Ku * sec
d_EIA, Z, initial=0)
tb_bottom_Ku= tv[:,::-1]

trans_total_up_reversed_Ka = trans_total_up_Ka[0,:,:-1]
ltb_reversed_Ka = ltb_Ka[:,::-1]
secd_EIA = 1/np.cos(np.radians(EIA[4]))
# Perform the cumulative trapezoidal integration

```

```
tv = integrate.cumtrapz(trans_total_up_reversed_Ka * ltb_reversed_Ka * sec  
d_EIA, Z, initial=0)  
tb_bottom_Ka= tv[:,::-1]  
  
# Plot Upwelling and downwelling atmospheric Tbs a function of Z for the 1  
976 U.S. Standard Atmosphere  
plt.figure(1, figsize=(15, 5))  
  
#print(tb_bottom_L)  
#print(np.size(Z[0:299]))  
  
plt.subplot(131)  
plt.plot(tb_top_L[0,0:300], Z[0:300]/1e3, '--', linewidth=2)  
plt.plot(tb_top_C[0,0:300], Z[0:300]/1e3, '--', linewidth=2)  
plt.plot(tb_top_X[0,0:300], Z[0:300]/1e3, '--', linewidth=2)  
plt.plot(tb_top_Ku[0,0:300], Z[0:300]/1e3, '--', linewidth=2)  
plt.plot(tb_top_Ka[0,0:300], Z[0:300]/1e3, '--', linewidth=2)  
  
plt.xlabel('Upwelling Atmospheric Temperature $T_{up} [K]', fontsize=12)  
plt.ylabel('Height above Sea Level [km]', fontsize=12)  
plt.grid(True)  
plt.tick_params(labelsize=12)  
  
plt.subplot(132)  
plt.plot(tb_bottom_L[0,0:300], Z[0:300]/1e3, '--', linewidth=2)  
plt.plot(tb_bottom_C[0,0:300], Z[0:300]/1e3, '--', linewidth=2)  
plt.plot(tb_bottom_X[0,0:300], Z[0:300]/1e3, '--', linewidth=2)  
plt.plot(tb_bottom_Ku[0,0:300], Z[0:300]/1e3, '--', linewidth=2)  
plt.plot(tb_bottom_Ka[0,0:300], Z[0:300]/1e3, '--', linewidth=2)  
  
plt.legend(['L-band at $\u03b8_{ref}=51.95^\circ$',  
           'C-band at $\u03b8_{ref}=55.2^\circ$',  
           'X-band at $\u03b8_{ref}=55.2^\circ$',  
           'Ku-band at $\u03b8_{ref}=55.2^\circ$',  
           'Ka-band at $\u03b8_{ref}=55.2^\circ$'],  
           loc='best')  
plt.xlabel('Downwelling Atmospheric Temperature $T_{dw} [K]', fontsize=12)  
plt.ylabel('Height above Sea Level [km]', fontsize=12)  
plt.grid(True)  
plt.tick_params(labelsize=12)  
#plt.suptitle('1976 U.S. Standard Atmosphere', fontsize=25)  
plt.tight_layout()  
plt.show()
```

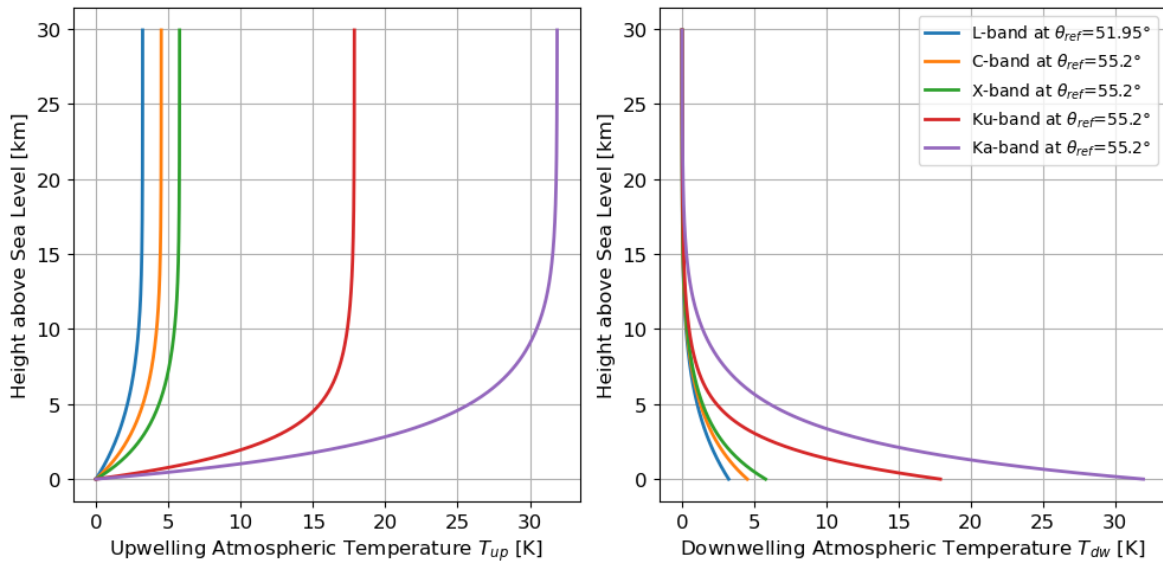


Figure 22 Vertical Profiles of left) Atmospheric Upwelling brightness temperatures and, right) Downwelling atmospheric brightness temperatures for the 1976 U.S. Standard atmosphere

```
from IPython.core.display import HTML as Center

Center("""""")

plt.figure(1, figsize=(5, 5))
plt.rcParams["figure.figsize"] = [5, 5]
plt.rcParams["figure.autolayout"] = True
plt.plot(trans_total_up_L[0,0:300], Z[0:300]/1e3, '--', linewidth=2)
plt.plot(trans_total_up_C[0,0:300], Z[0:300]/1e3, '--', linewidth=2)
plt.plot(trans_total_up_X[0,0:300], Z[0:300]/1e3, '--', linewidth=2)
plt.plot(trans_total_up_Ku[0,0:300], Z[0:300]/1e3, '--', linewidth=2)
plt.plot(trans_total_up_Ka[0,0:300], Z[0:300]/1e3, '--', linewidth=2)
plt.xlabel('Atmospheric Transmittance $\u03c4$', fontsize=12)
plt.ylabel('Height above Sea Level [km]', fontsize=12)
plt.grid(True)
plt.legend(['L-band',
           'C-band',
           'X-band',
           'Ku-band',
           'Ka-band'],
           loc='best')
plt.tick_params(labelsize=12)
plt.tight_layout()
plt.show()
```

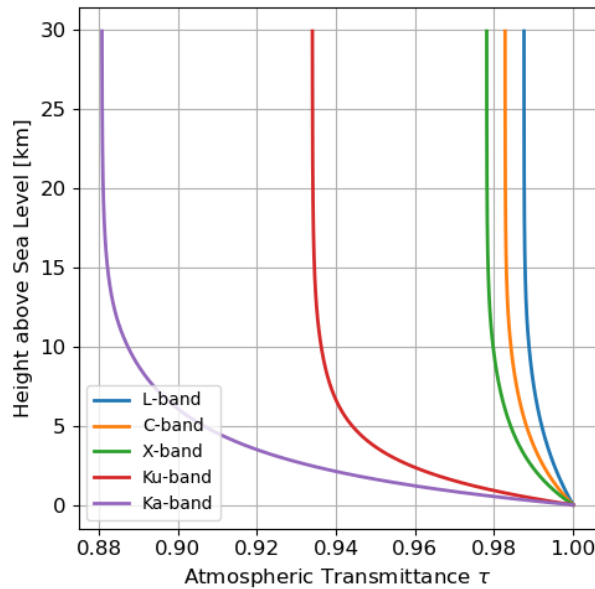


Figure 23 Vertical Profiles of Total Atmospheric Transmittance for the 1976 U.S. Standard atmosphere

10. Algorithm performance assessment using SCEPS

To assess the performance of the previously described SSS retrieval algorithm, we used the SCEPS prototype simulator to generate a very large test card ($\sim 6000 \text{ km} \times 4000 \text{ km}$), with 1 km resolution including strong SSS gradients due to the Amazon River plume, and, strong surface wind speed gradients with the presence of two hurricanes (see **Figure 25**).

As described in RD.2, the simulator consists of a single statically-linked linux executable program, cimrProject, which produces a Level 1b antenna temperature product from input scene brightness information. The program takes as input an EO-CFI orbit definition file (Team, 2022), a file containing the scene brightness temperature in the form of a 'test card', complete GRASP-generated antenna patterns provided by industry and a file that specifies the sample times at which to produce antenna temperatures. The scene brightness includes both the isotropic and anisotropic complete modified Stokes vector (T_h, T_v, U, V) in the surface polarization basis. The isotropic part can vary with incidence angle, while, for practical reasons in our analyses, the anisotropic part is assumed to be independent of incidence angle.

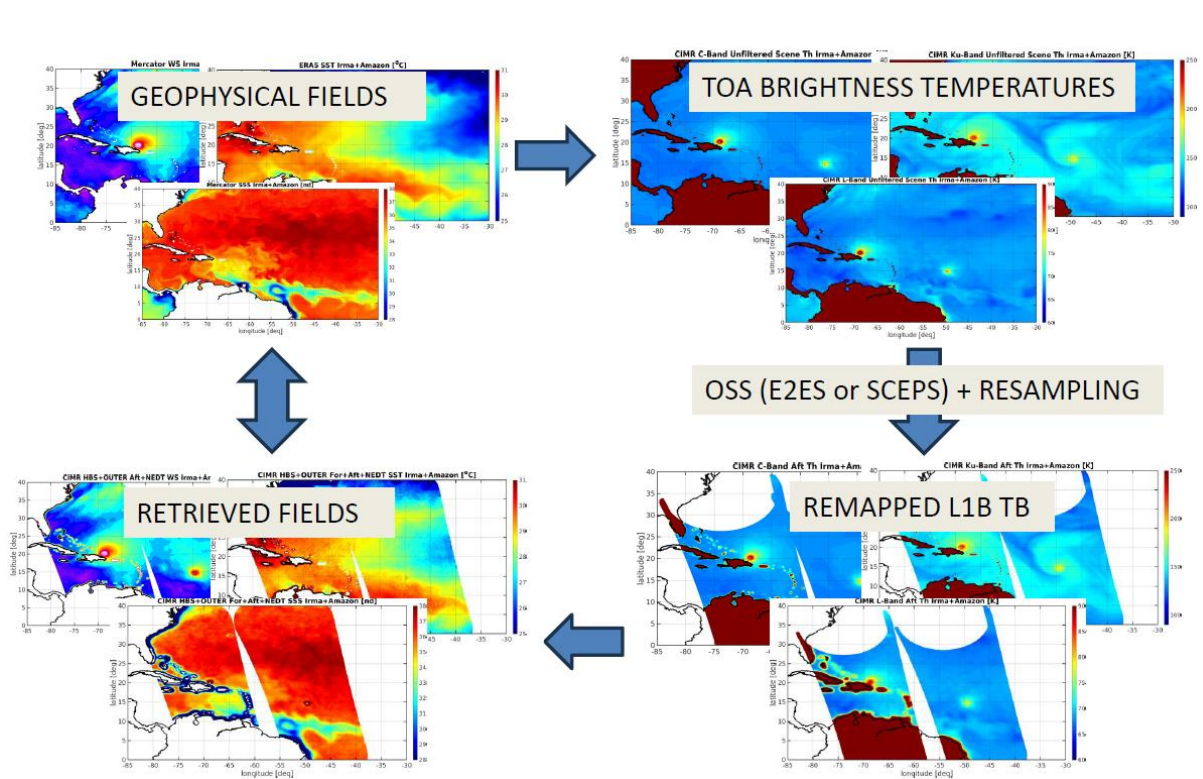


Figure 24: Schematic of the retrieval algorithm assessment using SCEPS

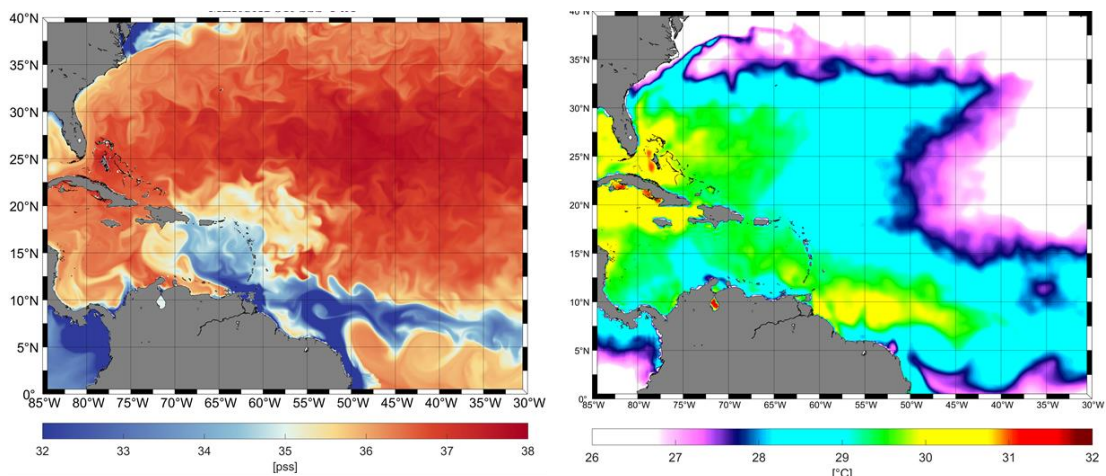
A schematic of the overall retrieval algorithm assessment using SCEPS is provided in Figure 24. The assessment is based upon these successive steps:

- 1) The scene is first described by geophysical fields, including: SSS, SST, OWV at $\sim 1\text{km}$ spatial resolution and the interpolated (in space and time) atmospheric vertical parameters from ERA5,
- 2) The TOA brightness temperatures are then evaluated for L-band and polarization using the previously described RTM for an ensemble of incidence angles. The azimuthal harmonic contributions to total TOA temperature are also evaluated separately,

- 3) The computation of (noisy) simulated CIMR antenna temperature from the scene brightness temperature field then involves several aspects:
- 3.1 Calculation of orbit and viewing geometry,
 - 3.2 Calculation of the scene brightness Stokes vector,
 - 3.3 Integration of the scene brightness over the antenna patterns (both near and far from the feed boresights) for each horn;
 - 3.4 Addition of NEDT noise to the antenna temperatures,
 - 3.5 Calculation and application of the Antenna Pattern Correction (APC) matrices for all feeds,
 - to reduce/remove cross-pol contamination. For these tests, this APC has the polarization basis rotation 'built-in';
 - 3.6 Production of a preliminary version of the Level 1b product.
- 4) Resampled brightness temperature are then computed by applying the Backus-Gilbert method to express in the surface polarization basis: SCEPS uses elliptical power patterns (on earth) to compute the BG inner products. Fore and aft sampled can be combined or kept separated in fore and aft images; The Target grid is the original testcard at 1km resolution and the target patterns are all circular Gaussians with FWHM for L- band defined as 60 km; A single application of BG yields weights that can be applied to all antenna pattern contributions;
- Maps of error variance amplification factors are computed from the BG weights.
- 5) The noisy simulated resampled CIMR L1b antenna temperature from the scene brightness temperature field are then used for simulation of the future CIMR remapped 'measured L1B Tbs'.

9.1 Geophysical data used to describe the ocean scene

The synthetic wind field used to model the scene is a merge between ERA5 re-analyses used as the background wind field, and, more local and high-resolution surface winds from Sentinel-1/2 SAR data around two hurricanes. The SSS is from MERCATOR model, the SST is from ERA5 re-analyses which were also used to simulate the atmospheric vertical profiles. The test scene includes several coasts to analyze the land-contamination.



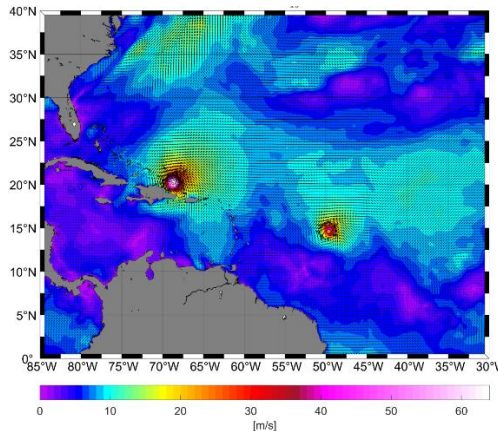


Figure 25: Input geophysical data used to simulate the test card: (top left): SSS from Mercator; (top right) ERA5 SST and (bottom) merged ERA5 & SAR images (over the two hurricanes) surface wind vectors.

9.2 Simulated TOA Tbs over the scene

Using these geophysical data as input, we generated TOA L-band TOA Tbs using the previously described RTM at an ensemble of EIA with values of $0^\circ, 20^\circ, 40^\circ, 50^\circ, 55^\circ, 60^\circ, 70^\circ, 80^\circ$ including azimuthal harmonics for the full Stokes vector. Note: in the Forward Model simulations we assumed the anisotropic roughness effects to be similar at all EIA values. ERA5 vertical profiles for Cloud Liquid, ice Water Content, air temperature, humidity were used to evaluate the atmospheric contributions at each frequency. Land Tbs~300K are from the SCEPS project (courtesy Carlos Jimenez). Example of such Tb fields are shown in Figure 26.

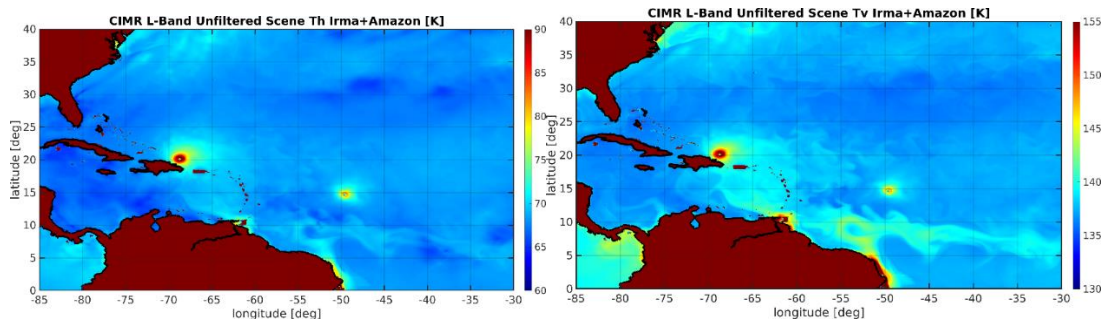


Figure 26: (Top Left) L-band H-pol, (Top right) L-band V-pol; (2nd panel from Top Left) C-band H-pol, (2nd panel from Top right) C-band V-pol ; (3rd panel from Top Left) X-band H-pol, (3rd panel from Top right) X-band V-pol; (4th panel from Top Left) Ku-band H-pol, (4th panel from Top right) Ku-band V-pol; (Bottom panel, left)) Ka-band H-pol; (Bottom panel, right)) Ka-band H-pol; based on the Radiative forward model (EIA=52° for L-band and EIA=55° for X-Ka band).

As described in previous sections, the roughness-induced emission ΔT_p can be decomposed into isotropic, and, anisotropic, emission components using a second order azimuthal harmonic expansion as a function of $\tilde{\varphi}$, the relative azimuth between the radiometer look direction and the wind direction. The Stokes vector of the total brightness temperature emitted by the sea surface at location (x_1, x_2) and at an EIA of θ_s thus reads:

$$\begin{aligned} T_h(x_1, x_2, \theta_s) &= T_{hso} + T_{ho}(U_{10}) + T_{hc1}(U_{10}) \cos(\tilde{\varphi}) + T_{hc2}(U_{10}) \cos(2\tilde{\varphi}) \\ T_v(x_1, x_2, \theta_s) &= T_{vso} + T_{vo}(U_{10}) + T_{vc1}(U_{10}) \cos(\tilde{\varphi}) + T_{vc2}(U_{10}) \cos(2\tilde{\varphi}) \\ U(x_1, x_2, \theta_s) &= U_{hs1}(U_{10}) \sin(\tilde{\varphi}) + U_{hs2}(U_{10}) \sin(2\tilde{\varphi}) \end{aligned}$$

$$V(x_1, x_2, \theta_s) = V_{hs1}(U_{10}) \sin(\tilde{\varphi}) + V_{hs2}(U_{10}) \sin(2\tilde{\varphi})$$

As found, only the horizontal and vertical polarization exhibit isotropic contributions (0th order azimuthal harmonics), namely, $T_{ho}(U_{10})$ and $T_{vo}(U_{10})$. The amplitude of these isotropic components are significantly larger than the first order azimuthal harmonics ($T_{hc1}(U_{10}), T_{vc1}(U_{10}), U_{hs1}(U_{10}), V_{hs1}(U_{10})$) and the second order azimuthal harmonics ($T_{hc2}(U_{10}), T_{vc2}(U_{10}), U_{hs2}(U_{10}), V_{hs2}(U_{10})$). Note that the third U and fourth V Stokes vector components are non-zero only because of anisotropic features of the sea surface roughness.

For each frequency, SCEPS integrates the harmonic contributions (see Figure 27):

$$T_{hc1}(U_{10}), T_{vc1}(U_{10}), U_{hs1}(U_{10}), V_{hs1}(U_{10}), T_{hc2}(U_{10}), T_{vc2}(U_{10}), U_{hs2}(U_{10}), V_{hs2}(U_{10})$$

to total antenna temperature separately and stores them in an extended L1B netCDF file.

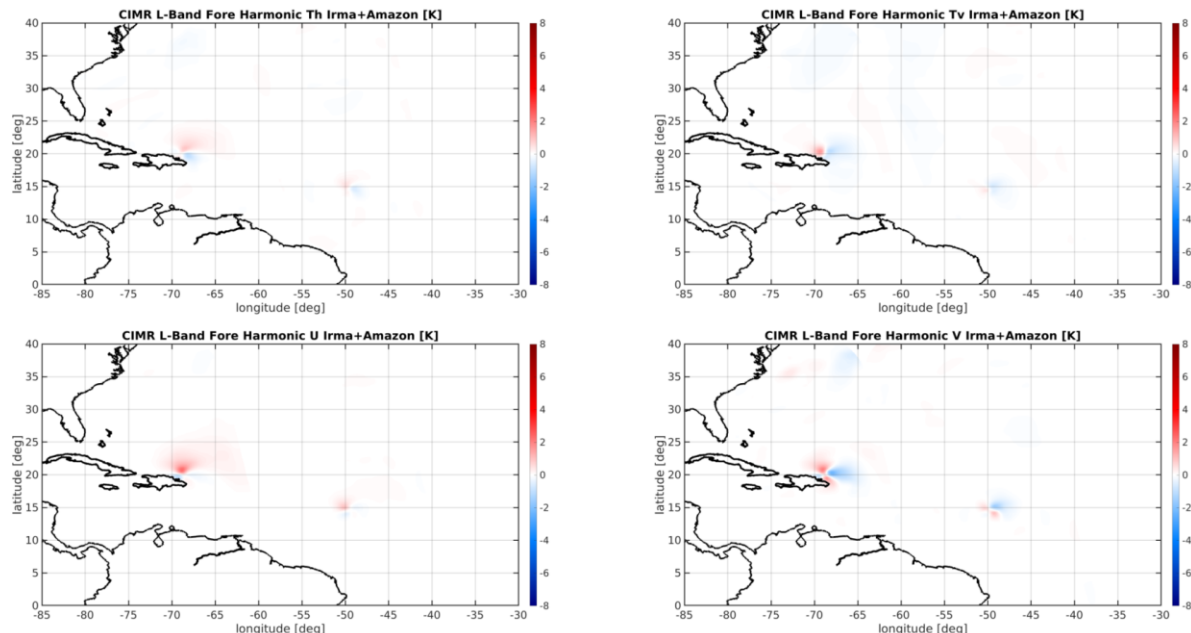


Figure 27: Example of the TOA scene azimuthal harmonics simulated from the surface wind field in Figure 25 for L-band. Panels show (T_h, T_v, U, V).

Here, we specified wind direction-relative harmonics together with the wind direction at each grid point. Note that the harmonics other than 0 cannot vary with incidence angle and are provided as a single value at each horizontal grid point.

9.3 Simulated instrument Tbs over the scene

The computation of (noisy) simulated CIMR antenna temperature from the scene brightness temperature field then involves several aspects:

1. Calculation of orbit and viewing geometry,
2. Calculation of the scene brightness Stokes vector for an ensemble of incidence angles, and of the wind-relative azimuthal harmonics components,
3. Integration of the scene brightness over the antenna patterns (both near and far from the feed boresights),
4. Addition of NEDT noise to the antenna temperatures,
5. Calculation and application of the antenna pattern correction matrices for all feeds.
6. Production of a preliminary version of the Level 1B product,
7. Resampling of the TOA Tbs using Backus-Gilbert for all band except at L-band for which a weighting average is applied.
8. An OZA adjustment is then simply computed by interpolating the test card Tbs (without harmonics) to the reference and actual OZA for each sample/measurement using those values directly without integrating over the antenna pattern. Then, the resampler resamples the interpolated test card Tbs at the OZA values as well as the unadjusted antenna Tbs separately so as to keep track of the adjustment. The OZA correction is then applied after resampling as a simple addition of the resampled adjustment.

Details about each step of the SCEPS simulator can be found in [RD.2]. The simulator includes an orbit propagator to simulate the orbiting satellite positions in time and an antenna geometry routine to simulate the antenna scanning geometry and integrate the brightness fields over the antenna power patterns. Noting that most of the power originates near the feed boresight, the integration domain is divided into an inner and an outer domain. These domains are defined for each feed (see **Figure 28**). The inner domain includes the boresight and extends out to an ellipse corresponding to an azimuthally averaged power 40 dB below the peak (at the feed boresight), where the azimuthal average is computed in the tilted direction cosine coordinate system. The outer domain covers the rest of the Front Half-Space (FHS) of antenna (containing boresight) in either the tilted or un-tilted coordinate system.

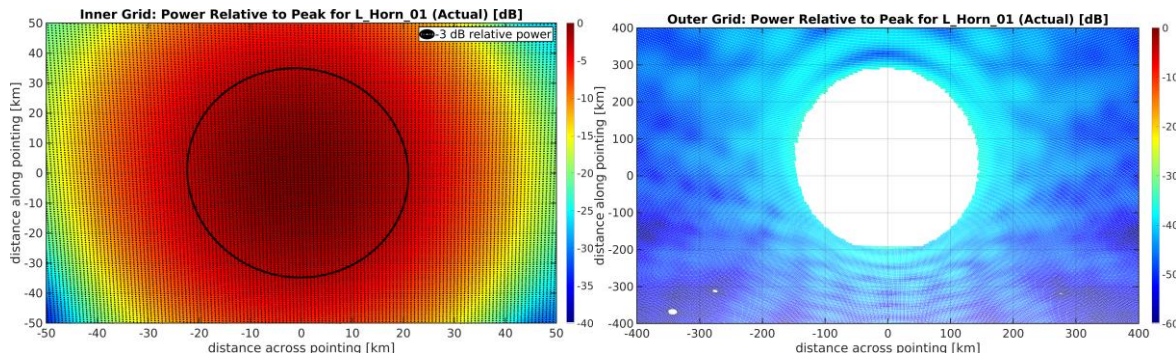


Figure 28: Inner (left) and outer (right) integration grids in untilted director cosine (u, v) coordinates for L-band. Only the directivities down to -40 dB and -60 dB below the peak are shown for the inner and outer grids, respectively. The color indicates the antenna pattern power relative to peak.

The CIMR instrument consists of 25 feeds, with one at L-band, 4 and C/X bands, and 8 at Ku/Ka bands. **Figure 29** shows the measurement (full integration time) footprints for a portion of three successive scans for the L- C-band, X-band and Ku-band horns. The figure illustrates the extent of overlap between successive footprints both along and across scan near the swath center. Although overlap can be increased (at the expense of increased noise) along scan by using individual samples, the across-scan overlap cannot be changed. To obtain a resolution consistent with the antenna pattern footprint size, distance between neighboring measurements should not exceed half the Half-Power Beam Width (by the Whittaker–Nyquist–Shannon sampling theorem). As discussed in [RD.2], this condition is not satisfied across scan in L and Ku bands, but is satisfied in C and X bands. For Ku-band there is no overlap in the half-power footprints across scan, which may be a limiting factor in the resolution of images obtained from resampled antenna temperatures. The figure illustrates the extent of overlap between successive footprints both along and across scan near the swath center. Although overlap can be increased (at the expense of increased noise) along scan by using individual samples, the across-scan overlap cannot be changed.

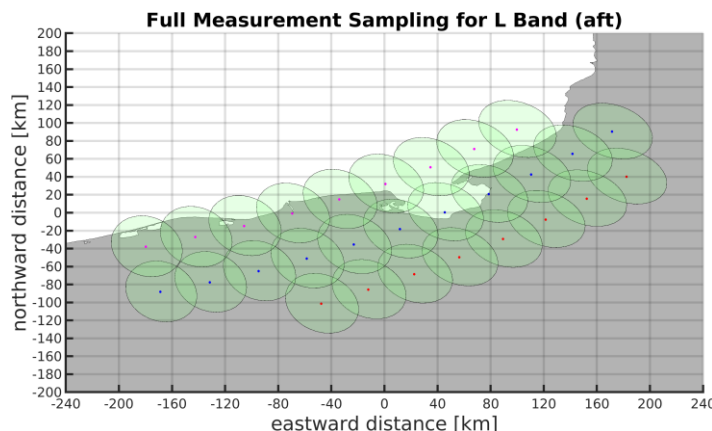


Figure 29: (a): Projection of the L-band feed half-power footprints and boresight locations onto the ground at two closely separated times for three successive scans.

In SCEPS the total antenna temperature integral over all space is separated into several parts, with different integration methods for each:

- the inner domain, extending from each feed boresight out to a circle (in tilted director cosine coordinates) corresponding to an isotropic directivity of -40 dB relative to the maximum at feed center (HBS)
- the outer domain, extending from the boundary of the inner domain out to the earth limb in the untilted frame (OUT)
- the contribution from distributed foreign sources (cold sky and galactic radiation in nominal instrument pointing) (sky),
- the contribution from localized sources (brightspots) in the test card scene (bs), and
- the contribution from the direct sun and moon (without reflection from the earth),

In SCEPS the default reflector rotation rate is set to the fixed value of 7.8 rpm (clockwise looking towards the instrument along the spin axis from behind the reflector) and the radiometer integration times are set to the values shown in Table 5. SCEPS can be configured to produce antenna temperatures for only the full measurements or for all samples. In the present simulation there are five samples per measurement.

Receiver Parameters					
Band Name	Number of feeds	Center frequency (GHz)	Maximum Bandwidth (MHz)	Sample Integration Time (ms)	Measurement NEDT At $T_a = T_{rn} = 150$ K
L	1	1.4135	50.0	11.12	0.3

Table 5: Receiver characteristics. Both the antenna temperature and the effective receiver noise temperature T_{rn} corresponding to the NEDT values are taken to be 150 K in SCEPS. There are five samples per measurement for all bands.

The reflector rotation rate is sufficiently fast that the antenna patterns move substantially during the measurement integration times, and this must be accounted for when SCEPS is configured to compute antenna temperatures for the full measurements. To do so, SCEPS extend the antenna pattern integration to include integration over the integration time of the receiver.

For L-band, one uses a weighted average of the original scene T_{Bs} based on a Gaussian window of FWHM=30 km. Examples of simulated TOA brightness temperatures integrated over CIMR antenna patterns for Aft view of two successive ascending passes intercepting the scene are shown in **Figure 30**.

Note that instrument measurements are simulated from scene T_p using SCEPS with several options:

- ⇒ L1B TOA + NEDT (constant over the antenna pattern),
- ⇒ L1B TOA without NEDT,
- ⇒ L1B TOA integrated over inner antenna patterns (HBS): Boresight to -40 dB,
- ⇒ L1B TOA integrated over full antenna patterns (TOT): 0 dB to -60 dB,
- ⇒ L1B TOA T_p are then remapped into L1C TOA T_p using « gaussian weighted-average » for L-band (do not respect Nyquist sampling)
- ⇒ L1C TOA T_p are then generated for both Aft and Fore views and for 2 ascending passes intercepting the scene.

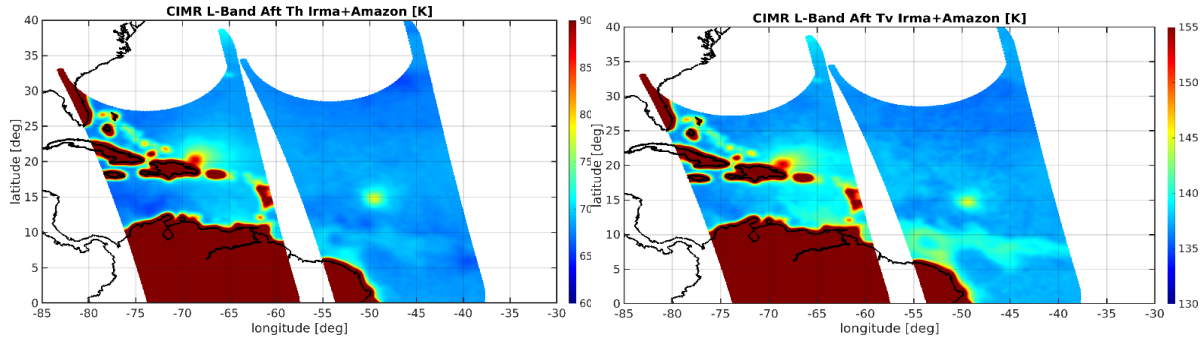
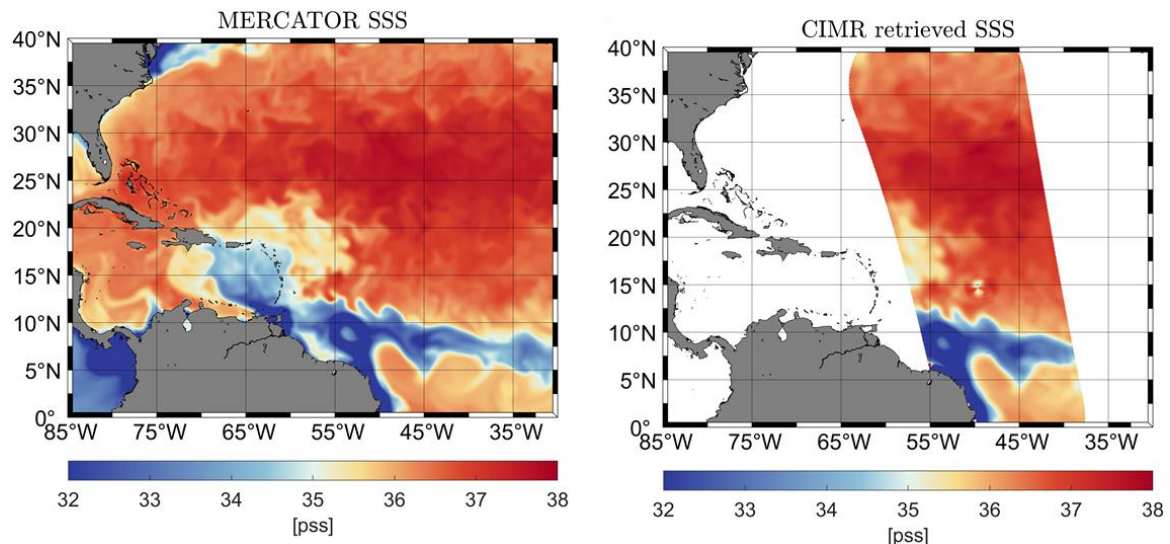


Figure 30: Simulated TOA L-band brightness temperatures integrated over CIMR antenna patterns for Aft view of two successive ascending passes intercepting the scene (left) V-pol; (right) H-pol.

10.4 SSS retrieval simulations

Examples of SSS retrieved over the scene is shown in **Figure 31**. In these retrieval simulations, the instrument Tbs were derived by integrating the scene over the full antenna patterns (HBS+outer patterns). SCEPS provides the option to add NEDT noise to the antenna temperatures: we perform retrieval simulations with and without NEDT, and in the following, we present only results with NEDT. As shown in **Figure 31**, the $\Delta\text{SSS} = \text{SSS}_{\text{retrieved}} - \text{SSS}_{\text{input}}$ fields exhibit high resolution features (North Brazilian current induced SSS fronts and Tropical Cyclone center) which represent area where the retrieved SSS are not well resolved by the ~60 km footprint of CIMR L-band data. The ΔSSS distribution is also skewed with large negative values along the coasts.

We analyzed the ΔSSS as a function of distance to nearest coasts in bins of 10 km. As illustrated in **Figure 32**, a significant fresh bias and increased standard deviation of the ΔSSS is observed when the data are acquired at distance to nearest coasts less than ~70 km.



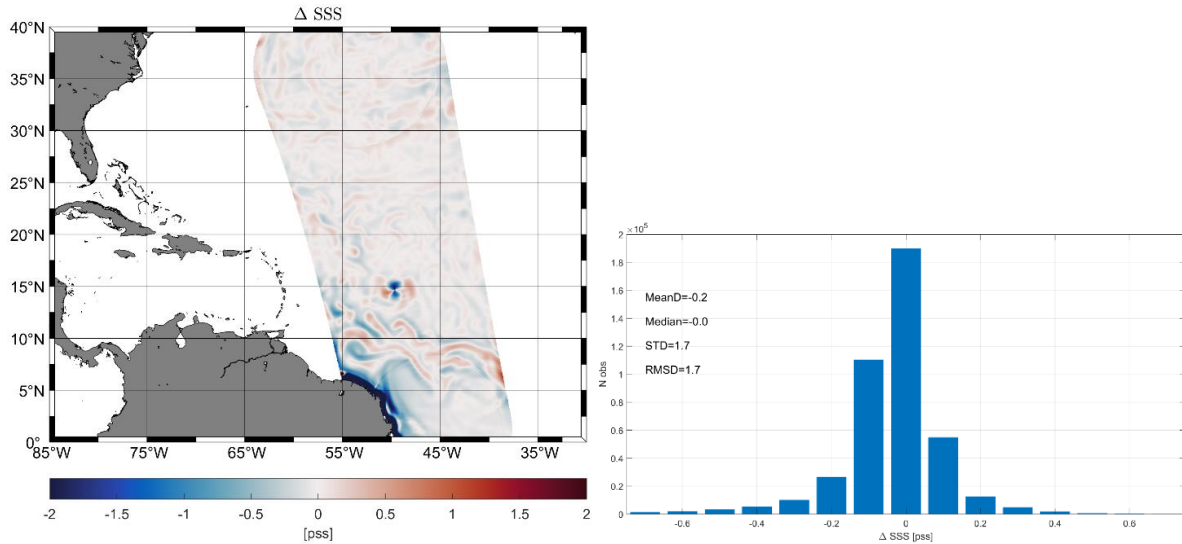


Figure 31: (Top Left) Input 4km resolution SSS field (Top Right) CIMR retrieved SSS from SCEPS generated L1C data. (Bottom Left) Differences between input and retrieved SSS (Bottom Right) Histogram of the differences between input and retrieved SSS.

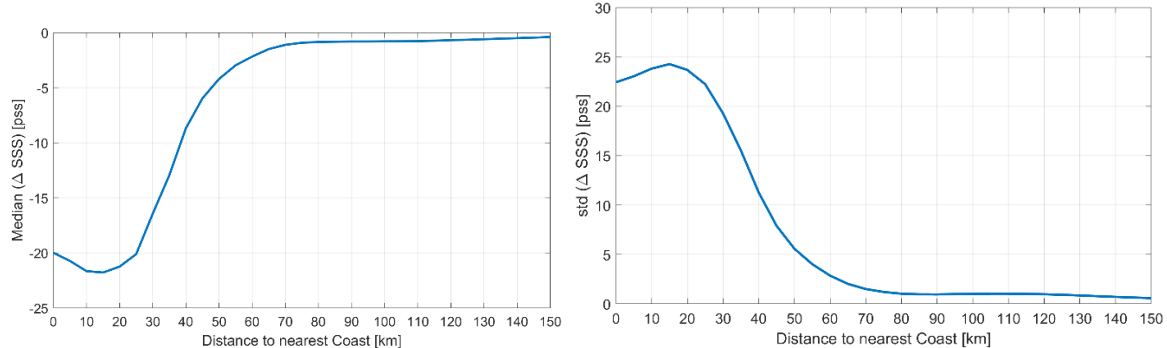


Figure 32: Median (Left) and standard deviation (Right) of the differences between input and retrieved SSS binned as a function of the distance to nearest coasts.

The closer to the coast, the higher the fresh bias and standard deviation of the ΔSSS .

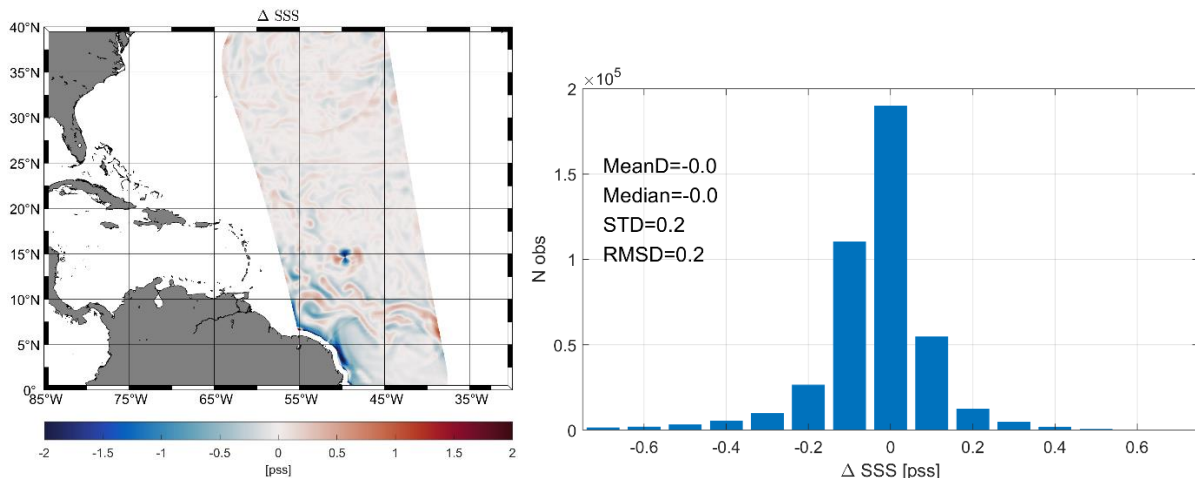


Figure 33: Filtered ΔSSS when data with distance to nearest coasts less than 70 km are removed. The histogram of ΔSSS is shown in the right panel.

While a land-contamination correction will be potentially derived from the future CIMR data (e.g., using the approach of Meissner et al. 2017, 2018), flagging/removing the data within a distance of 70 km from the nearest coasts, will solve most of the land-contamination issues. When removing data within 70 km from the coasts, the statistics of the Δ SSS becomes more gaussian with a significantly reduced STD of ~0.2 pss (see **Figure 33**), compared to ~1.7 pss when considering all data including the SSS retrieved within a band of 70 km from nearest coasts (see **Figure 31**).

10.4 SSS retrieval simulations: comparison with MRD

As stated in the CIMR MRD, the mission objectives for SSS retrieval are the following:

“SEC-OBJ-9. Measure Sea Surface Salinity (SSS) over the global ocean from space [AD-3],[AD-4] with a target gridded spatial resolution of 40 km and uncertainty ≤ 0.3 pss over monthly time-scales [AD-3]”

The accuracy of weekly or monthly SSS products from orbiting satellites depends on the number of satellite passes over a given grid cell within the period of time.

To evaluate such number for the CIMR L-band data collected over one month, in the MACRAD project [RD.3], we have conducted a sampling analysis with the satellite instrument retrieval simulator for the mission: the CIMR SCEPS. We estimated the number of L1B samples per day in $0.36^\circ \times 0.36^\circ$ rectangular grid (~40km resolution) boxes for the complete month of January 2029. We reproduced some of the results herafter.

10.4.1 Error Estimates for individual CIMR L2 SSS

In the following, we first estimated the accuracy of the CIMR satellite L2 SSS measurements from the effects of the various error sources at a nominal incidence angle of 52° that were described in detail in [RD.3]. Table 1 summarizes the influence of various geophysical error sources for four water temperature ranges:

- 1) very low SSTs with $-4^\circ\text{C} \leq T_s < 0^\circ\text{C}$
- 2) Low SSTs: $0^\circ\text{C} \leq T_s < 10^\circ\text{C}$
- 3) Moderate SSTs: $10^\circ\text{C} \leq T_s < 20^\circ\text{C}$
- 4) Warm SSTs: $20^\circ\text{C} \leq T_s < 30^\circ\text{C}$

And for each SST range, we investigated the errors for the three following wind speed range:

- 5) Low wind speed $U_{10} < 5 \text{ m/s}$
- 6) Moderate wind speed $5 \leq U_{10} < 15 \text{ m/s}$
- 7) High wind speed $U_{10} > 15 \text{ m/s}$

In [RD.3], we performed sensitivity analyses from the RTM presented in this ATBD. For each temperature and wind speed range, the estimated brightness temperature errors were listed for T_v , T_h , and $(T_v + T_h)/2$. The estimates for the average brightness temperature $(T_v + T_h)/2$ were included because it is insensitive to the Faraday rotation. We provided the sensitivity of the brightness temperatures to SSS, and SST, indicating a varying degree of sensitivity versus polarization and water temperature, the sensitivity to surface wind speed and direction, respectively. We also estimated the sensitivity to air surface temperature, surface pressure,

columnar water vapor content and cloud liquid water content as well as we provided the residual brightness temperature errors after data corrections or under an assumed threshold for data flag for external sources (galactic and solar glints) and land sea contamination was filtered (e.g., all data within a 70 km band from coasts were not considered). The net effect of geophysical errors is described in **Figure 34** under the assumption that all the geophysical error sources are uncorrelated.

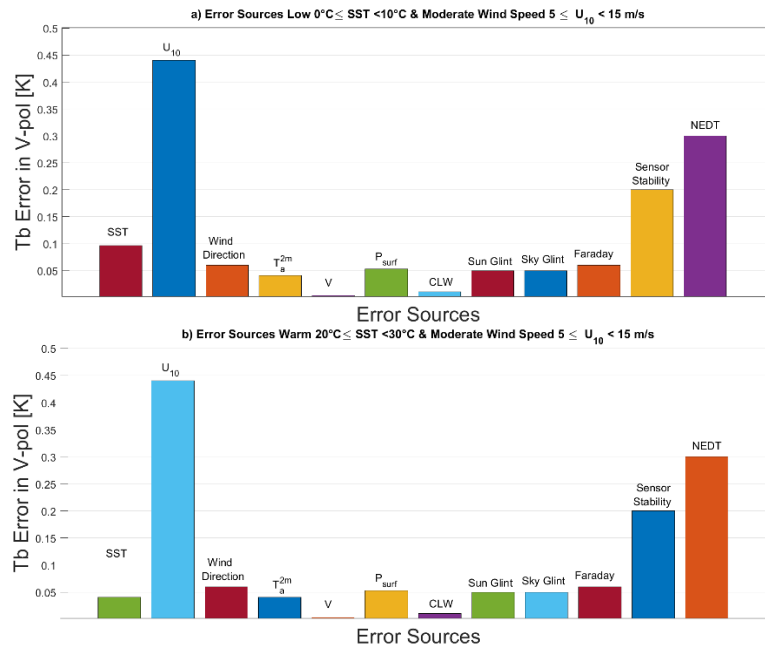
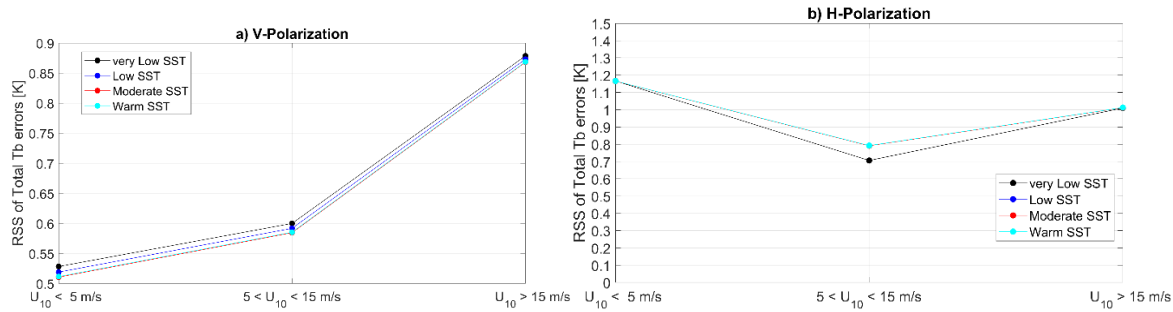


Figure 34: Distribution of uncertainties in the modeling of the V-polarization L-band Tbs at incidence angle of 52° in a) cold sea condition and b) warm sea conditions. The wind speed is moderate with 5 m/s $\leq U_{10} < 15$ m/s.

For individual L-band measurements, the square Root of the Sum of Squares (RSS) of quantity is varying from about 0.5 K to 1.2 K, depending on SST and Wind Speed and on polarization. One of the dominant error sources is the surface roughness (e.g., wind speed). The second most impacting effect is NEDT and radiometer stability. Contrarily to V-polarization (see **Figure 35**), the RSS do not increase monotonically with increasing wind speed for H-polarization because the sensitivity to wind speed is higher for low wind speed than for moderate and higher winds (see **Erreur ! Source du renvoi introuvable.**). As a reference, 0.1 K corresponds to a wind speed uncertainty of 0.5 m/s- for vertical polarization and 0.25 m/s- for horizontal polarization.



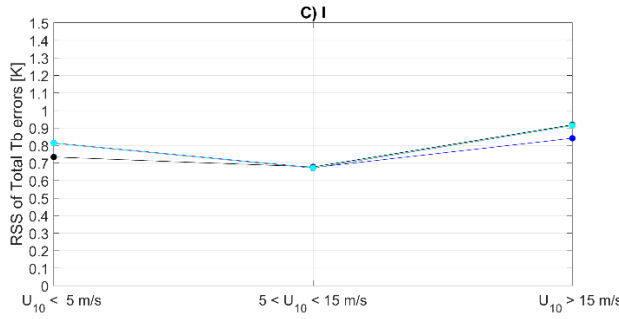


Figure 35: RSS of total Tb errors for a) V-polarization; b) H-polarization and c) First Stokes parameter for the 3 wind speed and 4 SST regimes.

The sensor errors include the calibration errors and the radiometer noise-equivalent-delta-T (NEDT). The instrument calibration stability does not include the bias of the instrument calibration errors, and only accounts for the temporal variability of the instrument calibration. It is assumed that the instrument calibration bias is a constant and hence can be removed by a comparative analysis of in-situ measurements. The dominant errors sources are the antenna pointing angle, antenna emissivities, and the stability of calibration device, such as the noise source, for the electronics. The radiometer NEDT is assumed to be 0.3 K for each polarization

As found, the vertical polarization outperforms the other polarization and combinations because of its superior sensitivity to salinity. In moderate SST and wind conditions, it is about ~1 pss. It increases with increasing wind speed and decreasing SST. The average brightness temperature $(T_v + T_h)/2$ has the advantage of a negligible Faraday rotation error, but its performance is slightly worse than the vertical polarization because of a slight degradation of SSS sensitivity.

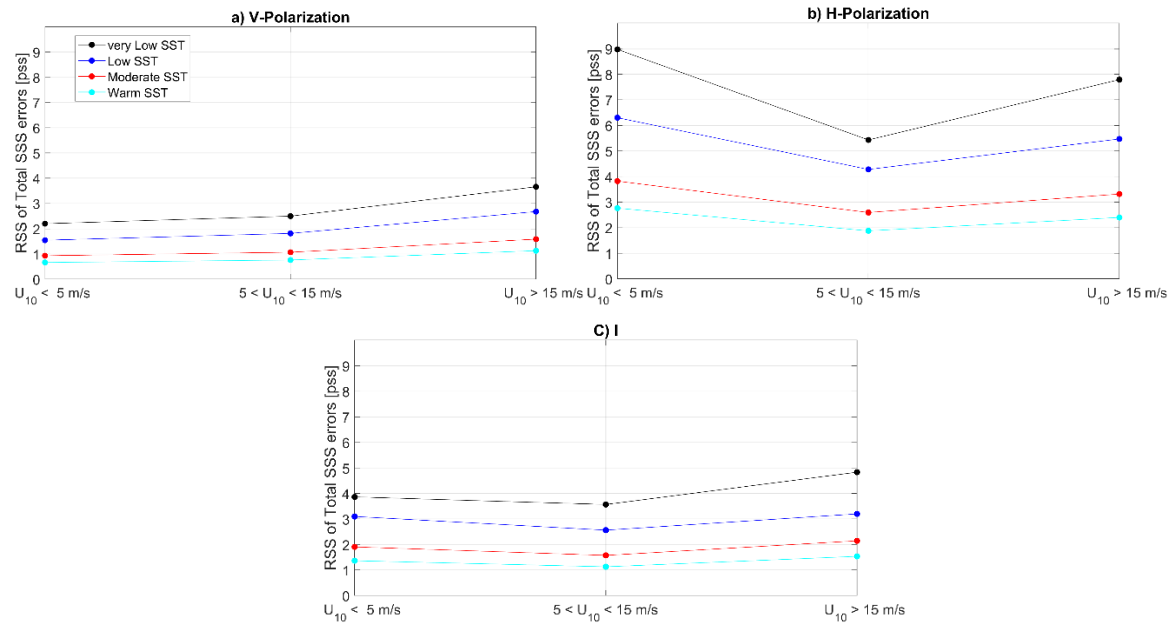


Figure 36: RSS of total SSS errors for a) V-polarization; b) H-polarization and c) First Stokes parameter for the 3 wind speed and 4 SST regimes.

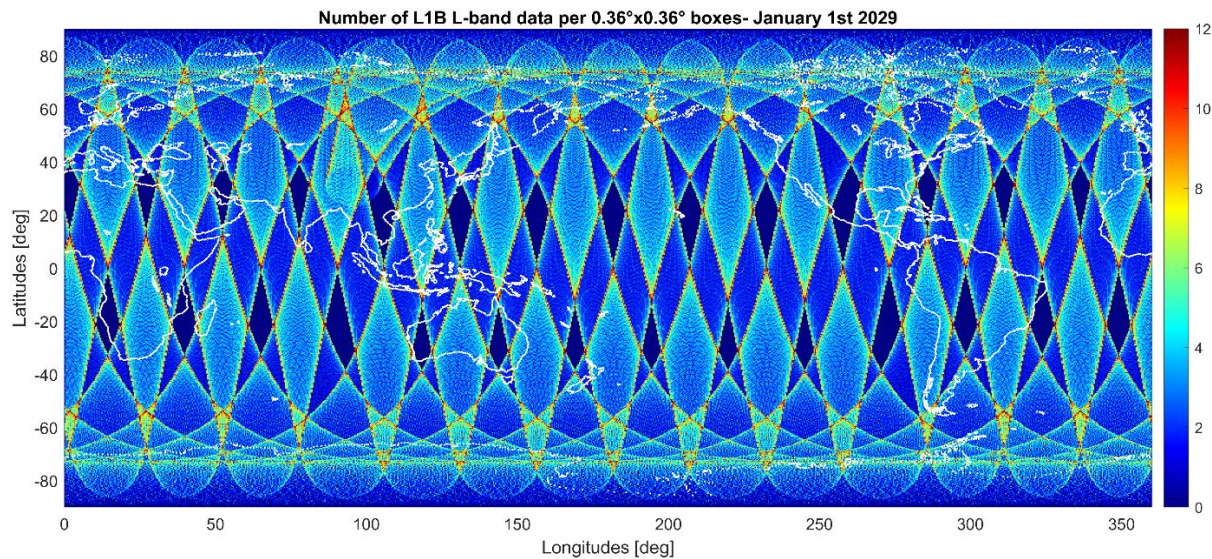
In V-polarization, the accuracy ranges from ~0.9 pss to ~3.5 pss depending on wind speed and SST conditions. In H-pol, it is significantly higher ranging from ~2.5 to 9 pss. The accuracy indicated here is for one satellite observation, and approaches 2 pss (vertical polarization) for

cold waters and improves with increasing water temperatures to reach about 0.9 psu for warm waters.

10.4.2 Error Estimates for Level 3 CIMR SSS

To achieve a better accuracy, multiple independent observations are needed. The independent measurements can possibly result from temporal or spatial averaging. The temporal averaging involves the average of data from multiple satellite passes over a given surface grid cell. The revisit time is a few hours for high latitudes and 1 to 3 days for equatorial regions; therefore, it is reasonable to assume that the data from different satellite passes are uncorrelated. In contrast, the spatial averaging over the measurements from adjacent antenna footprints may not reduce the error because most of the geophysical error sources and instrument calibration uncertainty are likely to have a spatial correlation.

For the CIMR conical scanner, a correlation time of a few minutes for the instrument calibration error will make the measurements across the entire swath and along the track of about 1800 km correlated. The only error source that definitely can be improved by spatial averaging is the sensor NEDT, which is random. To be conservative, we assume only the measurements from different satellite passes as independent estimates. Under this assumption, the number of satellite passes required to reduce the error to 0.3 psu, has been evaluated in [RD.3]. It is about 50 for very cold waters with vertical polarization and diminishes to ~5 for equatorial regions. It is indicated in *Figure 37* and *Figure 38* that one month sampling with the CIMR polar-orbiting L-band instrument results in about 100 passes. This suggests that even during strong sunglint period (when more than 25% of the data might be contaminated in the Northern Hemisphere), a monthly averaged SSS of 0.3 psu is achievable with the vertical polarization data under the assumptions stated above. An average of the SSS estimates from both polarizations should yield better accuracy.



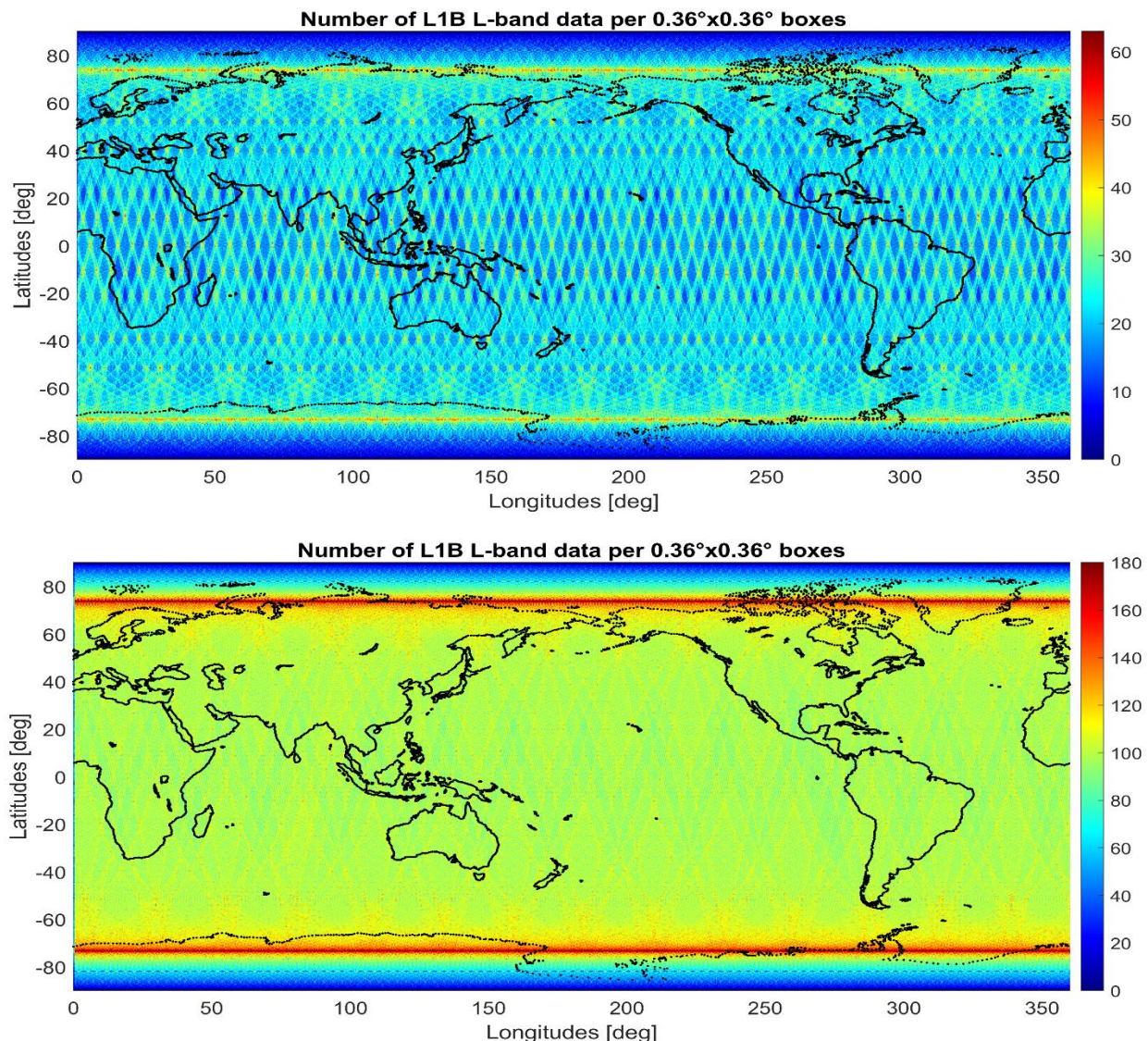


Figure 37: Total number of L-band L1B samples in $0.36^\circ \times 0.36^\circ$ for 1 day (top panel), 1 week (middle panel) and 1 month (bottom panel).

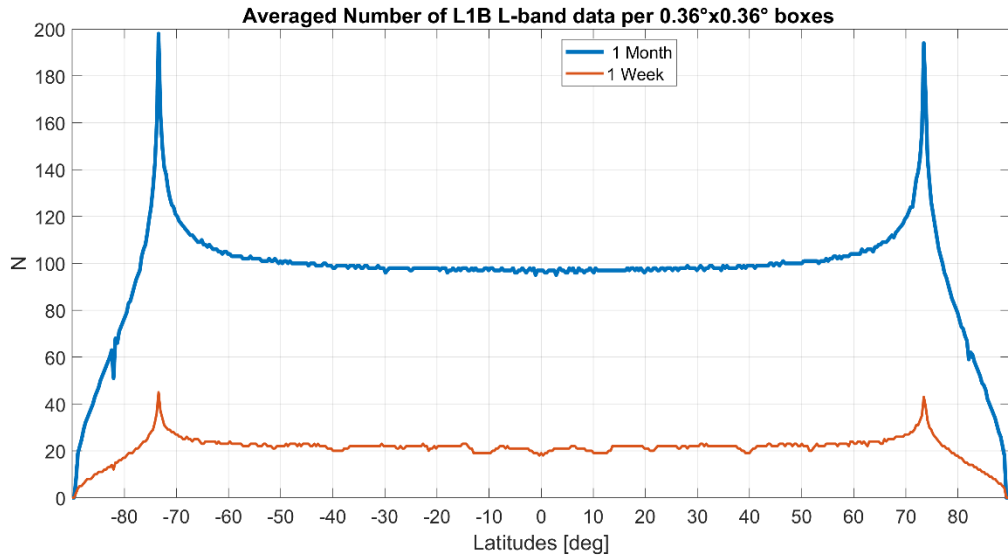


Figure 38: Median number of L-band L1B samples per $0.36^\circ \times 0.36^\circ$ as a function of latitude for 1 week (orange) and 1 month (blue curve).

11. Roadmap for Future CIMR SSS ATBD Developments

The prototype CIMR Level-2 SSS retrieval algorithm presented in this ATBD is based on several assumptions and simplifications. Several developments and improvements to the prototype algorithm are planned which have the potential to significantly improve the performance of the CIMR Level-2 SSS algorithm. We highlight a few of them in this chapter.

11.1 New Sea water dielectric constant model at L-band

At the time this ATBD was developed, two up-to-date parametrizations for the sea water dielectric constant at L-band were available, based on one hand, on the Soil Moisture and Ocean Salinity (SMOS) satellite multi-angular brightness temperature measurements by Boutin et al. (2021) (BV), and, on the other hand, on the new George Washington University laboratory measurements by Zhou et al. (2021) (GW2020). These two approaches are fully independent. For most SSS and Sea Surface Temperature (SST) conditions commonly observed over the open ocean, the relative variations of brightness temperatures Tb simulated through the BV and GW2020 parametrizations agree particularly well, and better than with earlier parametrizations previously used in the SMOS, SMAP, and Aquarius SSS retrievals. Being based purely on Laboratory data, we therefore advise the use of GW2020 in the present ATBD. However, uncertainty remains, especially below 10°C where a ~0.1 K relative difference between the two models is observed. This motivated the development of a revised parameterization, BVZ (Boutin, Vergely, and Zhou (2023)), based on a methodology similar to that used to derive BV but using GW2020 instead of SMOS measurements. Compared to the GW2020 parameterization, BVZ is derived with a reduced number of degrees of freedom, it relies on the TEOS10 PSS78 conductivity-salinity relationship, and on the previously derived static permittivity of fresh water. Noting that this new parametrization significantly improved the SSS retrieval from SMOS in the 5°C–15°C SST range, we advise to update the GW2020 L-band sea water dielectric constant model with this new BVZ model in future algorithm developments for CIMR.

11.2 Incidence angle & SST dependencies of the roughness correction

The wind induced emissivity model is based on the wind emissivity model of the Aquarius V5 release after extrapolating to the CIMR Earth incidence angle. Small adjustment can be applied to the Aquarius V5 model function due to the fact that the ancillary field used to derive the GMF (CIMR L2 OWV) will be slightly different from the Aquarius HHH wind speed which was used in the Aquarius Version 5 algorithm. Small biases will likely exist between these two ancillary wind fields and are dependent on wind speed as well as SST. Because of the high level of accuracy that is required for retrieving salinity, these biases needed to be considered when deriving the wind induced emissivity model function for CIMR using the method outlined in Meissner et al. 2014. As a consequence of the slightly different ancillary wind speed inputs to the Aquarius Version 5 and CIMR salinity retrieval, the geophysical model functions for the wind emissivities shall also differ slightly. This is most important for the wind speed dependence 0th harmonic coefficient of the wind induced emissivity i.e., the isotropic part. Small differences can be expected at very low and at very high wind speeds. In addition, one can expect slight differences in the SST dependence of the wind induced emissivity. All these adjustments shall be done post-launch, once co-localized CIMR L-band Tbs, SSS, SST and wind data sets will be made available. Alternatively, roughness emission

GMFs at 52° can also be directly inferred from SMOS data but at the expense if a higher NEDT in the Tbs.

11.3 Roughness emission azimuthal harmonics in High winds

It remains unclear how the roughness anisotropic emission components (first and second harmonics, see Figure 10 and Figure 11 for all four Stokes parameters behave in high wind speed regimes (say > 20 m/s). Wind-direction signals in passive microwave polarimetry for ocean surfaces under hurricane force winds were however presented in Yueh et al., 2008. They performed analysis of Windsat data for several Atlantic hurricanes from 2003 to 2005. The polarimetric third Stokes parameter observations from the Windsat 10-, 18-, and 37-GHz channels were collocated with the ocean-surface winds from the National Oceanic and Atmospheric Administration Hwind analysis. The collocated data were binned as a function of wind speed and wind direction. The 10-GHz data show clear 4-K peak-to-peak directional signals at 50-60-m/s wind speed after correction for atmospheric attenuation. The signals in the 18- and 37-GHz channels were unclear at above 40-m/s wind speeds, probably caused by the impact of clouds and rain. The data were expanded by sinusoidal series of the relative azimuth angles between the Hwind analysis and observation directions. The coefficients of the sinusoidal series suggest decreasing response to wind direction for increasing wind speed, but the 10-GHz data appear to be fairly constant for up to 50-m/s wind speeds. The trend of the high-wind data (> 25 m/s) is, in general, consistent with the characteristics of the lighter wind data. The combined Windsat-GDAS (< 25 m/s) and Windsat-Hwind (> 25 m/s) analyses show that the amplitude of first-harmonic coefficients (U1) increases with increasing wind speed from low to 20 m/s but then saturates and decreases at higher wind speeds. The amplitude of second harmonic coefficients (U2), having a similar feature, increases with wind speed from light to moderately high wind speed (< 15 m/s) and then displays a decreasing trend beyond about 15–20-m/s wind speeds. This feature is consistent with the active microwave observations of hurricanes. This implies that the ocean waves and other roughness features generated by hurricane force winds will start to lose directionality for increasing wind speed beyond 30–50 m/s. The loss of directionality can be due to a wider azimuthal spreading of wave propagation, increasing coverage of sea foam and spray, and the impact of raindrops on the surface roughness. Excessive attenuation by rain, if undercorrected, may further reduce the directional dependence of U. The ocean waves with longer wavelengths having greater influence on the 10, 6 and 1.4-GHz microwaves probably can sustain better directionality at very high winds than the ocean waves with shorter wavelength, which have greater impact on the 18.7- and 36.5-GHz frequencies. Therefore, in future ATBD developments for CIMR, we suggest to decrease the directional harmonics (1 and 2) towards zero for wind speed higher than 20 m/s.

11.4 Simplified Atmospheric Corrections

Our proposed Atmospheric corrections rely on the vertical integration of the indexes of refraction from local atmospheric parameter profiles. This may be unpractical for an operational processing in terms of computing time. In this case, we suggest to follow the approach used in AMSR-E ATBD (Wentz and Meissner, 2000), where approximated vertically integrated absorption coefficients can be derived from vertically integrated water vapor, cloud liquid water and air temperature. One approximated approach valid at L-band, is to follow the simplified single layer atmospheric model used in

the ESA SMOS Level 2 Ocean Salinity Processor [RD.4], the atmospheric contributions are approximated by the following formulation in which the emission and absorption are expressed purely in terms of air surface temperature T_o , surface pressure P_s , and total column water vapor V . In terms of these quantities, the vertically integrated absorption owing to molecular oxygen and water vapor are, respectively:

$$A_d = A_d^{(u)} = A_d^{(d)} = 10^{-6} \left(C_{ao}^{(0)} + C_{ao}^{(1)} T_o + C_{ao}^{(2)} P_s + C_{ao}^{(3)} T_o^2 + C_{ao}^{(4)} P_s^2 + C_{ao}^{(5)} T_o P_s \right)$$

and

$$A_v = A_v^{(u)} = A_v^{(d)} = 10^{-6} \left(C_{av}^{(0)} + C_{av}^{(1)} P_s + C_{av}^{(2)} V \right)$$

Where the numerical values for coefficients in this mono-layer model are from the papers of Liebe (1989) and of Liebe et al. (1993).

$$\begin{aligned} C_{ao}^{(0)} &= 8033.3 \\ C_{ao}^{(1)} &= -103.999 \\ C_{ao}^{(2)} &= 28.2992 \\ C_{ao}^{(3)} &= 0.2626 \\ C_{ao}^{(4)} &= 0.0064 \\ C_{ao}^{(5)} &= -0.0942 \end{aligned} \quad \text{and} \quad \begin{aligned} C_{av}^{(0)} &= -151.7150 \\ C_{av}^{(1)} &= 0.1554 \\ C_{av}^{(2)} &= 3.5406 \end{aligned}$$

The corresponding 1-way atmospheric transmittances associated with molecular oxygen absorption and water vapor along a line of sight at angle θ_s from nadir are:

$$\begin{aligned} \tau_d &= \exp[-A_d \sec \theta_s] \\ \tau_v &= \exp[-A_v \sec \theta_s] \end{aligned}$$

with this formulation, the surface brightness temperature after passage through the atmosphere T'_B is related to the unattenuated brightness temperature T_B by:

$$T'_B = (\tau_d \tau_v) T_B$$

The upwelling and downwelling atmospheric emission are assumed to be equal and take the following form at nadir for the oxygen and water vapor contributions, respectively:

$$T_{bad} = A_d \left[T_o - C_{ao}^{(0)} - C_{ao}^{(1)} T_o - C_{ao}^{(2)} P_s - C_{ao}^{(3)} T_o^2 - C_{ao}^{(4)} P_s^2 - C_{ao}^{(5)} T_o P_s \right]$$

and

$$T_{bav} = A_v \left[T_o - C_{av}^{(0)} - C_{av}^{(1)} P_s - C_{av}^{(2)} V \right]$$

where:

$$\begin{aligned}
 C_{aeo}^{(0)} &= -0.7789 \\
 C_{aeo}^{(1)} &= 0.1376 \\
 C_{aeo}^{(2)} &= -0.0011 \\
 C_{aeo}^{(3)} &= -1.1578 \times 10^{-4} \\
 C_{aeo}^{(4)} &= 1.2847 \times 10^{-6} \\
 C_{aeo}^{(5)} &= -1.1133 \times 10^{-5}
 \end{aligned}
 \quad \text{and} \quad
 \begin{aligned}
 C_{aev}^{(0)} &= 8.1637 \\
 C_{aev}^{(1)} &= 2.4235 \times 10^{-4} \\
 C_{aev}^{(2)} &= 0.0337
 \end{aligned}$$

and the total atmospheric emission brightness temperature at nadir (unpolarized) is:

$$T_{ea} = T_{bad} + T_{bav}$$

Along a path at angle θ_s from nadir, the unpolarized brightness temperature of atmospheric 1-way emission is:

$$T_{ea}(\theta_s) = \sec \theta_s [T_{bad} + T_{bav}]$$

As discussed in [RD.4], for sea scenes, the required accuracy is better than 0.05 K and this could be achieved using the same formulas but restricting the surface pressure range to [900 1100] hPa. The method selected for computing gaseous radiative contributions has to be selected in such a way that the resulting error on upwelling brightness temperatures due to approximating the effect of physical atmospheric properties (pressure, temperature, water vapor concentration) never exceeds 0.05 K for CIMR operating conditions. It is expected that this goal is compatible with computing power/time requirements. Then, the major error source will be due to estimates of absorption cross sections, which in turn reflect the uncertainty on spectroscopic measurements. This uncertainty is estimated around 5%.

11.5 Needed and missing correction: retrieval in coastal areas and closer to the sea ice edge

The improved resolution of CIMR and stringent beam forming (“distance-to-coast”) requirements mean that Level-2 SSS retrievals can be achieved closer to the coastline. Still, coastal regions and water bodies will be challenging for the CIMR Level-2 products when the main beam overlaps different surface types. This can lead to erroneous coastal SSS as demonstrated in the performance assessments. Similar challenges exist for retrieval of SSS close to the sea-ice edge. Application of a land-spill over correction and methods for mitigating land contamination [Olmedo et al., 2017, Olmedo et al., 2018] should be investigated, as well as methods to reduce sea-ice contamination [Meissner and Manaster, 2021]. It is not fully clear yet at which processing level (1) or (2) the land- and ice-ocean transitions effects shall be corrected for on the T_{bs} (so called land sea contamination). Given that these effects require antenna-pattern -related information, it shall better be applied in the Level 1 algorithms.

11.6 SSS uncertainty estimation

A detailed analysis of various geophysical error sources that influence the microwave remote sensing of ocean surface salinity with CIMR sensor has been performed in [RD.3]. The error

sources include the sea surface temperature, sea surface roughness, atmospheric gases, ionospheric Faraday rotation, solar and galactic emission sources, as well as the brightness temperature contamination at the land-sea or the sea ice -open ocean transitions. Using the SSS retrieval algorithm developed in this document sensitivity analyses for each of the previous potential error sources for the L2 SSS retrievals were performed. Many of them are shown to have an influence of a few Kelvin, which are not negligible compared with the sensitivity of L-band sea surface brightness temperatures to salinity. An accurate knowledge of these parameters is necessary to enable a correction of the microwave measurements to accurately measure SSS. While uncertainty estimate, shall be part of the output product, we have not yet included it into the algorithm. In [RD3], the method we used for formally assessing random and systematic uncertainties in the CIMR SSS retrievals was presented. The method is based on performing multiple retrievals by perturbing the various inputs to the retrieval algorithm and calculating the sensitivity of the CIMR retrieved SSS to these inputs. Together with an error model for the uncertainties in the input parameters it is possible to calculate the uncertainty in the retrieved salinity. Such approach can be used to partition the retrieval errors in different classes of geophysical conditions (cold to warm SSTs, low to high winds etc..). As found, for individual L-band measurements far away from coasts or ice-edges (> 70 kms), the square Root of the Sum of Squares (RSS) of quantity is varying from about 0.5 K to 1.2 K, depending on SST and Wind Speed and on polarization. As found, an accuracy of 0.3 pss is achievable for a monthly average gridded data set for CIMR polar-orbiting satellite with a swath width of ~ 1800 km. Two key factors to enable the accuracy of satellite measurements is a precise evaluation of the wind speed within the L-band footprint and the stability of the instrument or calibration device. The instrument has to be calibrated to an accuracy of better than 0.2 K in terms of temporal variability. This level of precision is believed to be achievable, but does represent an implementation challenge. Extreme care has to be taken for the sensor design and development.

12. References

1

G. Siedler, J. Church, and J. Gould. *Ocean Circulation and Climate: Observing and Modelling the Global Ocean*. Academic Press, London, 2001.

2

G. Wust. *Oberflächensalzgehalt, Verdunstung und Niederschlag auf dem Weltmeere*, pages 347–359. Landerkundliche Forschung, Festschrift Norbert Krebs, 1936.

3

R. W. Schmitt. Salinity and the global water cycle. *Oceanography*, 21(1):12–19, 2008.
URL: <https://www.jstor.org/stable/24860148> (visited on 2022-11-30).

4

Paul J. Durack, Susan E. Wijffels, and Richard J. Matear. Ocean salinities reveal strong global water cycle intensification during 1950 to 2000. *Science*, 336(6080):455–458, 2012.
URL: <https://www.science.org/doi/abs/10.1126/science.1212222>, arXiv:<https://www.science.org/doi/pdf/10.1126/science.1212222>, doi:10.1126/science.1212222.

5

Nikolaos Skliris, Robert Marsh, Simon A. Josey, Simon A. Good, Chunlei Liu, and Richard P. Allan. Salinity changes in the world ocean since 1950 in relation to changing surface freshwater fluxes. *Climate Dynamics*, 43(3-4):709–736, August 2014.
URL: <https://eprints.soton.ac.uk/365182/>.

6

Jan D. Zika, Nikolaos Skliris, A. J. George Nurser, Simon A. Josey, Lawrence Mudryk, Frédéric Laliberté, and Robert Marsh. Maintenance and broadening of the ocean's salinity distribution by the water cycle. *Journal of Climate*, 28(24):9550 – 9560, 2015.
URL: <https://journals.ametsoc.org/view/journals/clim/28/24/jcli-d-15-0273.1.xml>, doi:10.1175/JCLI-D-15-0273.1.

7

Peter E. Land, Jamie D. Shutler, Helen S. Findlay, Fanny Girard-Ardhuin, Roberto Sabia, Nicolas Reul, Jean-Francois Piolle, Bertrand Chapron, Yves Quilfen, Joseph Salisbury, Douglas Vandemark, Richard Bellerby, and Punyasloke Bhadury. Salinity from space unlocks satellite-based assessment of ocean acidification. *Environmental Science & Technology*, 49(4):1987–1994, 2015. PMID: 25569587.
URL: <https://doi.org/10.1021/es504849s>, arXiv:<https://doi.org/10.1021/es504849s>, doi:10.1021/es504849s.

8

Rana A. Fine, Debra A. Willey, and Frank J. Millero. Global variability and changes in ocean total alkalinity from aquarius satellite data. *Geophysical Research Letters*, 44(1):261–267, 2017.
URL: <https://agupubs.onlinelibrary.wiley.com/doi/abs/10.1002/2016GL071712>, arX

iv:<https://agupubs.onlinelibrary.wiley.com/doi/pdf/10.1002/2016GL071712>, doi:<https://doi.org/10.1002/2016GL071712>.

9

Roger Lukas and Eric Lindstrom. The mixed layer of the western equatorial pacific ocean. *Journal of Geophysical Research: Oceans*, 96(S01):3343–3357, 1991. URL: <https://agupubs.onlinelibrary.wiley.com/doi/abs/10.1029/90JC01951>, arXiv:<https://agupubs.onlinelibrary.wiley.com/doi/pdf/10.1029/90JC01951>, doi:<https://doi.org/10.1029/90JC01951>.

10

K. Balaguru, P. Chang, R. Saravanan, L. R. Leung, Z. Xu, M. Li, and J.-S. Hsieh. Ocean barrier layers' effect on tropical cyclone intensification. *Proc. Natl. Acad. Sci. U.S.A.*, 109(36):14343–14347, August 2012. URL: <http://dx.doi.org/10.1073/pnas.1201364109>, doi:<10.1073/pnas.1201364109>.

11

Frederick M. Bingham, Stephan D. Howden, and Chester J. Koblinsky. Sea surface salinity measurements in the historical database. *J. Geophys. Res.*, 107(C12):8019, 2002. doi:<10.1029/2000JC000767>.

12

Giulio Notarstefano. Argo float data and metadata from global data assembly centre (argo gdac). Technical Report, IFREMER, SEANOE, 2022. doi:<https://doi.org/10.17882/42182>.

13

Gaël Alory, T. Delcroix, P. Téchiné, D. Diverrès, D. Varillon, S. Cravatte, Y. Gouriou, J. Grelet, S. Jacquin, E. Kestenare, and et al. The French contribution to the voluntary observing ships network of sea surface salinity. *Deep-Sea Res. Pt. I*, 105:1–18, November 2015.

URL: <http://dx.doi.org/10.1016/j.dsr.2015.08.005>.

14

SR Smith, JJ Rolph, K Briggs, and MA Bourassa. Quality-controlled underway oceanographic and meteorological data from the center for ocean-atmospheric predictions center (coaps)-shipboard automated meteorological and oceanographic system (samos). *Asheville, NC: NOAA National Centers for Environmental Information. Dataset*, doi, 10:V5QJ7F8R, 2009.

15

J. Font, G. S. E. Lagerloef, D. M. Le Vine, A. Camps, and O. -Z. Zanife. The determination of surface salinity with the European SMOS space mission. *IEEE Trans. Geosci. Remote Sens.*, 42(10):2196–2205, Oct. 2004. doi:<10.1109/TGRS.2004.834649>.

16

G. S. E. Lagerloef, C. Swift, and D. Le Vine. Sea surface salinity: The next remote sensing challenge. *Oceanography*, 8(2):44–50, 1995.

17

JD Droppleman, RA Mennella, and DE Evans. An airborne measurement of the salinity variations of the mississippi river outflow. *Journal of Geophysical Research*, 75(30):5909–5913, 1970.

18

C. T. Swift. Microwave radiometer measurements of the Cape Code Canal. *Radio Sci.*, 9(7):641–653, 1974.

19

R. M. Lerner and J. P. Hollinger. Analysis of 1.4 GHz Radiometric measurements from Skylab. *Remote Sens. Environ.*, 6(4):251–269, January 1977. URL: <http://linkinghub.elsevier.com/retrieve/pii/0034425777900475>, doi:10.1016/0034-4257(77)90047-5.

20

V Sironian. Effect of temperature, angle of observation, salinity, and thin ice on the microwave emission of water. *Journal of Geophysical Research*, 73(14):4481–4486, 1968.

21

Jack F Paris. Microwave radiometry and its application to marine meteorology and oceanography. Technical Report, TEXAS A AND M UNIV COLLEGE STATION DEPT OF OCEANOGRAPHY, 1969.

22

James P Hollinger. Passive microwave measurements of sea surface roughness. *IEEE Transactions on Geoscience Electronics*, 9(3):165–169, 1971.

23

Gary C Thomann. Experimental results of the remote sensing of sea-surface salinity at 21-cm wavelength. *IEEE Transactions on Geoscience Electronics*, 14(3):198–214, 1976.

24

Mark A Goodberlet, Calvin T Swift, Kevin P Kiley, Jerry L Miller, and James B Zaitzeff. Microwave remote sensing of coastal zone salinity. *Journal of coastal research*, pages 363–372, 1997.

25

Hans-Juergen C Blume, Bruce M Kendall, and John C Fedors. Measurement of ocean temperature and salinity via microwave radiometry. *Boundary-Layer Meteorology*, 13(1):295–308, 1978.

26

Hans-Juergen C Blume and Bruce M Kendall. Passive microwave measurements of temperature and salinity in coastal zones. *IEEE Transactions on Geoscience and Remote Sensing*, pages 394–404, 1982.

27

Bruce M Kendall and JO Blanton. Microwave radiometer measurement of tidally induced salinity changes off the georgia coast. *Journal of Geophysical Research: Oceans*, 86(C7):6435–6441, 1981.

28

A Stogryn. Equations for calculating the dielectric constant of saline water (correspondence). *IEEE transactions on microwave theory and Techniques*, 19(8):733–736, 1971.

29

L. A. Klein and C. T. Swift. An improved model for the dielectric constant of sea water at microwave frequencies. *IEEE Trans. Antennas Propag.*, 25(1):104–111, January 1977. [doi:10.1109/TAP.1977.1141539](https://doi.org/10.1109/TAP.1977.1141539).

30

A Shutko, B Liberman, and G Chuhray. On the influence of dielectric property variations on the microwave radiation of a water surface. *IEEE Journal of Oceanic Engineering*, 7(1):35–39, 1982.

31

William J Webster Jr, Thomas T Wilheit, Duncan B Ross, and Per Gloersen. Spectral characteristics of the microwave emission from a wind-driven foam-covered sea. *Journal of Geophysical Research*, 81(18):3095–3099, 1976.

32

Calvin T Swift and Robert E McIntosh. Considerations for microwave remote sensing of ocean-surface salinity. *IEEE Transactions on Geoscience and Remote Sensing*, pages 480–491, 1983.

33

David M Le Vine, Michael Kao, Alan B Tanner, Calvin T Swift, and Andrew Griffis. Initial results in the development of a synthetic aperture microwave radiometer. *IEEE Transactions on Geoscience and Remote Sensing*, 28:614–619, 1990.

34

DM Le Vine, M Kao, RW Garvine, and T Sanders. Remote sensing of ocean salinity: results from the delaware coastal current experiment. *Journal of Atmospheric and Oceanic Technology*, 15(6):1478–1484, 1998.

35

MA Goodberlet and CT Swift. A remote sensing system for measuring estuarine and coastal ocean surface salinity. *Quadrant Eng., Hadley, MA, Progress Rep*, 1993.

36

Ian Stuart Robinson. *Satellite oceanography; an introduction for oceanographers and remote-sensing scientists*. Chichester (UK) Horwood, 1985.

37

Jerry L Miller, Mark A Goodberlet, and James B Zaitzeff. Airborne salinity mapper makes debut in coastal zone. *Eos, Transactions American Geophysical Union*, 79(14):173–177, 1998.

38

DM Burrage, ML Heron, JM Hacker, Jorg L Miller, TC Stieglitz, Craig R Steinberg, and A Prytz. Structure and influence of tropical river plumes in the great barrier reef:

application and performance of an airborne sea surface salinity mapping system. *Remote Sensing of Environment*, 85(2):204–220, 2003.

39

Jerry L Miller* and Mark Goodberlet. Development and applications of starrs: a next generation airborne salinity imager. *International Journal of Remote Sensing*, 25(7-8):1319–1324, 2004.

40

Tabare Perez, Joel C Wesson, and Derek Burrage. Airborne remote sensing of the plata plume using starrs. Technical Report, NAVAL RESEARCH LAB STENNIS SPACE CENTER MS OCEANOGRAPHY DIV, 2006.

41

Victor Klemas. Remote sensing of sea surface salinity: an overview with case studies. *Journal of Coastal Research*, 27(5):830–838, 2011.

42

William J Wilson, Simon H Yueh, Steve Dinardo, Yi Chao, and Fuk Li. Precision ocean salinity measurements using the passive active l/s-band aircraft instrument. In *IGARSS 2003. 2003 IEEE International Geoscience and Remote Sensing Symposium. Proceedings (IEEE Cat. No. 03CH37477)*, volume 4, 2792–2794. IEEE, 2003.

43

Simon H Yueh, Richard West, William J Wilson, Fuk K Li, Eni G Njoku, and Yahya Rahmat-Samii. Error sources and feasibility for microwave remote sensing of ocean surface salinity. *IEEE Transactions on Geoscience and Remote Sensing*, 39(5):1049–1060, 2001.

44

JM Goutoule, E Anterrieu, YH Kerr, A Lannes, and N Skou. Miras microwave radiometry critical technical development. *TOULOUSE, MMS*, 1996.

45

Franck Bayle, J-P Wigneron, Yann H Kerr, Philippe Waldteufel, Eric Anterrieu, J-C Orlhac, Andre Chanzy, Olivier Marloie, Marc Bernardini, Sten Sobjaerg, and others. Two-dimensional synthetic aperture images over a land surface scene. *IEEE Transactions on Geoscience and Remote Sensing*, 40(3):710–714, 2002.

46

Roger Lang, Yiwen Zhou, Cuneyt Utku, and David Le Vine. Accurate measurements of the dielectric constant of seawater at l band. *Radio Science*, 51(1):2–24, 2016.

47

Peter Josef William Debye. *Polar molecules*. Dover publications, 1929.

48

AP Stogryn, HT Bull, K Rubayi, and S Iravanchy. The microwave permittivity of sea and fresh water. *GenCorp Aerojet, Azusa, CA*, 1995.

49

W. Ellison, A. Balana, G. Delbos, K. Lamkaouchi, L. Eymard, C. Guillou, and C. Prigent. New permittivity measurements of sea water. *Radio Sci.*, 33(3):639–648, 1998. [doi:10.1029/97RS02223](https://doi.org/10.1029/97RS02223).

50

W Ho and WF Hall. Measurements of the dielectric properties of seawater and nacl solutions at 2.65 ghz. *Journal of Geophysical Research*, 78(27):6301–6315, 1973.

51

WW Ho, AW Love, and MJ VanMelle. Measurements of the dielectric properties of sea water at 1.43 ghz. Technical Report, NASA, 1974.

52

Thomas Meissner and Frank J Wentz. The complex dielectric constant of pure and sea water from microwave satellite observations. *IEEE Transactions on Geoscience and Remote Sensing*, 42(9):1836–1849, 2004.

53

Thomas Meissner and Frank J Wentz. The emissivity of the ocean surface between 6 and 90 ghz over a large range of wind speeds and earth incidence angles. *IEEE Transactions on Geoscience and Remote Sensing*, 50(8):3004–3026, 2012.

54

Thomas Meissner, Frank J Wentz, and Lucrezia Ricciardulli. The emission and scattering of l-band microwave radiation from rough ocean surfaces and wind speed measurements from the aquarius sensor. *Journal of Geophysical Research: Oceans*, 119(9):6499–6522, 2014.

55

A. Camps, J. Font, M. Vall-llossera, C. Gabarró, I. Corbella, N. Duffo, F. Torres, S. Blanch, A. Aguasca, R. Villarino, L. Enrique, J. J. Miranda, J. J. Arenas, A. Julià, J. Etcheto, V. Caselles, A. Weill, J. Boutin, S. Contardo, R. Niclós, R. Rivas, S. C. Reising, P. Wurteleisen, M. Berger, and M. Martín-Neira. The WISE 2000 and 2001 Field Experiments in Support of the SMOS Mission: Sea Surface L-band Brightness Temperature Observations and their Application to Multi-Angular Salinity Retrieval. *IEEE Trans. Geosci. Remote Sens.*, 42(4):804–823, 2004. [doi:10.1109/TGRS.2003.819444](https://doi.org/10.1109/TGRS.2003.819444).

56

W. J. Wilson, S. H. Yueh, S. J. Dinardo, and F. K. Li. High-stability L-band radiometer measurements of saltwater. *IEEE Trans. Geosci. Remote Sens.*, 42(9):1829–1835, 2004. [doi:10.1109/TGRS.2004.833393](https://doi.org/10.1109/TGRS.2004.833393).

57

Sebastián Blanch and Albert Aguasca. Seawater dielectric permittivity model from measurements at 1 band. In *IGARSS 2004. 2004 IEEE International Geoscience and Remote Sensing Symposium*, volume 2, 1362–1365. IEEE, 2004.

58

SMOS Team and others. Smos l2 os algorithm theoretical baseline document so-tn-arg-gs-0007. 2016.

59

Thomas Meissner, Frank J Wentz, and David M LeVine. The salinity retrieval algorithms for the nasa aquarius version 5 and smap version 3 releases. *Remote Sensing*, 10(7):1121, 2018.

60

Emmanuel P Dinnat, Jacqueline Boutin, Xiaobin Yin, and David M Le Vine. Inter-comparison of smos and aquarius sea surface salinity: effects of the dielectric constant and vicarious calibration. In *2014 13th Specialist Meeting on Microwave Radiometry and Remote Sensing of the Environment (MicroRad)*, 55–60. IEEE, 2014.

61

Yiwen Zhou, Roger H Lang, Emmanuel P Dinnat, and David M Le Vine. L-band model function of the dielectric constant of seawater. *IEEE Transactions on Geoscience and Remote Sensing*, 55(12):6964–6974, 2017.

62

Jacqueline Boutin, Jean-Luc Vergely, Emmanuel P. Dinnat, Philippe Waldteufel, Francesco D'Amico, Nicolas Reul, Alexandre Supply, and Clovis Thouvenin-Masson. Correcting sea surface temperature spurious effects in salinity retrieved from spaceborne l-band radiometer measurements. *IEEE Transactions on Geoscience and Remote Sensing*, 59(9):7256–7269, 2021. [doi:10.1109/TGRS.2020.3030488](https://doi.org/10.1109/TGRS.2020.3030488).

63

Yiwen Zhou, Roger H Lang, Emmanuel P Dinnat, and David M Le Vine. Seawater debye model function at l-band and its impact on salinity retrieval from aquarius satellite data. *IEEE Transactions on Geoscience and Remote Sensing*, 59(10):8103–8116, 2021.

64

David M. Le Vine, Roger H. Lang, Yiwen Zhou, Emmanuel P. Dinnat, and Thomas Meissner. Status of the dielectric constant of sea water at l-band for remote sensing of salinity. *IEEE Transactions on Geoscience and Remote Sensing*, 60():1–14, 2022. [doi:10.1109/TGRS.2022.3207944](https://doi.org/10.1109/TGRS.2022.3207944).

65

Xiaobin Yin, Jacqueline Boutin, Emmanuel Dinnat, Qingtao Song, and Adrien Martin. Roughness and foam signature on smos-miras brightness temperatures: a semi-theoretical approach. *Remote sensing of environment*, 180:221–233, 2016.

66

Simon Yueh, Wenqing Tang, Alexander Fore, Akiko Hayashi, Yuhe T Song, and Gary Lagerloef. Aquarius geophysical model function and combined active passive algorithm for ocean surface salinity and wind retrieval. *Journal of Geophysical Research: Oceans*, 119(8):5360–5379, 2014.

67

Alexander G. Fore, Simon H. Yueh, Wenqing Tang, Bryan W. Stiles, and Akiko K. Hayashi. Combined active/passive retrievals of ocean vector wind and sea surface salinity with smap. *IEEE Transactions on Geoscience and Remote Sensing*, 54(12):7396–7404, 2016. [doi:10.1109/TGRS.2016.2601486](https://doi.org/10.1109/TGRS.2016.2601486).

68

S. H. Yueh. Modeling of wind direction signals in polarimetric sea surface brightness temperatures. *IEEE Trans. Geosci. Remote Sens.*, 35(6):1400–1418, November 1997.

69

Simon H. Yueh, Ronald Kwok, and Son V. Nghiem. Polarimetric scattering and emission properties of targets with reflection symmetry. *Radio Sci.*, 29(6):1409–1420, Nov-Dec 1994.

70

S. H. Yueh, W. J. Wilson, S. J. Dinardo, and F. K. Li. Polarimetric microwave brightness signatures of ocean wind directions. *IEEE Trans. Geosci. Remote Sens.*, 37(2):949–959, mar 1999.
URL: <http://dx.doi.org/10.1109/36.752213>, doi:[10.1109/36.752213](http://dx.doi.org/10.1109/36.752213).

71

Joel T. Johnson. An Efficient Two-Scale Model for the Computation of Thermal Emission and Atmospheric Reflection from the Sea Surface. *IEEE Trans. Geosci. Remote Sens.*, 44(3):560–568, March 2006. doi:[10.1109/TGRS.2005.855999](https://doi.org/10.1109/TGRS.2005.855999).

72

Wentao Ma, Yanlei Du, Guihong Liu, Yang Yu, Xiaofeng Yang, Jian Yang, and Kun-Shan Chen. Study on direction dependence of the fully polarimetric wind-induced ocean emissivity at l-band using a semi-theoretical approach for aquarius and smap observations. *Remote Sensing of Environment*, 265:112661, 2021.
URL: <https://www.sciencedirect.com/science/article/pii/S0034425721003813>, doi: <https://doi.org/10.1016/j.rse.2021.112661>.

73

Sang-Moo Lee and Albin J. Gasiewski. A physically based two-scale ocean surface emissivity model tuned to windsat and ssm/i polarimetric brightness temperatures. *IEEE Transactions on Geoscience and Remote Sensing*, 60():1–23, 2022. doi:[10.1109/TGRS.2021.3133852](https://doi.org/10.1109/TGRS.2021.3133852).

74

E.C. Monahan and I. G. O'Muircheartaigh. Whitecaps and the passive remote sensing of the ocean surface. *Int. J. Remote Sens.*, 7(5):627–642, 1986. doi:[10.1080/01431168608954716](https://doi.org/10.1080/01431168608954716).

75

A. Stogryn. The Emissivity of Sea Foam at Microwave Frequencies. *J. Geophys. Res.*, 77(9):1658–1666, March 1972.
URL: <http://dx.doi.org/10.1029/JC077i009p01658>, doi:[10.1029/JC077i009p01658](http://dx.doi.org/10.1029/JC077i009p01658).

76

Nicolas Reul and Bertrand Chapron. A model of sea-foam thickness distribution for passive microwave remote sensing applications. *J. Geophys. Res.*, 108(C10):3321, 2003. doi:[10.1029/2003JC001887](https://doi.org/10.1029/2003JC001887).

77

A. Camps, M. Vall-llossera, R. Villarino, N. Reul, B. Chapron, I. Corbella, N. Duffo, F. Torres, J. J. Miranda, R. Sabia, A. Monerris, and R. Rodriguez. The emissivity of foam-covered water surface at L-band: theoretical modeling and experimental results from the FROG 2003 field experiment. *IEEE Trans. Geosci. Remote Sens.*, 43(5):925–937, May 2005. [doi:10.1109/TGRS.2004.839651](https://doi.org/10.1109/TGRS.2004.839651).

78

David J. Erickson, John T. Merrill, and Robert A. Duce. Seasonal estimates of global oceanic whitecap coverage. *Journal of Geophysical Research: Oceans*, 91(C11):12975–12977, 1986.
URL: <https://agupubs.onlinelibrary.wiley.com/doi/abs/10.1029/JC091iC11p12975>, arXiv:<https://agupubs.onlinelibrary.wiley.com/doi/pdf/10.1029/JC091iC11p12975>, doi:<https://doi.org/10.1029/JC091iC11p12975>.

79

William Asher, James Edson, Wade Mcgillis, Rik Wanninkhof, David T. Ho, and Trina Litchendorf. *Fractional Area Whitecap Coverage and Air-Sea Gas Transfer Velocities Measured During GasEx-98*, chapter, pages 199–203. American Geophysical Union (AGU), 2002.
URL: <https://agupubs.onlinelibrary.wiley.com/doi/abs/10.1029/GM127p0199>, arXiv:<https://agupubs.onlinelibrary.wiley.com/doi/pdf/10.1029/GM127p0199>, doi:<https://doi.org/10.1029/GM127p0199>.

80

V. G. Bondur and E. A. Sharkov. Statistical properties of whitecaps on a rough sea. *Oceanology*, 22(3):274–279, 1982.

81

Magdalena D. Anguelova and Ferris Webster. Whitecap coverage from satellite measurements: A first step toward modeling the variability of oceanic whitecaps. *J. Geophys. Res.*, March 2006.
URL: <http://dx.doi.org/10.1029/2005JC003158>, doi:10.1029/2005JC003158.

82

Adrian Callaghan, Gerrit de Leeuw, Leo Cohen, and Colin D. O'Dowd. Relationship of oceanic whitecap coverage to wind speed and wind history. *Geophys. Res. Lett.*, 35(23):L23609, December 2008. [doi:10.1029/2008GL036165](https://doi.org/10.1029/2008GL036165).

83

Dean F. Smith, Bob L. Weber, and Albin J. Gasiewski. An anisotropic ocean surface emissivity model based on windsat polarimetric brightness observations. In *2008 Microwave Radiometry and Remote Sensing of the Environment*, volume, 1–4. 2008. [doi:10.1109/MICRAD.2008.4579491](https://doi.org/10.1109/MICRAD.2008.4579491).

84

Simon H Yueh. Estimates of faraday rotation with passive microwave polarimetry for microwave remote sensing of earth surfaces. *IEEE Transactions on Geoscience and Remote Sensing*, 38(5):2434–2438, 2000.

85

David M Le Vine and Saji Abraham. The effect of the ionosphere on remote sensing of sea surface salinity from space: absorption and emission at l band. *IEEE Transactions on Geoscience and Remote Sensing*, 40(4):771–782, 2002.

86

Jean-Luc Vergely, Philippe Waldteufel, Jacqueline Boutin, Xiaobin Yin, Paul Spurgeon, and Steven Delwart. New total electron content retrieval improves smos sea surface salinity. *Journal of Geophysical Research: Oceans*, 119(10):7295–7307, 2014.

87

N. Reul, J. Tenerelli, B. Chapron, and P. Waldteufel. Modeling Sun Glitter at L-Band for Sea Surface Salinity Remote Sensing With SMOS. *IEEE Trans. Geosci. Remote Sens.*, 45(7):2073–2087, July 2007. [doi:10.1109/TGRS.2006.890421](https://doi.org/10.1109/TGRS.2006.890421).

88

Ali Khazâal, Joseph Tenerelli, and François Cabot. Impact of sun glint on the smos retrieved brightness temperature maps for almost four years of data. *Remote Sensing of Environment*, 180:234–245, 2016. Special Issue: ESA's Soil Moisture and Ocean Salinity Mission - Achievements and Applications. URL: <https://www.sciencedirect.com/science/article/pii/S0034425716300311>, doi:<https://doi.org/10.1016/j.rse.2016.02.003>.

89

Jacqueline Boutin, Jean-Luc Vergely, Stéphane Marchand, Francesco d'Amico, Audrey Hasson, Nicolas Kolodziejczyk, Nicolas Reul, Gilles Reverdin, and Jérôme Vialard. New smos sea surface salinity with reduced systematic errors and improved variability. *Remote Sensing of Environment*, 214:115–134, 2018.

90

Estrella Olmedo, Justino Martínez, Antonio Turiel, Joaquim Ballabriga-Poy, and Marcos Portabella. Debiased non-bayesian retrieval: a novel approach to smos sea surface salinity. *Remote Sensing of Environment*, 193:103–126, 2017.

91

Estrella Olmedo, Isabelle Taupier-Letage, Antonio Turiel, and Aida Alvera-Azcárate. Improving smos sea surface salinity in the western mediterranean sea through multivariate and multifractal analysis. *Remote Sensing*, 2018. URL: <https://www.mdpi.com/2072-4292/10/3/485>, doi:[10.3390/rs10030485](https://doi.org/10.3390/rs10030485).

92

Semyon A Grodsky, Douglas Vandemark, and Hui Feng. Assessing coastal smap surface salinity accuracy and its application to monitoring gulf of maine circulation dynamics. *Remote Sensing*, 10(8):1232, 2018.

93

Semyon A Grodsky, Nicolas Reul, Abderrahim Bentamy, Douglas Vandemark, and Sébastien Guimbard. Eastern mediterranean salinification observed in satellite salinity from smap mission. *Journal of Marine Systems*, 198:103190, 2019.

94

N. Reul, S. A. Grodsky, M. Arias, J. Boutin, R. Catany, B. Chapron, F. D'Amico, E. Dinnat, C. Donlon, A. Fore, S. Fournier, S. Guimbard, A. Hasson, N. Kolodziejczyk,

G. Lagerloef, T. Lee, D. M. Le Vine, E. Lindstrom, C. Maes, S. Mecklenburg, T. Meissner, E. Olmedo, R. Sabia, J. Tenerelli, C. Thouvenin-Masson, A. Turiel, J.-L. Vergely, N. Vinogradova, F. Wentz, and S. Yueh. Salinity estimates from Spaceborne L-band radiometers: an overview of the first decade of observation (2010–2019). *Remote Sens. Environ.*, 242:111769, 2020.
URL: <https://doi.org/10.1016/j.rse.2020.111769>, doi:10.1016/j.rse.2020.111769.

95

D. M. Le Vine, S. Abraham, F. Wentz, and G. S. E. Lagerloef. Impact of the Sun on remote sensing of sea surface salinity from space. In *Proc. IEEE Int. Geoscience and Remote Sensing Symp. IGARSS '05*, volume 1. 2005.

96

N. Reul, J. E. Tenerelli, N. Flouri, and B. Chapron. Earth-viewing L-band radiometer sensing of sea surface scattered celestial sky radiation. Part II: application to SMOS. *IEEE Trans. Geosci. Remote Sens.*, 46(3):675–688, March 2008. doi:10.1109/TGRS.2007.914804.

97

Joseph E Tenerelli, Nicolas Reul, Alexis A Mouche, and Bertrand Chapron. Earth-viewing l-band radiometer sensing of sea surface scattered celestial sky radiation—part i: general characteristics. *IEEE Transactions on Geoscience and Remote Sensing*, 46(3):659–674, 2008.

98

Emmanuel P Dinnat and David M Le Vine. Impact of sun glint on salinity remote sensing: an example with the aquarius radiometer. *IEEE Transactions on Geoscience and Remote Sensing*, 46(10):3137–3150, 2008.

99

HJ Liebe, PW Rosenkranz, and GA Hufford. Atmospheric 60-ghz oxygen spectrum: new laboratory measurements and line parameters. *Journal of quantitative spectroscopy and radiative transfer*, 48(5-6):629–643, 1992.

100

Niels Skou and Dorthe Hoffman-Bang. L-band radiometers measuring salinity from space: atmospheric propagation effects. *IEEE transactions on geoscience and remote sensing*, 43(10):2210–2217, 2005.

101

Frank J Wentz and Thomas Meissner. Atmospheric absorption model for dry air and water vapor at microwave frequencies below 100ghz derived from spaceborne radiometer observations. *Radio Science*, 51(5):381–391, 2016.

102

Simon H Yueh, Steve J Dinardo, Alexander G Fore, and Fuk K Li. Passive and active l-band microwave observations and modeling of ocean surface winds. *IEEE transactions on geoscience and remote sensing*, 48(8):3087–3100, 2010.

103

Thomas Meissner and Andrew Manaster. Smap salinity retrievals near the sea-ice edge using multi-channel amsr2 brightness temperatures. *Remote Sensing*, 2021. URL: <https://www.mdpi.com/2072-4292/13/24/5120>, doi:10.3390/rs13245120.

104

William Peake. Interaction of electromagnetic waves with some natural surfaces. *IRE Transactions on Antennas and Propagation*, 7(5):324–329, 1959.

105

A. J. Gasiewski and D. B. Kunkee. Polarized microwave emission from water waves. *Radio Sci.*, 29:1449–1466, 1994. doi:[10.1029/94RS01923](https://doi.org/10.1029/94RS01923).

106

J. T. Johnson and M. Zhang. Theoretical study of the small slope approximation for ocean polarimetric thermal emission. *IEEE Trans. Geosci. Remote Sens.*, 37(5):2305–2316, 1999.

107

Sang-Moo Lee and Albin J. Gasiewski. A physically based two-scale ocean surface emissivity model tuned to windsat and ssm/i polarimetric brightness temperatures. *IEEE Transactions on Geoscience and Remote Sensing*, 60():1–23, 2022. doi:[10.1109/TGRS.2021.3133852](https://doi.org/10.1109/TGRS.2021.3133852).

108

C. S. Cox and W. H. Munk. Measurement of the roughness of the sea surface from photographs of the sun's glitter. *J. Opt. Soc. Am.*, 44(11):838–850, 1954. doi:[10.1364/JOSA.44.000838](https://doi.org/10.1364/JOSA.44.000838).

109

V. N. Kudryavtsev, V. K. Makin, and B. Chapron. Coupled sea surface-atmosphere model: 2. spectrum of short wind waves. *Journal of Geophysical Research: Oceans*, 104(C4):7625–7639, 1999. URL: <https://agupubs.onlinelibrary.wiley.com/doi/abs/10.1029/1999JC900005>, arXiv:<https://agupubs.onlinelibrary.wiley.com/doi/pdf/10.1029/1999JC900005>, doi: <https://doi.org/10.1029/1999JC900005>.

110

Vladimir Kudryavtsev, Danièle Hauser, Gérard Caudal, and Bertrand Chapron. A semiempirical model of the normalized radar cross-section of the sea surface 1. background model. *Journal of Geophysical Research: Oceans*, 108(C3):FET 2–1–FET 2–24, 2003. URL: <https://agupubs.onlinelibrary.wiley.com/doi/abs/10.1029/2001JC001003>, arXiv:<https://agupubs.onlinelibrary.wiley.com/doi/pdf/10.1029/2001JC001003>, doi: <https://doi.org/10.1029/2001JC001003>.

111

V. Kudryavtsev, D. Akimov, J. Johannessen, and B. Chapron. On radar imaging of current features: 1. model and comparison with observations. *Journal of Geophysical Research: Oceans*, 110(C7):, 2005. URL: <https://agupubs.onlinelibrary.wiley.com/doi/abs/10.1029/2004JC002505>, arXiv:<https://agupubs.onlinelibrary.wiley.com/doi/pdf/10.1029/2004JC002505>, doi: <https://doi.org/10.1029/2004JC002505>.

112

M. V. Yurovskaya, V. A. Dulov, B. Chapron, and V. N. Kudryavtsev. Directional short wind wave spectra derived from the sea surface photography. *Journal of Geophysical Research: Oceans*, 118(9):4380–4394, 2013.
URL: <https://agupubs.onlinelibrary.wiley.com/doi/abs/10.1002/jgrc.20296>, arXiv:
<https://agupubs.onlinelibrary.wiley.com/doi/pdf/10.1002/jgrc.20296>, doi:<https://doi.org/10.1002/jgrc.20296>.

113

T. Elfouhaily, B. Chapron, K. Katsaros, and D. Vandemark. A unified directional spectrum for long and short wind-driven waves. *Journal of Geophysical Research: Oceans*, 102(C7):15781–15796, 1997.
URL: <https://agupubs.onlinelibrary.wiley.com/doi/abs/10.1029/97JC00467>, arXiv:
<https://agupubs.onlinelibrary.wiley.com/doi/pdf/10.1029/97JC00467>, doi:<https://doi.org/10.1029/97JC00467>.

114

M. A. Donelan, J. Hamilton, and W. H. Hui. Directional spectra of wind-generated waves. *Phil. Trans. Roy. Soc. London A*, 315(1534):509–562, 1985. [doi:10.1098/rsta.1985.0054](https://doi.org/10.1098/rsta.1985.0054).

115

David M. Le Vine, Emmanuel P. Dinnat, Thomas Meissner, Frank J. Wentz, Hsun-Ying Kao, Gary Lagerloef, and Tong Lee. Status of aquarius and salinity continuity. *Remote Sensing*, 2018. URL: <https://www.mdpi.com/2072-4292/10/10/1585>, [doi:10.3390/rs10101585](https://doi.org/10.3390/rs10101585).

116

Jianjun Guo, Leung Tsang, William Asher, K-H Ding, and C-T Chen. Applications of dense media radiative transfer theory for passive microwave remote sensing of foam covered ocean. *IEEE transactions on geoscience and remote sensing*, 39(5):1019–1027, 2001.

117

J. D. Droppleman. Apparent microwave emissivity of sea foam. *Journal of Geophysical Research (1896-1977)*, 75(3):696–698, 1970.
URL: <https://agupubs.onlinelibrary.wiley.com/doi/abs/10.1029/JC075i003p00696>,
arXiv:<https://agupubs.onlinelibrary.wiley.com/doi/pdf/10.1029/JC075i003p00696>,
doi:<https://doi.org/10.1029/JC075i003p00696>.

118

R. P. Barber Jr. and Jin Wu. Sea brightness temperature and effects of spray and whitecaps. *Journal of Geophysical Research: Oceans*, 102(C3):5823–5827, 1997.
URL: <https://agupubs.onlinelibrary.wiley.com/doi/abs/10.1029/96JC03760>, arXiv:
<https://agupubs.onlinelibrary.wiley.com/doi/pdf/10.1029/96JC03760>, doi:<https://doi.org/10.1029/96JC03760>.

119

LA Dombrovskiy and V Yu Rayzer. Microwave model of a two-phase medium at the ocean surface. *IZVESTIIA-RUSSIAN ACADEMY OF SCIENCES ATMOSPHERIC*

AND OCEANIC PHYSICS C/C OF IZVESTIYA-ROSSIISKAIA AKADEMIIA NAUK FIZIKA ATMOSFERY I OKEANA, 28:650–650, 1992.

120

Igor V Cherny and Victor Yu Raizer. *Passive microwave remote sensing of oceans*. John Wiley & Son Limited, 1998.

121

L. M. Zurk, L. Tsang, K. H. Ding, and D. P. Winebrenner. Monte carlo simulations of the extinction rate of densely packed spheres with clustered and nonclustered geometries. *J. Opt. Soc. Am. A*, 12(8):1772–1781, Aug 1995.
URL: <https://opg.optica.org/josaa/abstract.cfm?URI=josaa-12-8-1772>, doi:10.1364/JOSAA.12.001772.

122

LA Dombrovskiy. Calculation of the thermal radiation emission of foam on the sea surface. *Academy of Sciences, USSR, Izvestiya, Atmospheric and Oceanic Physics*, 15:193–198, 1979.

123

Jin Wu. Variations of whitecap coverage with wind stress and water temperature. *Journal of physical oceanography*, 18(10):1448–1453, 1988.

124

W.K. Melville and P. Matusov. Distribution of breaking waves at the ocean surface. *Nature*, 3(4):155–158, 2002. doi:10.1038/417058a.

125

E.C. Monahan and D. K. Woolf. Comments on Variations of whitecap coverage with wind stress and water temperature. *J. Phys. Oceanogr.*, 19(5):706–709, May 1989.
URL: [http://dx.doi.org/10.1175/1520-0485\(1989\)019<0706:COOWCW>2.0.CO;2](http://dx.doi.org/10.1175/1520-0485(1989)019<0706:COOWCW>2.0.CO;2), doi:10.1175/1520-0485(1989)019<0706:COOWCW>2.0.CO;2.

126

Fawwaz T Ulaby. Microwave remote sensing active and passive. *Rader remote sensing and surface scattering and emission theory*, pages 848–902, 1982.

127

Philip W Rosenkranz. Water vapor microwave continuum absorption: a comparison of measurements and models. *Radio Science*, 33(4):919–928, 1998.

128

Propagation modeling of moist air and suspended water/ice particles at frequencies below 1000 GHz, November 1993.

129

missing journal in Liebe1989

130

Hans J Liebe and Donald H Layton. Millimeter-wave properties of the atmosphere: laboratory studies and propagation modeling. *NASA STI/Recon Technical Report N*, 88:21387, 1987.

131

F. J. Wentz. The forward scattering of microwave solar radiation from a water surface. *Radio Sci.*, 13(1):131–138, January 1978. [doi:10.1029/RS013i001p00131](https://doi.org/10.1029/RS013i001p00131).

132

J Aarons. A review of: “solar system radio astronomy”. edited by j. aarons. (new york : plenum press, 1965.) [pp.xi + 416.] price \\$17.50. *International Journal of Electronics*, 20(3):293–293, 1966.
URL: <https://doi.org/10.1080/0020721660893786>, arXiv:<https://doi.org/10.1080/0020721660893786>, doi:[10.1080/0020721660893786](https://doi.org/10.1080/0020721660893786).

133

A. G. Voronovich and V. U. Zavorotny. Theoretical Model for Scattering of Radar Signals in Ku- and C-bands from a Rough Sea Surface with Breaking Waves. *Waves in Random Media*, 11:247–269, 2001. [doi:10.1080/13616670109409784](https://doi.org/10.1080/13616670109409784).

134

David M. Le Vine and Saji Abraham. Galactic noise and passive microwave remote sensing from space at L-band. *IEEE Trans. Geosci. Remote Sens.*, 42(1):119–129, January 2004. [doi:10.1109/TGRS.2003.817977](https://doi.org/10.1109/TGRS.2003.817977).

135

E. P. Dinnat, D. M. Le Vine, and S. Abraham. L-band radiometry and reflection of the galaxy by a rough ocean surface. In *Proc. Microwave Radiometry and Remote Sensing of the Environment MICRORAD 2008*, 1–4. 11–14 March 2008. [doi:10.1109/MICRAD.2008.4579494](https://doi.org/10.1109/MICRAD.2008.4579494).

136

missing institution in meissner2019

137

J.L. Garrison, A. Komjathy, V.U. Zavorotny, and S.J. Katzberg. Wind speed measurement using forward scattered gps signals. *IEEE Transactions on Geoscience and Remote Sensing*, 40(1):50–65, 2002. [doi:10.1109/36.981349](https://doi.org/10.1109/36.981349).

138

W.J. Wilson, S.H. Yueh, S.J. Dinardo, S.L. Chazanoff, A. Kitiyakara, F.K. Li, and Y. Rahmat-Samii. Passive active L- and S-band (PALS) microwave sensor for ocean salinity and soil moisture measurements. *IEEE Trans. Geosci. Remote Sens.*, 39(5):1039–1048, May 2001. [doi:10.1109/36.921422](https://doi.org/10.1109/36.921422).

139

N. Reul, J. Tenerelli, B. Chapron, S. Guimbard, S.-S. Picard, P.-Y. Le Traon, and S. Zine. Preparing the potential and challenge of remote sensing-based sea surface salinity estimation: the cosmos airborne campaign. In *Proceedings of the SPIE 7150*. edited by R. J. Frouin et al., 2008. [doi:10.1117/12.804940](https://doi.org/10.1117/12.804940).

140

A. Ludwig. The definition of cross polarization. *IEEE Transactions on Antennas and Propagation*, 21(1):116–119, 1973. [doi:10.1109/TAP.1973.1140406](https://doi.org/10.1109/TAP.1973.1140406).

141

M Zundo and B Duesman. On-ground bt frame of reference tn. Technical Report SO-TN-ESA-GS-5873, ESA, 2010.

142

N Floury. Estimation of faraday rotation from auxiliary data. Technical Report, ESA, 2007.

143

G.A. Poe. Optimum interpolation of imaging microwave radiometer data. *IEEE Transactions on Geoscience and Remote Sensing*, 28(5):800–810, 1990. [doi:10.1109/36.58966](https://doi.org/10.1109/36.58966).

144

C. Bourlier and G. Berginc. Microwave analytical backscattering models from randomly rough anisotropic sea surface - Comparison with experimental data in C and Ku bands. *Progress in Electromagnetics Research*, 37:31–78, 2002.

145

G. B. Arfken and H. J. Weber. Mathematical methods for physicists 6th ed. *Materials and Manufacturing Processes*, 2005.

146

S. Blanch and A. Aguasca. Sea water dielectric permittivity models: review and impact on the brightness temperature at L-band. In *Proc. SMOS Campaigns Workshop, ESA SP-525*, 137–141. 2003.

147

C. S. Cox and W. H. Munk. Statistics of the sea surface derived from sun glitter. *J. Mar. Res.*, 13:198–227, 1954.

148

Hans J. Liebe. An updated model for millimeter wave propagation in moist air. *Radio Science*, 20(5):1069–1089, 1985.

URL: <https://agupubs.onlinelibrary.wiley.com/doi/abs/10.1029/RS020i005p01069>, arXiv:<https://agupubs.onlinelibrary.wiley.com/doi/pdf/10.1029/RS020i005p01069>, doi:<https://doi.org/10.1029/RS020i005p01069>.

149

Victor Raizer. *Advances in Passive Microwave Remote Sensing of Oceans*. CRC Press, 2017.

150

Ram Somaraju and Jochen Trumpf. Frequency, temperature and salinity variation of the permittivity of seawater. *IEEE Transactions on Antennas and Propagation*, 54(11):3441–3448, 2006. [doi:10.1109/TAP.2006.884290](https://doi.org/10.1109/TAP.2006.884290).